Structures and Mechanical Properties of Single Macromolecules at surfaces

Dissertation

zur Erlangung des akademischen Grades

doctor rerum naturalium

(Dr. rer. nat.)

im Fach: Physik

Spezialisierung: Experimentalphysik

eingereicht an der

Mathematisch-Naturwissenschaftlichen Fakultät

der Humboldt-Universität zu Berlin

von

Herrn M. Sc. Hua Liang

Präsident der Humboldt-Universität zu Berlin:

Prof. Dr. Jan-Hendrik Olbertz

Dekan der Mathematisch-Naturwissenschaftlichen Fakultät:

Prof. Dr. Elmar Kulke

Gutachter:

1. Prof. Dr. Jürgen P. Rabe
2. Prof. Dr. Matthias Ballauff
3. Prof. Dr. Paolo Samori

Tag der mündlichen Prüfung: 18.12.2014

Abstract

In order to investigate correlations between structure, properties and potential applications at the single molecule level, I chose three macromolecular systems: DNA, amphiphilic cylindrical polymer brushes, and amphiphilic core-shell structured hyperbranched polyglycerol (hPG). They form quasi one-, two-, and three dimensional structures on suitable surfaces, exhibit interesting mechanical properties, and also offer potential for applications.

First, I report a simple high throughput method to control the conformation of plasmid double-stranded DNA on a graphene surface, pre-coated with a layer of flat lying alkylamines. Depending on the surface concentration, the alkylamines self-assemble into various nanostructures and induce different DNA conformations: (i) supercoiled DNA, (ii) stretched DNA, partially melted into two single strands, (iii) DNA with an overstretched backbone up to 0.42 ± 0.01 nm per base on the surface as compared to 0.34 ± 0.01 nm in a physiological solution, (iv) relaxed circles without stretching, and (v) compact coils. This method allows to directly correlate DNA conformations to mechanical properties such as twist-stretch coupling. The plasmid DNA molecules were stretched further, up to 2.1 times their native B-form length and ruptured with a Scanning Force Microscope (SFM), exerting a force parallel to the surface. This force is either large enough to break the molecule immediately, or it is compensated by the elastic restoring force of the DNA backbone, which allows to stabilizes the molecular length of the DNA on the immobilizing surface. However, also the size-stabilized molecules break with time, the longer the molecules the quicker. The breakage of different lengths of stabilized molecules was recorded in order to study the time-dependent mechanical properties of the molecules under constant forces. From these data a rather high rate constant for breakage, k_0 = (2.2 ± 0.1) × 10^{-7} s^{-1}, was calculated. Moreover, I found a non-linear stress-strain dependence of DNA on the surface, which I attribute to DNA conformational transitions. Assuming that the structural transition on the surface is similar to that in solution I estimated the forces needed to stretch the molecules and thereby verified the estimated activation energy barrier.

The second system I studied was dual cylindrical polymer brushes, whose self-assembly I investigated at different surfaces. The brush polymers reveal worm-like chain conformations on mica, after being deposited from a chloroform solution. Due to different affinities of the side chains to the surface, parts of the side chains collapsed, while others fully extended on the surface, resulting in a "tadpole like" or a back-folding structure. Deposited from an aqueous solution, the dual cylindrical polymer brushes form supramolecular aggregates on the surface. These aggregates form clusters of different size and self-sort according to their size on the surface. The size of the clusters depends on their motilities on the surface.

The third system, I report on, is an innovative bi-functional nanocarrier. I investigated its supramolecular structure and its encapsulation and transportation capacities for typical guest molecules, such as nile red and pyrene. The polymer has been obtained by chemically tailoring hyperbranched polyglycerol to form an amphiphilic core-shell structure, which creates a large hydrophobic gradient across the polymer molecule leading to better selective transport capacities and better water solubility. SFM, light scattering, and spectroscopic results show that it encapsulates and transports guest molecules in both, a "unimolecular micelle" and polymeric micelle type mechanism. The capacity of co-loading of two drugs and controlled release makes it a promising candidate for simultaneous delivery of two hydrophobic drugs in cancer combination therapy.

Zusammenfassung

Die vorliegende Arbeit ist der Untersuchung von Zusammenhängen zwischen Struktur, Eigenschaften, und potentiellen Anwendung auf der Ebene einzelner Moleküle gewidmet. Dazu wurden drei makromolekulare Systeme ausgewählt: DNA, amphiphile Block-Bürstenpolymere, und amphiphile, hyperverzweigter Polyglycerine. Diese bilden quasi ein-, zwei-, und drei-dimensionale Strukturen auf geeigneten Oberflächen, zeigen interessante mechanische Eigenschaften, und bieten sich darüber hinaus für potentielle Anwendungen an.

Als erstes wird eine einfache, aber sehr effiziente Methode zur kontrollierten Abscheidung von plasmidischer, doppelsträngiger DNA mit definierten Konformationen auf Graphen-Oberflächen vorgestellt, die mit einer Monolage aus flach adsorbierten Alkylaminen vorbeschichtet sind. Abhängig vom Grad der Oberflächenbedeckung ordnen sich die Alkylamine in verschiedenen Nanostrukturen und erlauben damit die Präparation unterschiedlicher DNA Konfirmationen: (i) *supercoiled* DNA, (ii) gestreckte doppelsträngige DNA, die teilweise in zwei Einzelstränge aufgeschmolzen ist, (iii) DNA mit einem, auf bis zu 0.42 ± 0.01 nm pro Basenpaar überdehnten Rückgrat auf der Oberfläche, verglichen mit 0.34 ± 0.01 nm in einer physiologischen Lösung, (iv) entspannter, ungedehnter Ring und (v) kompaktes Knäuel. Diese Methode erlaubt es, direkt DNA Konformationen mit mechanischen Eigenschaften, wie der Kopplung von Streckung und Verdrillung zu korrelieren. Mit Hilfe eines Kraftmikroskops, mit dem man eine Kraft parallel zur Oberfläche anlegen kann, wurden die plasmidischen DNA Moleküle auf bis zum 2.1-fachen der ursprünglichen B-Form Länge gestreckt und dann gerissen. Die angelegte Kraft ist entweder groß genug, um das Molekül sofort zu zerreißen oder sie wird von der elastischen Rückstellkraft des DNA Rückgrats kompensiert, wodurch die Länge des Moleküls auf der immobilisierenden Oberfläche stabilisiert wird. Auch die Längen-stabilisierten Moleküle reißen mit der Zeit, und zwar umso schneller, je länger die Moleküle sind. Das Reißverhalten wurde bei konstanter Kraft untersucht. Aus diesen Daten wurde ein relativ hohe Geschwindigkeitskonstante $k_0 = (2.2 \pm 0.1) \times 10^{-7}\ s^{-1}$

berechnet. Außerdem wurde eine nicht-lineare Abhängigkeit der Streckung von der angelegten Spannung der DNA auf der Oberfläche gefunden, die auf Konformations-Übergänge der DNA zurückgeführt werden konnten. Unter der Annahme ähnlicher Konformations-Übergänge auf der Oberfläche und in Lösung ähnlich wurden die erforderlichen Streckkräfte abgeschätzt und damit die unabhängig abgeschätzte Energiebarriere bestätigt.

Das zweite in der Arbeit untersuchte System sind amphiphile Block-Bürstenpolymere, deren Selbst-Assemblierung auf verschiedenen Oberflächen untersucht wurde. Aus Chloroform-Lösung auf Glimmer abgeschiedene Polymere wiesen wurmartige Konformationen auf. Wegen der unterschiedlichen Oberflächenaffinitäten der Seitenketten sind diese zu einem Teil kollabiert, während sich ein anderer Teil ausstreckt. Das an Kaulquappen erinnernde Ergebnis ist eine Struktur mit rückgefalteten Kettenteilen. Aus wässriger Lösung abgeschieden bilden diese amphiphilen Block-Bürstenpolymere supramolekulare Aggregate auf der Oberfläche. Die Aggregate bilden verschieden große Cluster und sortieren sich nach ihrer Größe.

Das dritte in dieser Arbeit untersuchte System ist ein innovativer funktioneller Nanocarrier, der aus hyperverzweigten Polyglycerinen chemisch maßgeschneidert wurde. Die amphiphile Kern-Schale-Struktur verursacht einen großen hydrophoben Gradienten quer durch das Molekül, und damit eine bessere Wasserlöslichkeit sowie eine selektivere Transportkapazität. Ihre supramolekulare Struktur und ihre Verkapselungs- und Transportkapazität für typische Gastmoleküle wie Nil Rot und Pyren wurden mit Hilfe von SFM, Lichtstreu-, und Spektroskopie-Methoden untersucht. Die Ergebnisse zeigen, dass die Polymere verschiedene Gastmoleküle sowohl in unimolekulan Mizellen wie auch in polymeren Mizellen verkapseln und transportieren. Das Polymer ist ein vielversprechender Kandidat für die gleichzeitige Bereitstellung von zwei hydrophoben Pharmaka.

Table of Contents

1. Introduction

1.1 Motivation and aims of this work

The properties and the possible applications of a polymer material strongly correlate with its structure. For bulk polymer materials, desired properties can be achieved by tailoring the molecular structures on different levels: primary, secondary and tertiary structures. Techniques such as annealing, polymer blending, and crosslinking are well established and widely used in the polymer industry. However it remains challenging to characterize these structure-property-application relations at a single polymer molecule level. In this work I try to demonstrate such relations by choosing three different polymer systems: DNA, amphiphilic cylindrical polymer brushes, and amphiphilic core-shell structured hyperbranched polyglycerol (hPG).

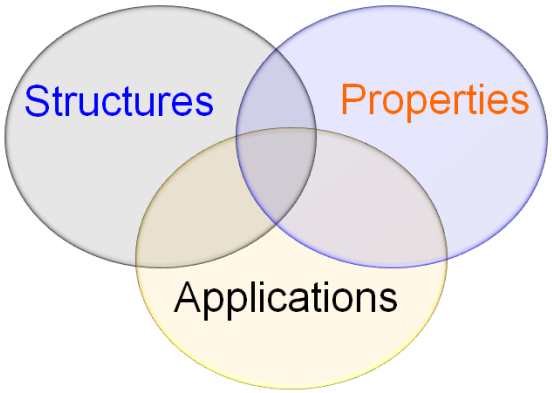

DNA mechanics were amply studied by stretching and twisting single DNA experimentally.[1-7] A "phase diagram" for DNA under torque and tension, i.e. different structural forms of DNA as a function of torque and tension, has been suggested based on force- or torque-extension curves.[8, 9] However, conventional single molecule manipulation experiments carried out in solution do not provide direct access to the conformational changes. Here I report on stretching plasmid DNA, utilizing a tunable surface and directly recording the

related DNA conformations. This allows to directly correlate DNA conformations to mechanical properties such as twist-stretch coupling.

The tensile strength of single DNA remains ambiguous. A value of 100-300 pN was obtained from shearing bulk DNA with buffer flow experiments.[4, 10] A tensile strength of 480 pN was calculated upon stretching single DNA with a receding meniscus. [11] Upon stretching DNA with an SFM tip, a tensile strength up to 1.7 nN was obtained.[12, 13] However these values are still smaller than the ones predicted by the bond potential theory for single C-C (4.2 nN) or C-O (4.3 nN) bonds.[14, 15] The rupture probability of a DNA chain relies on the external force applied, time of force loading, the number of repeating unit (base pairs), and possible chemical reactions with the environment such as hydrolysis of DNA phosphor diester backbone.[10, 16] In this work, I demonstrate, how with a recently developed method, "blowing manipulation", one can stretch and rupture plasmid DNA with an increasing forcing load and with a constant strain, applied for a time on the order of an hour. This allows to study the time-dependent tensile strength of DNA.

Beside its well-known role in genetics, DNA is now also recognized as an excellent building block for manufacturing nano-size structures such as DNA-templated synthesis of metal nanowires,[17-19] two-dimensional DNA crystals and supramolecular structures.[20, 21] DNA is the essential part for DNA nanomachines,[22-24] which produce nanoscale movement usually triggered by DNA conformational changes such as hybridization of the complementary strands. In order to directly sequence DNA one needs a fully stretched DNA backbone on a surface.[25-27] Therefore controlling and manipulating the DNA conformation at a single molecule level plays an important role for these applications. It remains a challenging task to deposit DNA on a solid surface in a predefined manner. While it has been reported that the conformation of ds-DNA molecules can be manipulated one by one with a Scanning Force Microscopy (SFM) tip after they were deposited on a surface,[28] a higher throughput method to control DNA conformation on a surface is desirable. In this work, I report a simple high

throughput method to control the conformation of plasmid double-stranded DNA on a graphene surface, pre-coated with a layer of flat lying alkylamines.

Polymeric amphiphiles, compared with small molecule surfactants, are characterized by a much larger number of molecular variables. They offer an enormous wealth of possible molecular structures and supramolecular aggregate structures in selective solvent such as in water. The second and third polymer system chosen in this work are both polymeric amphiphiles, mainly amphiphilic cylindrical polymer brush and amphiphilic core-shell structured hPG. Due to their increasing complexity in chemical structures and due to their size, amphiphilic cylindrical polymer brushes and amphiphilic hPG derivatives were expected to have equilibrium structures and metastable colloidal structures such as supramolecular aggregations in bulk, in selective solvents as well as at surfaces.

Cylindrical polymer brushes, also known as molecular bottle brushes, have “brush like” structures and their conformation and physical properties are mainly controlled by the densely grafted side chains. With the help of different controlled free radical polymerization techniques, mainly atom transfer radical polymerization (ATRP), reversible addition fragmentation chain transfer polymerization (RAFT) and nitroxide-mediated polymerization (NMP), hydrophilic side chains (such as PEG and poly-NIPAM) and hydrophobic side chains (such as polystyrene and poly-butyl acrylate) were attached in sequence to form the amphiphilic block cylindrical polymer brushes used in this work.[29-31] In solution the molecular conformation and self-assembly structures of amphiphilic cylindrical polymer brushes depend on the selectivity of the solvent. On a surface, the different affinity of the side chains to the surface plays an important role. Here, I studied the single molecular conformation and the self-assembly of supramolecular structures of amphiphilic cylindrical polymer brushes on different surface.

Dendritic hyperbranched-polyglycerol (hPG) was synthesized through a single reaction step: ring-opening multi-branching polymerization (ROMB) of glycidol.[32] Compared with dendrimers, hPG has an imperfect dendritic structure but avoids multi-step synthesis and post

purifications. Due to its low price but relatively well-defined structure, good water solubility and biocompatibility, hPG finds its applications in many fields such as drug and gene delivery. The imperfect structure of hPG allows one to chemically modify the core as well as the outer surface of the molecule to make amphiphilic core-shell structured nano-carrier systems. In solution they exhibit both equilibrium structures (micelles) formed by single polymer molecules and non-equilibrium metal stable structures such as polymeric micelles. Therefore the nano-carrier system is expected to encapsulate guest molecules in a combination of a "unimolecular micelle" and a "polymeric micelle" mechanism. Furthermore the nanocarrier system is a promising candidate for simultaneous delivery of two or more drugs for a combination therapy in tumor treatment. In this part, I report both equilibrium and non-equilibrium structures formed by single hPG polymers, by molecular aggregates, as well as by host-guest complexes of the polymer and different guest molecules. The aim is to characterize the transport mechanism of the polymer system and help to design better drug delivery systems.

1.2 Outline of the thesis

Chapter 1 "Introduction" is followed by Chapter 2 "Scientific Backgrounds". Chapter 2 contains a brief introduction to the relevant polymer physics, a short review on DNA conformation and mechanical properties, and previous work on cylindrical polymer brushes and polymer based drug delivery systems.

Chapter 3 "Experiments and Data Analysis" gives a brief introduction to SFM and how the data are acquired and analyzed. The method to prepare the samples is also described in Chapter 3.

Chapter 4 "Result and Discussion" presents the main results. It is divided into three sub-chapters. Results from DNA conformational and mechanical studies are presented in sub-chapter 4.1. In this sub-chapter, a simple method is demonstrated to control the single DNA conformation on an alkyl amine pre-coated HOPG surface, which is followed by the time-

dependent rupture of single DNA chain. Sub-chapter 4.2 reports the results from the studies on the single molecule conformation and the supramolecular aggregates of amphiphilic cylindrical polymer brushes on different surfaces. The effect of the surface on the polymer structure is also presented. Sub-chapter 4.3 shows the results from the structure and transport capacity studies of amphiphilic hPG and its derivatives. It turns out that the nanocarrier system shows an innovative bi-functional transport capacity, which makes it a promising candidate for simultaneously delivery of two or more drugs.

Chapter 5 presents a brief summary and conclusion from the whole work.

2. Scientific Background

This chapter is written based on classical polymer physics textbooks such as *Statistical Physics of Macromolecules* (by A. R. Khokhlov, American Institute of Physics, 1997) and *Introduction to Polymer Physics* (by M. Doi, Oxford University Press, 1990), as well as literatures.

2.1. Models for single polymer chain conformation

2.1.1 Ideal chain

A polymer chain consists of many repeating units or chemical monomers. At large scale the chain conformation does not depend on the particular details of the repeating unit. Therefore in an ideal chain model, we neglect the specific interaction between the repeating units. There are a few mathematic models to describe such a chain.

Freely jointed chain (FJC)

In the Freely Jointed Chain (FJC) model, the monomer is regarded as a rigid rod with a length of a. The monomers are freely jointed together, completely independent of the orientations and positions of neighboring repeat units.

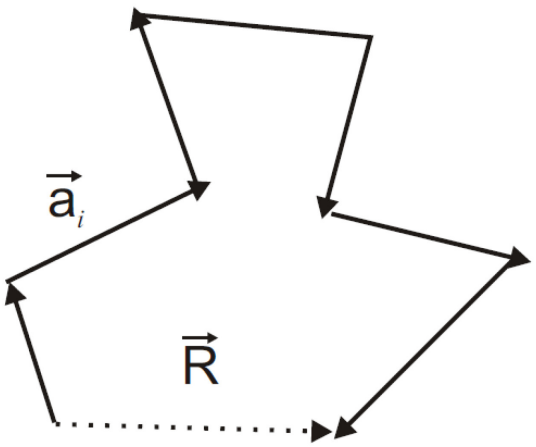

Figure 2-1. A freely joined chain model

The end-to-end distance is given by:

$$\vec{R} = \sum_{i=1}^{N} \vec{a}_i \qquad (2-1)$$

$$\langle \vec{R}^2 \rangle = \langle \left(\sum_{i=1}^{N} \vec{a}_i \right)^2 \rangle = \langle \sum_{i=1}^{N} {\vec{a}_i}^2 + 2 \sum_{i=1}^{N} \sum_{j=i+1}^{N} \vec{a}_i \vec{a}_j \rangle \qquad (2-2)$$

$$= \sum_{i=1}^{N} \langle (\vec{a}_i)^2 \rangle + 2 \sum_{i=1}^{N} \sum_{j=i+1}^{N} \langle \vec{a}_i \vec{a}_j \rangle \qquad (2-3)$$

Since the angle $\varphi_i \in [0,\ 2\pi]$ is randomly distributed, we get,

$$2 \sum_{i=1}^{N} \sum_{j=i+1}^{N} \langle \vec{a}_i \vec{a}_j \rangle = 0 \qquad (2-4)$$

and we obtain

$$\langle \vec{R}^2 \rangle = N a^2 \qquad (2-5)$$

The probability distribution of a polymer chain with N repeat units having the end-to-end distance of R is gaussian, which is described in a lattice model as follows

$$P_N(R) = \left(\frac{3}{2\pi N a^2} \right)^{3/2} \exp\left(-\frac{3R^2}{2Na^2} \right) \qquad (2-6)$$

The end-to-end distance R_0 is defined as

$$R_0 = \langle \vec{R}^2 \rangle^{1/2} = N^{1/2} a \qquad (2-7)$$

The radius of gyration, R_g , is given by

$$R_g = \left(\frac{1}{2N^2} \langle \sum_{i=1}^{N} \sum_{j=1}^{N} a_{ij}^2 \rangle \right)^{1/2} = \left(\frac{a^2}{2N^2} \sum_{i,j}^{N} |\ i-j\ | \right)^{1/2}$$

$$= \left(\frac{a^2}{2N^2} \sum_{i,j}^{N} |\ i-j\ | \right)^{1/2} = \left(\frac{a^2}{N} \sum_{k}^{N} \left(1 - \frac{k}{N} \right) k \right)^{1/2}$$

$$= \left(\frac{a^2(N^2-1)}{6N}\right)^{1/2} \approx \frac{aN^{1/2}}{\sqrt{6}} for\ n \gg 1 \qquad (2-8)$$

These are two useful parameters for theoretically estimating the size of the volume that a polymer chain occupies in three dimensions, e.g. in a solution.

Worm like chain (WLC)

A semi-flexible chain is better described by the worm like chain (WLC) model. In the FJC model, there is no orientation correlation between arbitrary neighboring repeat units. However, in the WLC model, the correlation follows an exponential decay with a decay constant, which is known as the persistence length l_p. This relationship is given by the following equation:

$$\langle \cos\varphi(s) \rangle = \exp\left(-\frac{s}{l_p}\right) \qquad (2-9)$$

s is the path along the chain with a contour length of L.

$\overrightarrow{U}(s) = \frac{d\vec{r}}{ds}$: a unit vector in the chain direction.

$$\langle \vec{R}^2 \rangle = \langle \left(\int_0^L ds \vec{U}(s) \right)^2 \rangle = \langle \int_0^L ds \vec{U}(s) \int_0^L ds' \vec{U}(s') \rangle \qquad (2-10)$$

$$= \int_0^L ds \int_0^L \langle \vec{U}(s) \cdot \vec{U}(s') \rangle ds' \qquad (2-11)$$

$$= 2\int_0^L ds \int_0^{L-s} e^{(-t/l_p)}\, dt \qquad (2-12)$$

where $t = s - s'$,

therefore

$$\langle \vec{R}^2 \rangle = 2l_p^2 \left(\frac{L}{l_p} - 1 + \exp(-L/l_p) \right) \qquad (2-13)$$

$$\langle \vec{R}^2 \rangle = \begin{cases} L^2, for\ L << l_p \\ 2Ll_p\ , for\ L >> l_p \end{cases} \qquad (2-14)$$

For an ideal chain, the properties of all models at scale $L >> l_p$ are similar. The chain reveals a coiled conformation with a size much smaller than its contour length L.

Closed circular chain

When the ends of a polymer chain are covalently connected to form a closed ring, the chain becomes more compact. The probability to find two repeating unit vector with an end-to-end distance of R_{ji} is described by the conditional probability under the condition that the end to end distance of the whole chain with N repeat units is 0,

$$P_N(\vec{R}_{ji}) = P_N(\vec{R}_{ji}|R = 0) \quad (2-15)$$

where

$$P_N(\vec{R}_{ji}|R = 0) = \frac{P_N(\vec{R}_{ji} \cap R = 0)}{P_N(R = 0)} \quad (2-16)$$

For an ideal chain the segment i-j and j-N-0-i is independent, and

$$P_N(\vec{R}_{ji} \cap R = 0) = P_{j-i}(\vec{R}_{ji}) P_{N-j+i}(\vec{R}_{ji}) \quad (2-17)$$

Putting Eq. (2-6) and (2-17) into (2-16), we get

$$P_N(\vec{R}_{ji}|R = 0) = \left(\frac{3}{2\pi\mu a^2}\right)^{3/2} \exp\left(-\frac{3R_{ji}^2}{2\mu a^2}\right) \quad (2-18)$$

with $\mu = (j-i)(N-j+i)/N$.

And we also obtain

$$\langle R_{ji}^2 \rangle = \mu a^2 \quad (2-19)$$

Therefore together with Eq. (2-8), the radius of gyration is obtained

$$\langle R_g^2 \rangle_{ring} = \frac{Na^2}{12} = \frac{\langle R_g^2 \rangle_{linear}}{2} \quad (2-20)$$

Thus compared with a linear ideal chain, the closed circular chain is more condensed by a fraction of $\sqrt{2}$.

The entropic elasticity of a polymer chain

In order to change its natural coiled conformation, e.g. to obtain a straight linear chain conformation, an external force is needed to overcome the entropic elasticity of the chain. This elasticity is not due to the enthalpy of the interactions of the monomers, but fully due to the entropy of a polymer chain. For an ideal chain there is no interactions between monomers, therefore the internal energy of the chain can be set to zero. The free energy of the chain is then given as

$$F = -TS \qquad (2-21)$$

Since

$$S = k_B \ln(W) \qquad (2-22)$$

then

$$F = -k_B T \ln(W) \approx -k_B T \ln(6^N P_N) \qquad (2-23)$$

Inserting eq. (2-6), we obtain

$$F \approx -k_B T \left[N\ln 6 + \frac{3}{2}\ln\left(\frac{3}{2\pi N a}\right) - \frac{3R^2}{2Na^2} \right] \qquad (2-24)$$

$$F = F_0 + k_B T \frac{3R^2}{2Na^2} \qquad (2-25)$$

Therefore

$$f = \frac{dF}{dR} = 3k_B T \frac{R}{Na^2} \qquad (2-26)$$

For small forces, the ideal chain acts like an ideal spring with spring constant of $3k_BT/(Na^2)$.

2.1.2 Excluded volume effects

The ideal chain does not include any interactions between the monomers. Due to the steric repulsion of the monomers (two monomers cannot occupy the same position), the ideal chain model holds only when the effective interactions between the monomers or between monomers and solvent molecules are balanced by the steric repulsion. For example, in a

polymer melt or in a "theta"-solvent, a polymer chain behaves like an ideal chain. In other conditions, interactions between the monomers need to be taken into account.

Flory approach

A successful approach is the Flory theory, which is based on a mean field approximation of density with the entropic elasticity of an ideal chain. In such a model a chain tends to be swollen due to the excluded volume, which is balanced by the loss of entropy due to the loss of possible chain conformations. The energetic contribution due to the excluded volume is given by the number of excluded volume interactions within a coil and the energy cost of each exclusion, k_BT. The total number of excluded volume interactions is just the probability of finding a monomer within the excluded volume of another. If we assume a mean density of monomers in the coil, N/R^3, then the number of excluded volume interactions per monomer is

$$U_i = \frac{v k_B T N}{R^3} \qquad (2-27)$$

where v is the excluded volume. For N monomers,

$$U = \sum_{i=1}^{N} = v k_B T \frac{N^2}{R^3} \qquad (2-28)$$

The free energy of the chain is

$$F = U - TS \qquad (2-29)$$

Inserting eq. (2-25) and (2-28) into eq. (2-29), we obtain

$$F \cong v k_B T \frac{N^2}{R^3} + k_B T \frac{3R^2}{2Na^2} \qquad (2-30)$$

The optimal radius R is calculated by minimizing the free energy.

$$\frac{\partial F}{\partial R} = 0 \qquad (2-31)$$

$$R \approx v^{1/5} a^{2/5} N^{3/5} \qquad (2-32)$$

For purely steric interactions, $v \sim a^3$, therefore

$$R \sim aN^{3/5} \qquad (2-33)$$

Formation of blobs

The repulsion between parts of the chain leads to the concept of blobs. A long polymer chain with excluded volume can be considered as a string of blobs with a diameter of *D*. Inside a blob, the interaction of the monomer is neglected, therefore it acts like an ideal chain.

$$D \sim ag^{v} i.e.\ \ g \sim (D/a)^{1/v} \qquad (2-34)$$

where *g* is the numbers of monomer per blob. The number of blobs is given by

$$n = N/g = \frac{N}{(D/a)^{1/v}} \qquad (2-35)$$

Since the block repels each other the overall system can be considered as a 1-dimensional (when the chain is confined in a pore) or 2-dimensional (flat geometry) "chain" of *n* blobs with a new "monomer" length of D. Therefore for two-dimensional excluded volume chain,

$$R \sim n^{v_2} D \sim N^{3/4} a^{5/4} D^{-1/4} \qquad (2-36)$$

2.1.3 Polymer solution

In very dilute polymer solution the concentration of chains and the concentration of monomer are very small, i.e. the chains behavior as independent chains. When the monomer concentration reaches the monomer concentration inside a polymer coil, the chains start to overlap. This concentration is given by

$$C^{*} = N/R^{3} \sim \frac{N^{-4/5}}{a^{3}} \qquad (2-37)$$

When $C > C^{*}$, a regime of a semi-dilute solution is reached first, and then a concentrated solution and finally a polymer melt, where there is no solvent at all.

Generally, a polymer chain in solution can experience three types of solvent. In a good solvent the monomer-solvent interaction is more favorable than monomer-monomer

interactions. Therefore the chain swells. The size of the chain is proportional to $N^{3/5}$ like the exclude volume chain. In poor solvent the monomer-monomer interaction is favorable, and the chain shrinks with a size proportional to $N^{1/3}$. In a theta-solvent, the effective overall interaction balances, and the polymer behaves like an ideal chain, whose size is proportional to $N^{1/2}$.

2.1.4 Charged polymers

Charged polymers, polyelectrolytes, carry charges along the backbone, which are neutralized by small counter ions. They are classified into two types, according to the charge density along the backbone. In a strongly charged polyelectrolyte each monomer has a charge, such as in double-stranded DNA. On the other hand, a weakly charged polyelectrolyte has less charged density. The Coulomb interaction is a long range interaction, which decays much slower than other non-specific interactions such as the Van der Waals interaction. Therefore for all theoretical approaches for polyelectrolytes the Coulomb interaction needs to be included.

The energy due to the electrostatic interaction of two point charges, e.g. unit charges e and e along the polymer backbone with a distance r is described as:

$$E(r) = k_B T l_B / r \qquad (2-38)$$

where

$$l_B = \frac{e^2}{\varepsilon k_B T} \qquad (2-39)$$

is the Bjerrum length: the separation, at which the electrostatic interaction between two elementary charges is equal to the thermal energy k_BT. ε is the dielectric constant of the solution.

For a strongly charged polymer chain with N repeating units, the number of charge pairs is ~ N^2, thus the energy due to the Coulomb interaction is given as

$$E_c \sim \frac{N^2 k_B T l_B}{R_0} \sim \frac{N^2 k_B T l_B}{N^{\nu} a} \sim N^{2-\nu} k_B T l_B a^{-1} \qquad (2-40)$$

For a polymer coil: $\nu < 1$, therefore

$$E_c \sim N^{2-\nu} \gg N^1 \qquad (2-41)$$

Eq. (2-41) implies that at large N, the repulsive Coulomb interaction overwhelms the entropic contribution to the free energy gained by the coil conformation of the long polymer. Therefore the chain tends to fully extend. Thus for a strongly charged polymer chain in a dilute counter ion free solution, the chain is fully extended, and

$$R_0 \sim N \qquad (2-42)$$

However, in the presence of counter ions, the electrostatic interaction is reduced or screened. In this case, Eq. (2-42) no longer holds. Since the repulsive electrostatic interaction is screened at large scales, the chain coils. The effective electrostatic interaction is given by:

$$E_D = \frac{k_B T l_B}{r} \exp(-r\kappa) \qquad (2-43)$$

where κ^{-1} is the Debye length, which determines the effective screening length, and it relates with the salt concentration or more precisely the ionic strength through:

$$\kappa^{-1} = \sqrt{\frac{\varepsilon \varepsilon_0 k_B T}{2e^2 c_{salt}}} \qquad (2-44)$$

Generally, the repulsive Coulomb interaction among charges along the polyelectrolyte extends the polymer chain. In a dilute, salt free solution, the chain is fully extended. When salt is added to the solution, the repulsive Coulomb interaction is reduced and screened belong the Debye length. As a result, the chain reveals a coil conformation at a large scale. On the other hand, at small length scales, e.g. shorter than the Debye radius, the chain remains extended, which leads to an increase in the persistent length:

$$l_p = l_0 + l_e \qquad (2-45)$$

The contribution l_e is known as the electrostatic persistent length.

2.1.5 Single chains at surfaces

The adsorption of a polymer chain from a solution onto a surface is controlled by the free energy changes of the process. Confined on a 2-D surface from a 3-D solution, the chain always loses entropic free energy, which should be compromised by the gain of internal energy during the adsorption process. For a week adsorption, i.e. when the polymer-surface interaction is small, the process is strongly influenced by the entropic elasticity of the polymer chain. On the other hand, for a strong adsorption such as a high negative charge density polyelectrolyte adsorbing onto a positively charged surface, the electrostatic force dominates the process.

A single neutral chain adsorbed at a surface

Fig. 2-2 displays a typical monomer-surface interaction when the polymer is adsorbed onto an attractive surface. When the monomer is too close to the surface, due to the impenetrability of the surface, they repel each other. The potential energy increases sharply and goes to infinity. When the monomer is too far from the surface, it does not feel the influence of the surface. At a distance around the equilibrium length *b*, the system is in balance, and each monomer adsorbed onto the surface contributes ΔE to the gain of the internal energy.

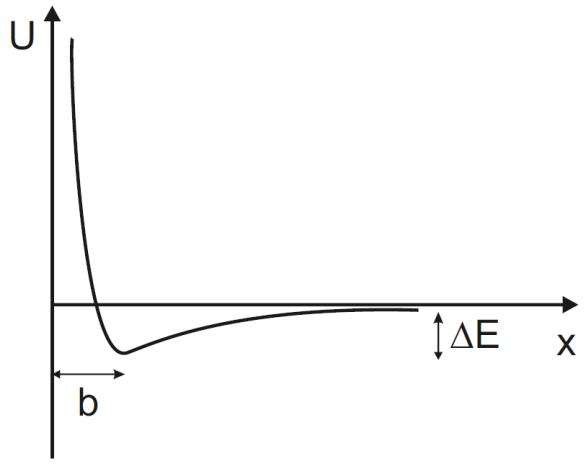

Figure 2-2. Adsorption energy of a monomer *vs* distance on an attractive surface: ΔE denotes the adsorption energy per monomer.

When a flexible chain adsorbs onto a surface, a polymer layer with the thickness of D is formed, which is described in Fig. 2-3.

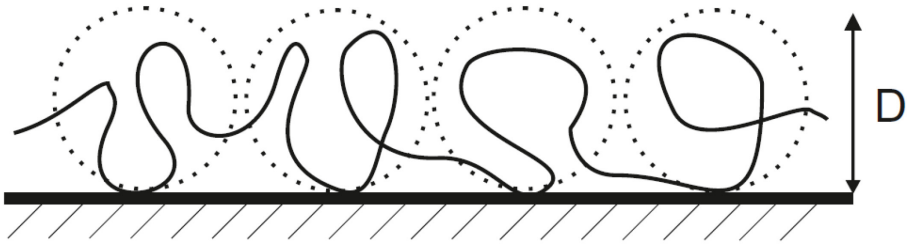

Figure 2-3. Adsorption of polymer with a thickness of D: such a layer can be regarded as a chain of polymer blobs.

The formation of each blob leads to a loss of entropic free energy by k_BT, therefore the total entropic energy loss of a chain is given as follows:

$$S = nk_BT = \frac{N}{(D/a)^{1/v}}k_BT \qquad (2-46)$$

with *n* is the number of blobs, which is described in Eq. (2-35). Suppose the overall number of the monomers, which are confined at the surface is ϕN ($\phi < 1$), the free energy change of the system is

$$F = \frac{N}{(D/a)^{1/v}}k_BT + \phi N\Delta E \qquad (2-47)$$

For a week adsorption, $\phi \ll 1$, the free energy depends on the entropic term.

For a strong adsorption of an ideal chain with $v = ½$, one can assume that the layer is homogeneous, thus $\phi \approx b/D$.

$$F = k_BT\frac{R_0^2}{D^2} + \frac{b}{D}N\Delta E \qquad (2-48)$$

By minimizing *F*, we obtain

$$D \sim \frac{k_BT}{\Delta E}\frac{a^2}{b} \qquad (2-49)$$

Interestingly, the layer thickness does not depend on the length of the chain, but on the adsorption energy and the equilibrium length.

A polyelectrolyte chain adsorbed at a charged surface

The adsorption of polyelectrolytes onto a charged surface is more complicated than the adsorption of a neutral polymer onto an attractive surface. The conformation of polyelectrolytes on the surface depends on the surface properties, such as charge density, surface-polymer interaction, ionic strength, temperature, and so on. The charge per repeating unit of the polyelectrolyte is denoted by *e* and the charge density of the surface by σ. The electrostatic interaction between a repeating unit and the surface area element *dS* is given by:

$$dV = \frac{k_B T l_B \sigma}{r} \exp(-r\kappa) dS \qquad (2-50)$$

Therefore the integral of Eq. (2-50) over the whole surface gives us the total interaction of the surface to a repeating unit,

$$V = \frac{2\pi k_B T l_B \sigma}{\kappa} \exp(-r\kappa) \qquad (2-51)$$

The repeat units within the distance of κ feel the attractive electrostatic force from the surface, which equals

$$f = 2\pi k_B T l_B \sigma \qquad (2-52)$$

and drags the polymer to the surface. The force is balanced by the entropic elasticity and the bending rigidity of the semi-flexible chain. A polymer layer with a thickness of D is formed on the surface (Fig. 2-4).

When the persistence length of the chain is much larger than the thickness of the absorbed layer D, the chain is highly confined in the layer and a new characteristic length, known as the deflection length is introduced to describe the chain statistics. [33] The deflection length is the average distance between two adjacent contact points with the surface. The chain loses roughly k_BT of free energy per contact with the surface.

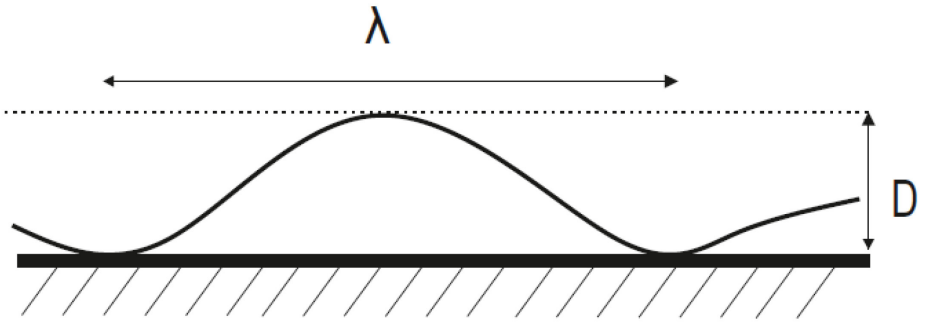

Figure 2-4. A polyelectrolyte chain adsorbs onto a surface when the persistence length is much larger than the thickness of the absorbed layer D. λ characterizes the deflection length, which is the average length between two adjacent contact points with the surface.

2.2. DNA

2.2.1 DNA primary and secondary structure

The double helix model of the deoxyribonucleic acid (DNA) structure was first suggested by Watson and Crick in 1953 based on the experimental results from DNA X-ray diffraction.[34] The double helix structure resembles a spiral ladder, with the two strands being outside of the helix as the sides of the ladder and the base pairs in the middle forming the rungs of the ladder. The strands are made of a sugar-phosphate backbone, within which each phosphor group is linked covalently through a phosphodiester bond to two sugar groups, one with the 3' and the other with the 5' carbon atom of the sugar group. The two strands run anti-parallel to each other, one in 5' to 3' direction and the other in 3' to 5' direction. The helix makes a turn every 3.4 nm, and the distance between two neighboring base pairs is 0.34 nm. Hence, there are about 10 pairs per turn. The width of the double helix is about 2.0 nm. The intertwined strands make two grooves of different widths, referred to as the major groove and the minor groove, which may facilitate binding with specific proteins. This structure is also known as the B-form DNA (Fig. 2-5). The nucleobases (Adenine, Thymine, Cytosine, and Guanine) are connected to a DNA strand via a C-N covalent bond between the nucleobase and the 2' carbon atom of the sugar group. Within the double helix, the nucleobases of one strand together with the

complementary nucleobases of the other stand form base pairs via hydrogen bonds. Adenine (A) binds only to thymine (T), forming 2 hydrogen bonds; while guanine (G) binds to cytosine (C), and forming 3 hydrogen bonds (Fig. 2-5).

The complementary nature of the base-paired structure provides the genetic information encoded within the double-stranded DNA. The difference in the binding energies between the C-G and A-T base pairs brings different stability of the double helix; e. g. DNA with high G-C content is more stable than DNA with high A-T content. The difference in the double helix stability plays an important role *in vivo*. During DNA transcription and DNA replication, the double helix needs to be separated into two single strands, which usually occurs in a high A-T content region. For example, during DNA transcription, the double helix opens in the Pribnow box or TATA box of a promoter, where a very high A-T content exists. [35] In bacteria, e.g. in *Escherichia coli*, replication initiation has been reported to involve the initiator protein DnaA binding to DnaA boxes at the *oriC,*[36] forming a big nucleoprotein complex, which facilitates the melting of a nearby A-T content rich region named DNA-unwinding Element (DUE) [37, 38]. The base pairs lie parallel on one another at a distance of about 3.4 Å. The π-orbitals of the aromatic groups thus overlap, which forms the so-called π-π stacking. The π-π stacking and the hydrogen bonds between base pairs are the two major stability factors for the double helix structure.

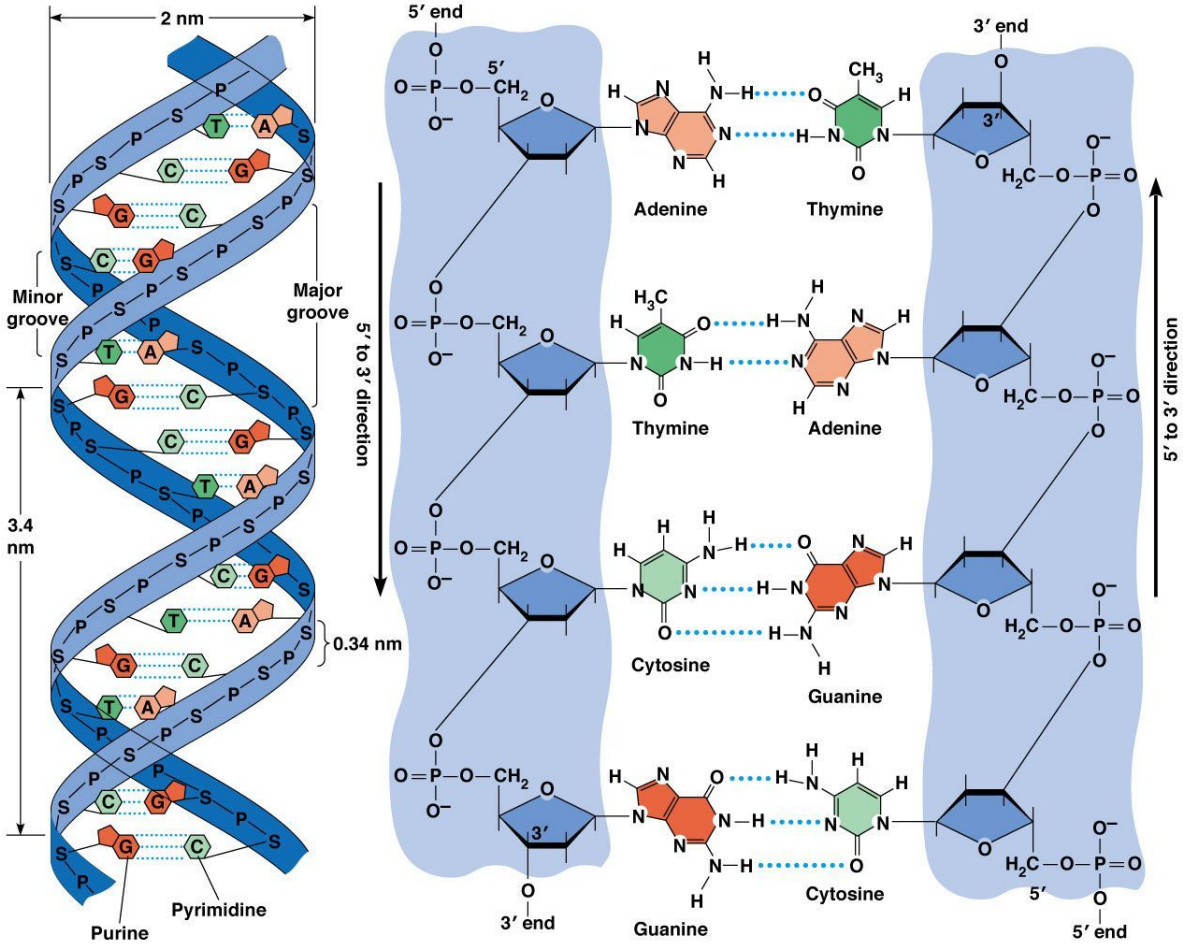

Figure 2-5. DNA double helix structure, strand structure and base pairs. (Image original from Pearson Education, Inc.)

2.2.2 DNA tertiary structure: topological constraint and supercoiling

In the first domain of life, DNA is mostly present in a closed circular shape. The distinctive feature of a closed circular double helix structure is that its topological state cannot be changed by any conformational rearrangement without breaking one of the strands. In topological terms, this property can be described by the linking number (Lk). The linking number is the total number of the two strands crossing each other. If each crossing is assigned a ± 1, with the sign depending on the chain orientation (for DNA the right-handed takes the positive), the linking number is given by

$$Lk = \sum_{crossing} \pm 1 \qquad (2-53)$$

For example, Fig. 2-6 shows two intersecting contours S_1 and S_2. The linking number of the system is the total number of times that S_2 crosses through an imaginary surface which covers S_1. For this case, the linking number is 1.

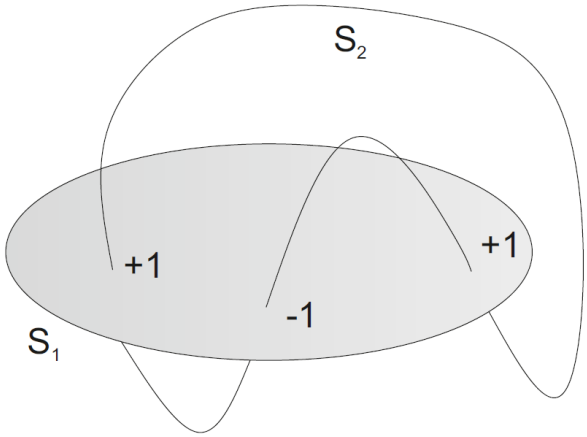

Figure 2-6. The linking number of the two contours S_1 and S_2 equals 1.

Mathematically the linking number is given by the Gaussian integral,

$$Lk = \frac{1}{4\pi}\oint_{S1}\oint_{S2}\frac{(d\vec{r}_1 \times d\vec{r}_2)\cdot\vec{r}_{12}}{r_{12}^3} \qquad (2-54)$$

where $d\vec{r}_1$ and $d\vec{r}_2$ are the vectors along S_1 and S_2, $\vec{r}_{12} = d\vec{r}_2 - d\vec{r}_1$.

The linking number contains two parts, the twist number (*Tw*) and the writhe number (*Wr*). The twist number is equal to the number of times one phosphodiester backbone wraps locally about the other. $Tw = N/\gamma$, where N is the total number of base pairs of a DNA molecule, γ is the number of base pairs per double-helix turn in DNA under given conditions. The writhe number equals to the average number of non-local self-crossings of the double helix. The twist number describes the torsional deformation of the base pairs stacking inside the double helix backbone, while the writhe number describes the deformation of the double helix backbone. Therefore $Lk = Tw + Wr$ remains constant for all conformations without breakage of the strands.

Fig. 2-7 displays cartoons of circular DNA with $Lk = 52$ in different supercoiled states. In the relaxed state, the linking number is equal to the twist number, 52, i.e. the number of times that the two strands locally twist along each other (Fig. 2-7a). In the supercoiled state, the double helix backbone wraps along itself, positive in the right-handed direction and negative in the left-handed direction. In Fig. 2-7b, the double helix backbone wraps along itself three times in the right-handed direction, which gives a value of 3 to *Wr* and reduces *Tw* by 3. On the other hand, in the left-handed direction, *Wr* equals -3, and *Tw* has a value of 55 (Fig. 2-7c). All these three conformations have the same linking number 52.

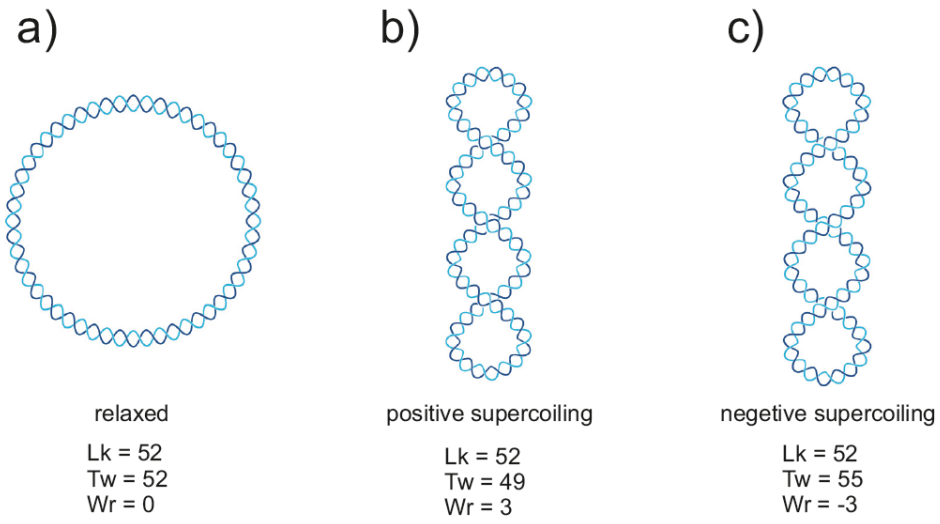

Figure 2-7. Schematic presentations: a) relaxed circular DNA, b) positive supercoiling, and c) negative supercoiling. [39]

Since the linking number is a topological invariant, it is more convenient to use other parameters to describe DNA supercoiling such as the linking number difference ΔLk and the superhelix density σ,

$$\Delta Lk = Lk - N/\gamma \qquad (2-55)$$

$$\sigma = \Delta Lk/Lk_0 = \Delta Lk \cdot \gamma/N \qquad (2-56)$$

where N is the total number of base pairs of a DNA molecule, and γ is the number of base pairs per double-helix turn in DNA under given conditions.

The value of ΔLk can be determined experimentally by gel electrophoresis or sedimentation experiments. Superoiling makes the DNA molecule more compact, which leads to an increase in the mobility of the molecule in gel electrophoresis or an increase in the sedimentation constant.[40] Experimental results showed that for a given circular DNA the distribution of ΔLk is a normal distribution and this can be described as

$$P(\Delta Lk) = A\exp\left[-\frac{(\Delta Lk)^2}{2\langle(\Delta Lk)^2\rangle}\right] \qquad (2-57)$$

Experimental data also showed that for $N > 2500$,

$$\langle(\Delta Lk)^2\rangle/N = Constant$$

More generally the distribution of a DNA supercoiled state is given by its corresponding supercoiling free energy $F(\Delta Lk)$

$$P(\Delta Lk) = A\exp\left[-\frac{F(\Delta Lk)}{k_B T}\right] \qquad (2-58)$$

Therefore it follows

$$F(\Delta Lk) = Bk_B T(\Delta Lk)^2/N \qquad (2-59)$$

where B is a constant. In a physiological solution (0.2 M NaCl), B = 1100.[41, 42] The whole chain is under topology-induced stress in a supercoiled state. This stress can be released either by torsional deformation of the base pairs stacking (changes of *Tw*) or by deformation of the double helix backbone (changes of *Wr*). For sufficiently high negative supercoiling, the partial break of the double helix into two single strands occurs, which cannot be described by Eq. (2-59) but rather involves mechanical studies of DNA. In the following section, I will provide an overview of studies on single DNA mechanics.

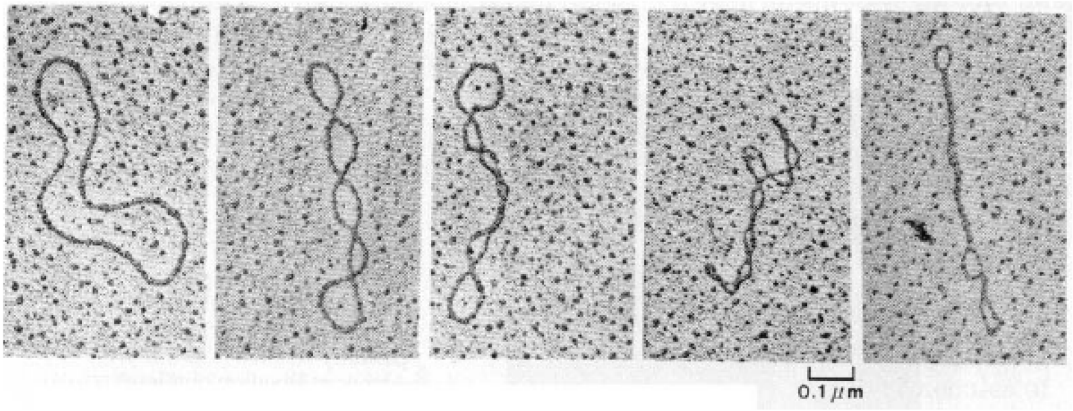

Figure 2-8. Images of supercoiled plasmids (5 kb) obtained by electron microscopy.[43] The degree of supercoiling increased from left to right.

2.2.3 DNA mechanical properties

Stretching single DNA

The elastic properties of single ds-DNA chain have been explored by stretching the molecule with micromanipulation methods such as pulling with an SFM tip,[12, 14, 44] micropipettes[1] and optical tweezers[2, 45]. Fig. 2-9 demonstrates a typical force-extension curve recorded in such experiments. The x-axis is the relative extension of DNA compared with its original length. Careful inspection reveals that the force-extension curve can be divided into 4 regimes: A) the entropic elasticity regime, B) the intrinsic elasticity regime, C) the B- to S-form transition regime, and D) highly stretched regime.

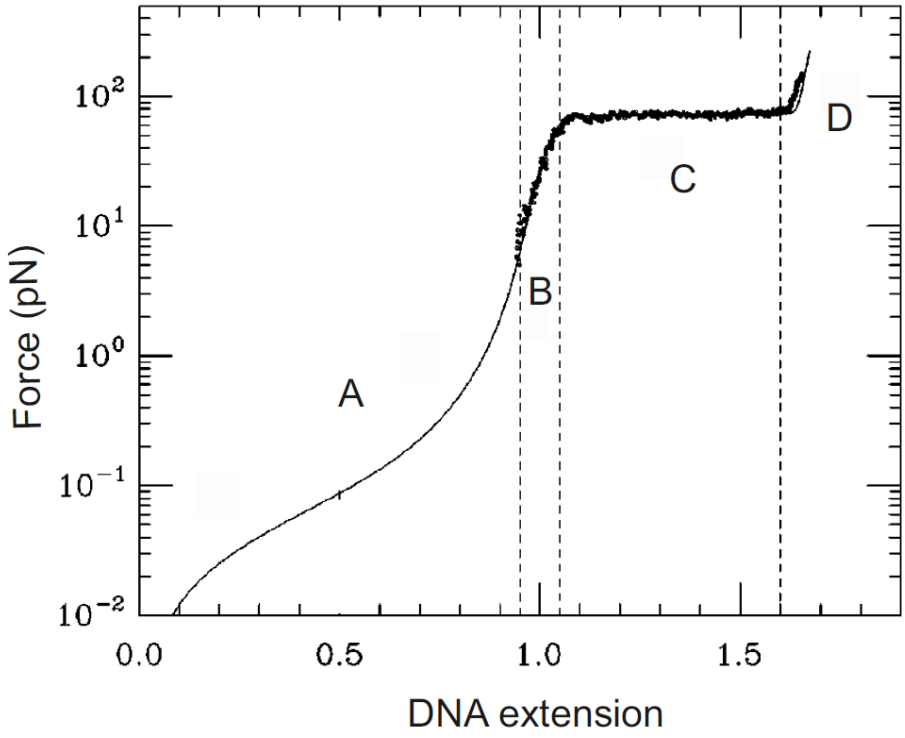

Figure 2-9. Force vs. relative extension curve in a typical DNA stretching experiment. Four regimes are revealed: A) the entropic elasticity regime, B) the linear intrinsic elasticity, C) the highly cooperative structural transition, D) and the highly stretched regime.[46]

A. The entropic elasticity regime

At large length scales a DNA chain coils up due to thermal fluctuations. The end-to-end distance is much smaller than the contour length. In order to align the chain, an external force is needed to stretch the chain. This elasticity is of pure entropic nature of the long polymer chain. The thermal energy is on the scale of k_BT. Therefore the typical force scale in the entropic elasticity regime is $f \sim k_BT / l_p \approx 0.1$ pN, where l_p is the persistence length of DNA and has a value of around 50 nm.

The entropic elasticity of DNA can be described by the freely-joint chain (FJC) and the worm-like chain (WLC) models (details see previous section). In the WLC model, the force is related to the DNA extension by:[47]

$$f = \frac{k_BT}{l_p}\left(\frac{1}{4\left(1-\frac{x}{L}\right)^2} + \frac{x}{L} - \frac{1}{4}\right) \qquad (2-60)$$

Compared with FJC model, the WLC model gives a better fit at low and intermediate forces (0.1 ~ 10 pN) (Fig. 2-10). In the fitting, the persistence length takes a value of 53 nm.

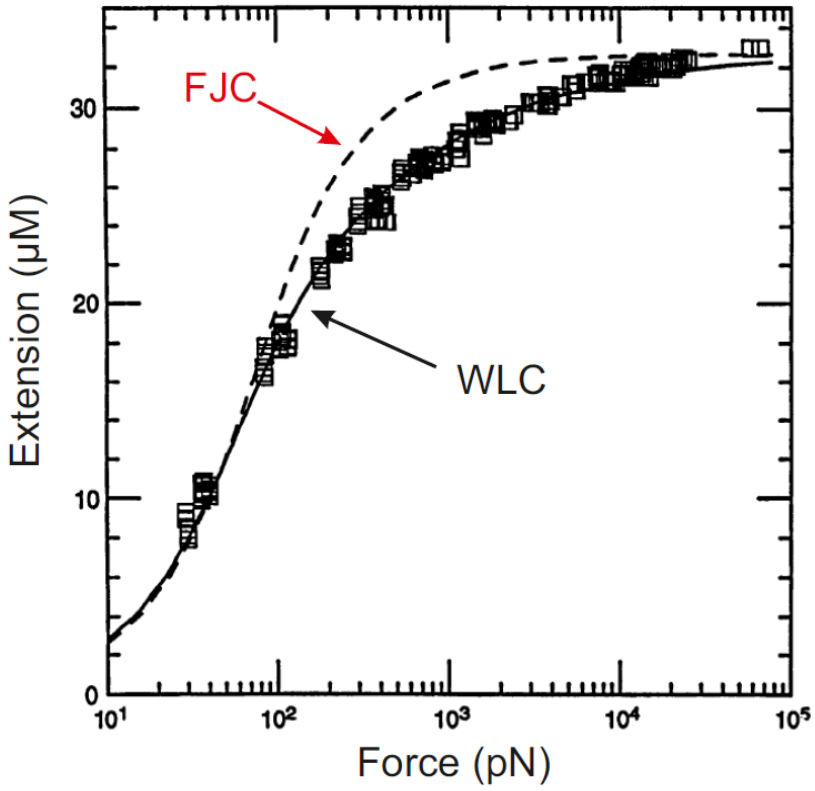

Figure 2-10. Force-extension data from stretching a 97 kbP λ-DNA fitted with the worm-like chain (solid line) and the freely joined chain (dashed line) model. A persistence length of 53 nm was taken for the fitting. [47]

B. The intrinsic elasticity regime

Between 10 and 70 pN, the DNA extension grows linearly according to the external force. The external force completely suppressed the entropic elasticity of the chain and the DNA responses to an external force like an elastic rod with a Young's modulus *E*. Therefore one can write

$$\frac{f}{X} = E\left(\frac{x-L}{L}\right) \qquad (2-61)$$

where *X* is the area of cross section of DNA.

Knowledge of the bending rigidity (persistence length) allows one to estimate the Young's modulus of a DNA chain under small forces. The Young's modulus of an elastic rod with a uniform cross-section is given by

$$E = \frac{4A}{\pi r^4} = \frac{4 l_p k_B T}{\pi r^4} \qquad (2-62)$$

where *r* is the radius of the rod. The double helix DNA has a diameter of 1 nm and a persistence length around 50 nm. A Young's modulus around 300 MPa is obtained, which agrees with the results of other numerical calculations.[2]

C. The B-form to S-form transition

When the stretching force reaches about 70 pN, ds-DNA undergoes a highly cooperative structural transition. In this regime, within a very narrow force window, the extension increases dramatically, mainly from around 110% in the beginning of the transition to 170% of its original B-form length at the end of the transition.[1, 2] An increase around 70% in length strongly implies a rearrangement of the double helix internal structure. A new structure, named the S-form DNA was suggested based on experimental observations and results from steered molecular dynamics simulation.[1, 2, 48] The new S-form DNA is about 70% longer than the B-form. The exact structure of S-form DNA depends on which ends of the double helix are being pulled. Pulling on the two 3′ ends unwinds the double helix, forming a ladder like structure. Pulling on the two 5′ ends preserves the helical structure, with tiled base pairs and a smaller inner diameter (Fig. 2-11).

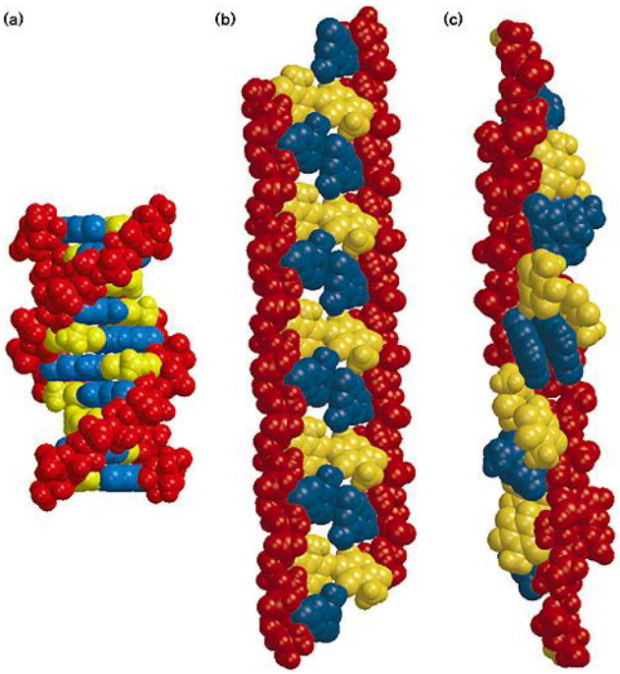

Figure 2-11. Comparison of B-form and S-form DNA: a) B-form, b) S-from DNA induced by pulling at two 3' ends, c) S-form DNA induced by pulling two 5' ends[48]

Pulling on only one strand of each ends indicates that the chain is allowed to rotate along the backbone axis to release the torsional stress. The chain is not under a torsional constraint. Later it was demonstrated that S- to B-form DNA transition occurred at around 70 pN only for a nicked ds-DNA, i.e. one of the strand is broken and the chain is freely to rotate. For an un-nicked ds-DNA the transition takes place at 110 pN.[3]

D. The highly stretched and bond rupture regime

In this regime, the chain is further extended up to 2.1 times the length of its original B-form length before finally it breaks.[11, 49] The strength of the covalent bonds in the DNA backbone is tested. The phosphodiester backbone consists of single C-C, C-O, and C-P covalent bonds. DNA was ruptured by a dynamic flow and a tensile strength of 480 pN was obtained. [11] DNA could stand a force up to 1.7 nN before it broke in pulling with an SFM tip experiments[50]. These values are still smaller than that of a typical single bond obtained experimentally or calculated from the bond potential, such as 2 nN for a single Si-C and around 4 nN for a single

C-C bond.[14] However, the DNA tensile strength depends on the length of the molecule, i.e. the number of covalently connected bonds along the backbone. Solvent effect plays also an important role in the DNA stability, such as the hydrolysis of the phosphordiester backbone. Most interestingly, the tensile strength depends on the force loading rate, i.e how far one pulls the DNA molecule.[16, 51] The differences in the reported experimental values may be caused by the different characteristic time scales of each experimental set-up. Therefore pulling and breaking DNA under a constant force is an attractive new approach to explore the time-dependent mechanical properties. In the "Result and discussion" section I will address the DNA time dependent mechanical properties in detail by using a "blowing manipulation" method, which allows a combination of a dynamic load and a static load on single DNA chains.

Twisting and bending single DNA

At large length scales, the single DNA chain can be very well described by the WLC model, which characterizes the polymer chain with one parameter, the persistence length l_p. The value of the persistence length is half of the Kuhn length. In the WLC model, the chain bends smoothly along its contour and the correlation between two chain segments decays exponentially with the distance between them. After a characterized distance l_p, the initial orientation of the chain is forgotten. Each chain segment can be regarded as an elastic rod with a bending rigidity A. The bending rigidity of the DNA chain is related to its persistence length by:

$$A = l_p k_B T \qquad (2-63)$$

The bending energy which is required to bend a DNA fragment of length L into an arc through an angle θ is given by

$$\xi_{bend} = \frac{l_p k_B T L}{2r^2} = \frac{l_p k_B T}{2L}\theta^2 \qquad (2-64)$$

where r is the radius of the arc.

This bending energy has to be overcome when a long DNA chain is packed into the relatively small nucleus or the capsid. For example, the double-stranded DNA of bacteriophage ϕ29 has 19.3 kilo base pairs, which is 6.6 μm in length. The whole DNA is packed into a roughly tube shape capsid with a radius of 42 nm and a height of 54 nm. From Eq. (2-64), a bending energy in the order of 100 k_BT is needed to be overcome. The packing is finished by the DNA packing motor: a portal complex that hydrolyses ATP.[52] The motor has to overcome not only the bending energy but also the entropic and electrostatic energy of packing DNA into the capsid.

Supercoiling is another type of DNA packing. In a supercoiled state, the double helix backbone coils around itself, this leads to a further reduction of the DNA size. DNA supercoiling can be achieved by twisting DNA. Twisting DNA adds a torsional stress to the whole chain, which is released by DNA supercoiling. Therefore DNA supercoiling results from a balance between the bending energy cost of these tertiary structures and the torsional energy gained. Again, we can treat the DNA as an elastic rod with length L and twisting rigidity C. If we fix one end of the tube, rotate and simultaneously stretch the other end with a force f, the torque Γ increases linearly with the twist angle θ.

$$\Gamma = \frac{C}{L}\theta \qquad (2-65)$$

The elastic rod remains straight until a critical torque and twist angle is reached, the rod locally buckles and forms a loop of radius r. Therefore the torsional energy gained is

$$\xi_{twist} = 2\pi\Gamma \qquad (2-66)$$

The energy cost is the bending energy and the work against the constant force f,

$$\begin{aligned}\xi_{cost} &= \xi_{bend} + W \\ &= \frac{AL}{2r^2} + 2\pi r f \\ &= \frac{\pi A}{r} + 2\pi r f\end{aligned} \qquad (2-67)$$

By minimizing the energy cost according to the radius of the loop,

$$\frac{d\xi_{cost}}{dr} = 0$$

one obtains

$$r = \sqrt{\frac{A}{2f}} \qquad (2-68)$$

Therefore,

$$\xi_{min} = 2\pi\sqrt{2Af} \qquad (2-69)$$

And the critical torque at which the rod start to buckles is

$$\Gamma_c = \frac{\xi_{twist}}{2\pi} = \frac{\xi_{min}}{2\pi} = \sqrt{2Af} \qquad (2-70)$$

The twisting rigidity can be directly determined by twisting and stretching a single DNA with a magnetic bead. Fig. 2-12a shows the schematic representation of the experiment. A DIG/biotine end-labeled DNA molecule (16mm long) is attached at one end to a glass surface by DIG/anti-DIG bonds and at the other to a 2.8 mm magnetic bead via streptavidin/biotin links. By varying the distance between the sample and permanent magnets the stretching force is kept constant while rotating inducing DNA supercoiling. The sample is placed on an inverted microscope and viewed with a 63× objective. The force is measured by a real time video analysis of the bead's Brownian fluctuations: the greater the force, the more restricted are its fluctuations. The linking number difference ΔLk equals the number of turns that the magnetic bead rotates.[53, 54] Fig. 1-12b shows the DNA's end-to-end distance *vs* $\Delta\sigma$ under certain constant stretching forces. At a low stretching force (~ 0.2 pN), the torsional behavior of DNA is somehow symmetric. The torsional stress (both + σ and - σ) is released by DNA supercoiling. The degree of supercoiling (*Wr*) increases with $|\sigma|$, resulting in further decrease at the DNA extension. At moderate forces (~ 1 pN), the DNA extension curve becomes asymmetric. Positive twisting shows an elastic rod like behavior: the chain keeps straight until a critical

value is reached. After that the chain supercoils. The extension decreases almost linearly according to the number of turns. Negative twisting does not affect the extension. The torsional stress is attributed to melt partly the double helix instead of supercoiling.

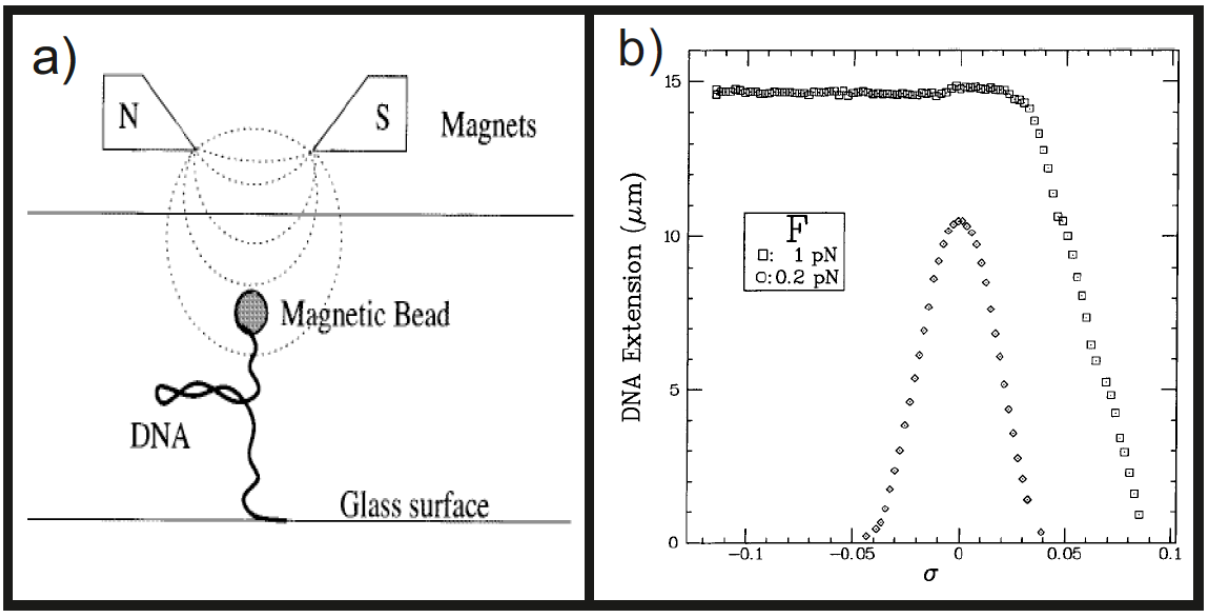

Figure 2-12. a) Schematic set up of stretching and twisting DNA with magnetic beads, b) extension *vs* supercoiling for a stretching force of 0.02 pN (circles) and 1 pN (square). [53-55]

The twisting rigidity and the energy required to melt the double helix can be obtained by comparing the work required to stretch an overwound ($\sigma > 0$) and an underwound ($\sigma < 0$) DNA chain. Fig. 1-11a displays the force-extension curves of DNA with different degrees of supercoiling. Let us denote A_+ and B_+ as two states in stretching overwound DNA, A_- and B_- in stretching underwound DNA, A_0 and B_0 for the non-supercoiled DNA. State B_+ can be achieved in two ways. We can first twist A_0 *n* times to achieve A_+ (with a torsional energy $\xi_{twist}^{A_+}$) and then stretch A_+ to B_+ (with a torsional energy $\xi_{twist}^{B_+}$). Alternatively, we first stretch to B_0, and then twist B_0 *n* time to achieve B_+. Due to the energy conservation, we should have

$$\xi_{twist}^{A_+} + \Delta W_0^+ = \xi_{twist}^{B_+} = \frac{C}{2L}(2\pi n)^2 \qquad (2-71)$$

where ΔW_0^+ is the work difference between stretching a non-supercoiled and an overwound DNA. Similarly we can write for the underwound DNA

$$\xi_{twist}^{A-} + \Delta W_0^- = \xi_{twist}^{B-} \qquad (2-72)$$

Negative twisting causes DNA to melt partly. The DNA melting occurs after a critical torque Γ_c is reached. After that the torsional energy is used to melt the DNA double helix, and Γ_c saturates for further increasing twist. Therefore

$$\xi_{twist}^{B-} = \frac{C}{2L}(2\pi n_c)^2 + \xi_D \qquad (2-73)$$

where ξ_D is the melting energy:

$$\xi_D = 2\pi(n - n_c)\Gamma_c \qquad (2-74)$$

Subtracting Eq. (2-74) by Eq. (2-73), and noting that at low forces $\xi_{twist}^{A+} = \xi_{twist}^{-}$, one obtains

$$\Delta = \Delta W_0^+ - \Delta W_0^- = \frac{2\pi^2 C}{L}(n - n_c)^2 \qquad (2-75)$$

where Δ presents the work difference as shown by the shaded area in Fig. 2-13a. By plotting $\sqrt{\Delta}$ *vs n*, one obtains the twisting rigidity *C* from the slope of the linear line (Fig. 2-13b):

$$\frac{C}{k_B T} = 86 \pm 10\ nm \qquad (2-76).$$

From the intercept of the line with the x-axis, one obtained $n_c = 66$ and $\Gamma_c = 9$pN nm. The melting energy per base pair can also be calculated,

$$\epsilon_D = \frac{\xi_D}{10.5\ (n - n_c)} = 1.35\ k_B T \qquad (2-77).$$

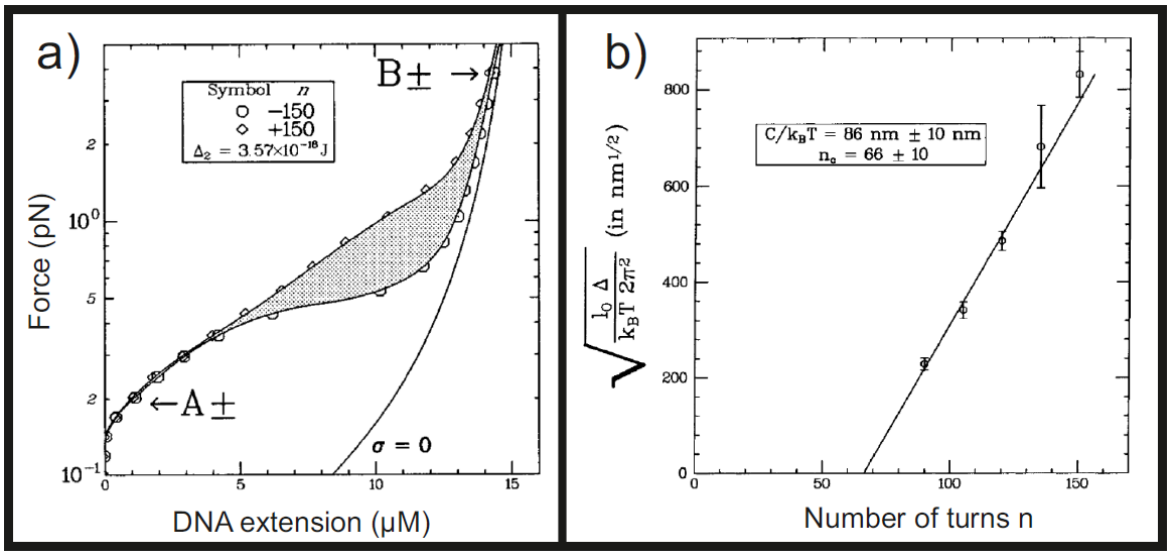

Figure 2-13. a) Work difference (grey part) between stretching an overwound (quadrangles) and an underwound (circles) DNA; b) work different *vs* number of twisting turns, the torsional modulus was presented by the slope of the curve. [53-55]

Twist-stretch coupling

DNA is regarded as an elastic rod in the studies on its mechanical properties. In the previous section, mechanical parameters such as the Young's modulus *E*, the bending rigidity *A*, and the twist rigidity *C* have been discussed. However a forth parameter, known as the twist-stretch coupling *δ*, is needed to introduce in order to better describe the DNA's behavior under tension. The twist-stretch coupling describes how the torsional mechanical properties vary upon stretching, and *vice versa*. When DNA is stretched and twisted, where the stretching force is large enough to overwhelm the thermal bending of the chain, the total energy of the chain can be described as: [5, 56, 57]

$$\xi = \frac{C}{2L}\theta^2 + \delta\frac{x}{L}\theta + \frac{EX}{2L}x^2 \qquad (2-78)$$

where *X* is the DNA cross section area, *L* is the contour length, and θ is the twist angle. For a double helix structure like ds-DNA, a negative coupling is expected, which means that stretching induces underwinding of DNA. Surprisingly, in an experiment twisting and stretching single DNA with a magnetic bead, for small extensions a positive coupling was

measured, i.e. DNA overwinds when stretched. The inverse effect was also detected with the same set-up: overwinding results in lengthening of the chain. A model is also suggested to explain these unusual mechanical properties. DNA is modeled as an elastic inner rod (grey) wrapped helically by a stiff wire (red). When stretched, the inner rod decreases its diameter, and the outer wire can wrap a larger number of times, i.e. an increase in the twist number (Fig. 2-14). [5]

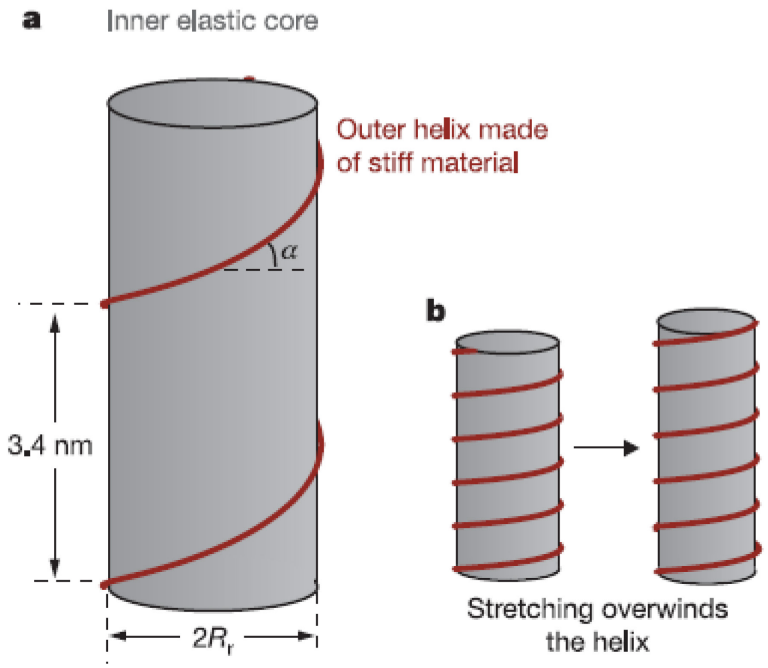

Figure 2-14. a) DNA as an elastic inner rod (grey) wrapped with a stiff wire (red). The pitch is 3.4 nm and the diameter of the rod is 1nm.b) Stretching DNA reduce the diameter of the inner core, therefore the wire wraps more turn, i.e. the DNA overwinds. [5]

2.3. Amphiphilic cylindrical polymer brushes

2.3.1 Introduction and synthesis of cylindrical polymer brushes

Besides the linear and the ring polymer discussed in the previous section, polymers have diverse topologies such as star polymers, polymer brushes, branched polymers, polymer networks, and dendrimers. Polymer brushes refer to a collection of polymer chains with one end attached to a linear polymer chain, a planar surface or a spherical particle. In the first case, the polymer is also known as "cylindrical polymer brush" or "molecular polymer brush". Fig. 2-15 demonstrates different structures of cylindrical polymer brushes with different backbones and side chains. Due to their various architectures and functionalities, cylindrical polymer brushes find their applications in template synthesis,[58, 59] molecular actuators,[60] as synthetic substitutes for proteoglycans,[61] and as giant surfactants. [29]

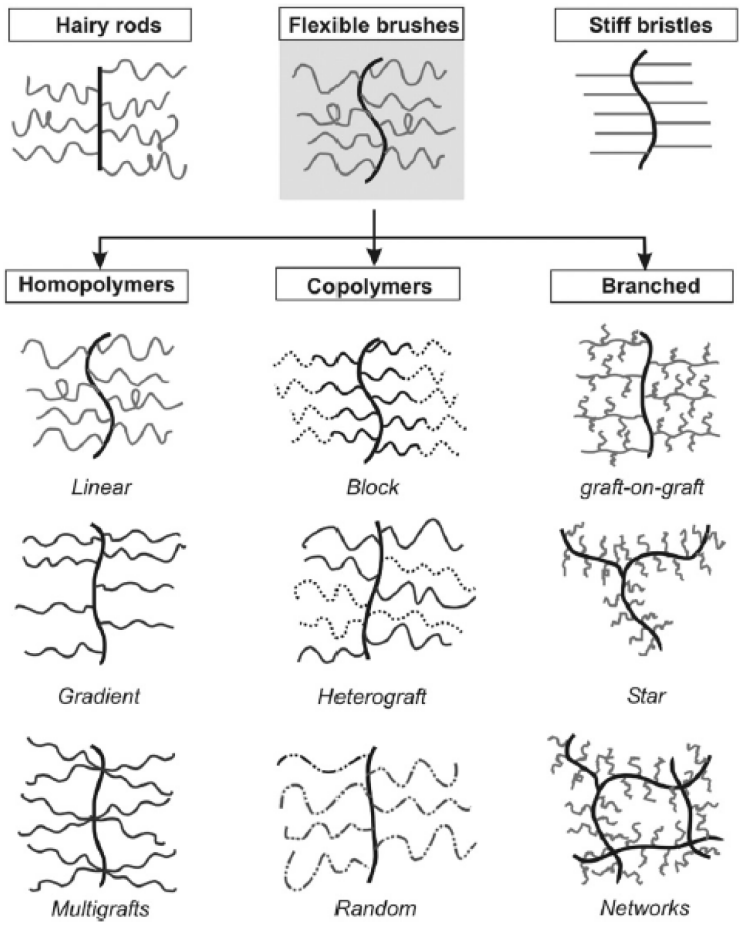

Figure 2-15. Different topologies of cylindrical polymer brushes

Fig. 2-16 shows the three main approaches to the synthesis of cylindrical polymer brushes: "grafting to", "grafting through", and "grafting from". [62] In the "grafting to" method, the side chains and the functional linear main chain are first prepared separated and then the side chains are grafted to the functional sides along the linear main chain via coupling reactions such as "click chemistry". In the "grafting through" method, sides chains with double bond end groups are first prepared, used as macromonomer and polymerized directed in the presence of initiator to form the cylindrical molecular brushes. The "grafting from" method was first introduced by the group of Matyjaszewski in 1998.[63] A linear main chain is first prepared followed by attaching initiating groups along the chain, resulting in a macroinitiator chain with many active sites. The final product is achieved by polymerization of side chains at the active sites.

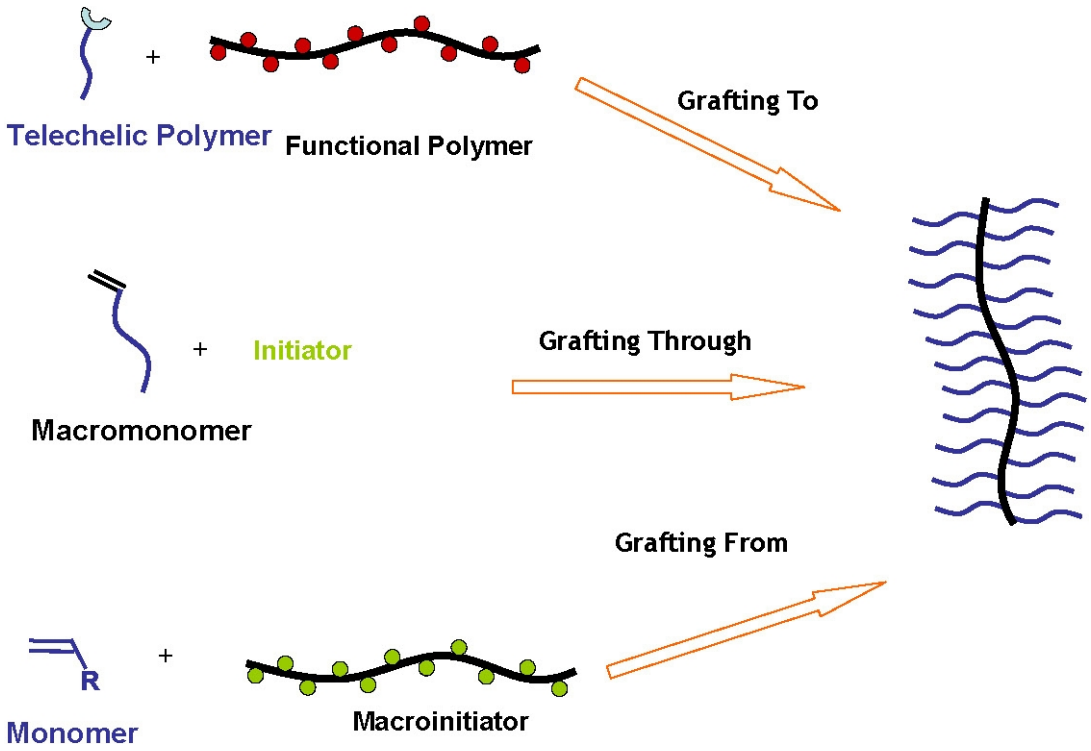

Figure 2-16. Three different strategies to synthesize cylindrical polymer brushes [62]

The most attractive advantage of "grafting to" is that both the side chains and the backbone are prepared separately. Different polymerization methods and reaction conditions are chosen according to the chemical nature of side chain monomers and backbone monomers. However a coupling step is needed to attach the side chains to the main chain. In order to increase the grafting density the reaction is usually run under an access of the side chains via most efficient and high yield reaction types such as click chemistry[64] and nucleophilic substitution.[65] "Grafting through" was the first method introduced by Tsukahara to prepare homopolymer brushes.[66] High grafting density homopolymers can be achieved in this method via different polymerization methods such as radical polymerization,[67] anionic polymerization[68] and ring opening polymerization.[69, 70] Copolymerization of two different macromonomers to prepare copolymer brushes was also reported.[71, 72] The most characteristic figure of this method is that every repeating unit of the backbone is covalently linked with one side chain, resulting in 100% grafting density. Well-defined side chains can be prepared before polymerization. The disadvantage of this method is also obvious. Due to the high grafting density and the large steric repulsion between the side chains, the degree of polymerization and the conversion is highly hindered. The "grafting from" method is so far the most successful way to prepare relatively high grafting density cylindrical molecular brushes with well-defined side chains and backbones. *In situ* growing of the side chains at the active sites of the backbone makes the steric repulsion less relevant compared with "grafting through" and "grafting to" methods.[62] Brushes with homopolymer, copolymer backbones, and gradient brushes were achieved by tailoring the backbone structure. By varying the chemical composition of the side chains, brushes with random and block-copolymer side chains as well as homopolymer were synthesized. However, this method provides less control on the length and the grafting density of the side chains compared with "grafting through" method.

2.3.2 Conformation of single cylindrical polymer brushes

Conformation in solution

The steric repulsion between the densely grafted side chains plays an important role in the molecular conformation. In a good solvent, the repulsive interaction between the side chains overwhelms the entropic elastic of the backbone, and therefore straightens the backbone. The whole molecule reveals a worm-like cylindrical conformation, which is characterized by the persistence length (l_p), the cylinder diameter (D), and the length per monomer (l_m). With the growth of the side chains, l_m increases and saturates at a maximum value of 0.25 nm. On the other hand, the persistence length and the diameter of the cylinder also increase and it was suggested that the ratio l_p/D is roughly constant with $l_p/D \sim n^{9/8}$,[73] where n is the degree of polymerization of the side chains.

Conformation transition

For some functional cylindrical brushes, the transition from cylindrical to globular conformation is triggered by external stimuli such as change of temperature, pH or ionic strength, and light. For example, cylindrical brushes with thermally responsive poly(*N*-isopropylacrylamide) side chains undergo a conformation transition when the temperature crosses its lower critical solubility temperature (LCST), which leads to a sharp decrease of the radius of gyration R_g and the hydrodynamic radius R_h at the LSCT. The constant molar mass excludes the argument that the size reduces due to the polymer decomposing (Fig. 2-17). Similar transitions were also observed for cationic polypeptide brushes triggered by the change of ionic strength.[74]

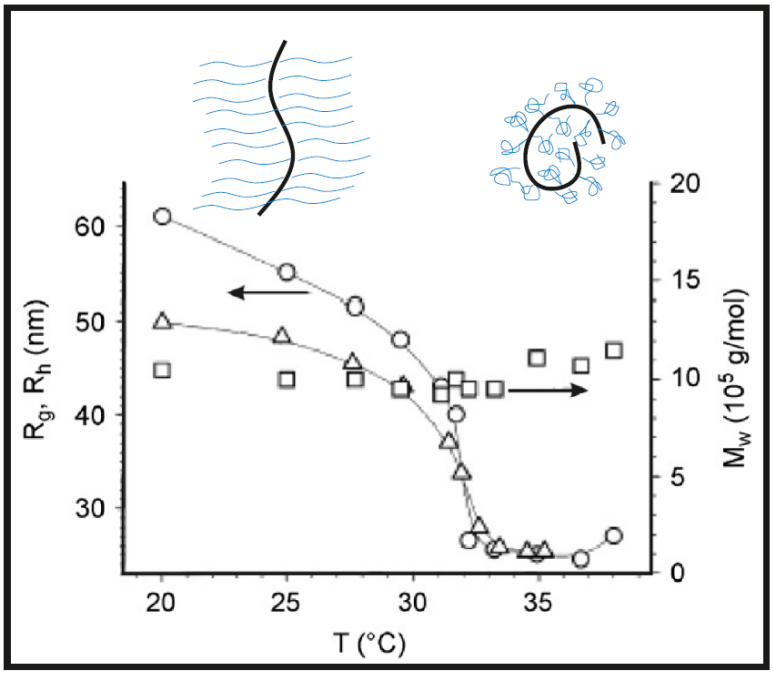

Figure 2-17. Radius of gyration R_g (circle), hydrodynamics radius R_h (triangle), and molar mass (square) of PNIPAM brushes *vs* temperature.[75]

Conformation on surfaces

The conformation of single polymer brushes on surfaces depends on the interaction between the side chains and the surface as well as the steric repulsion interactions between the side chains. The contour length, persistence length, and brush width of the polymer are directly accessible by SFM at surfaces.

Adsorbed from a 3D solution to a 2D flat surface, the polymer brushes lose one degree of freedom. Therefore the steric repulsion between the side chains intensifies, which straightens the backbone further compared to the conformation in solution. Absorbed on an attractive surface, the backbone of a homopolymer brush extends to nearly fully stretched length. The persistence length depends on the side chain length by $l_p \sim n^{\alpha}$, where n is the degree of polymerization of the side chain. A value of $\alpha = 2.7$ was obtained experimentally for homopolymer brushes, which fitted the theoretical value $2 < \alpha < 3$.[76] For highly grafted polymer brushes, the stretching effect induced by the adsorption of the side chain on the surfaces was large enough to break the covalently linked backbone.[77] When adsorbed on a

repulsive surface, the cylindrical polymer brushes exhibit globular conformations in order to minimize contact with the surface.

For cylindrical brushes with block copolymer side chains, the conformation on the surface mainly falls into three categories (Fig. 2-18). When the two blocks have similar attractive affinity to the surface, flat and extended side chains are obtained, as shown in Fig. 2-18a. When one of the polymer blocks has higher affinity to another, it tends to adsorb on the surface while the other avoid contacting the surface, resulting in a folding back conformation as shown in Fig. 2-18b and c.

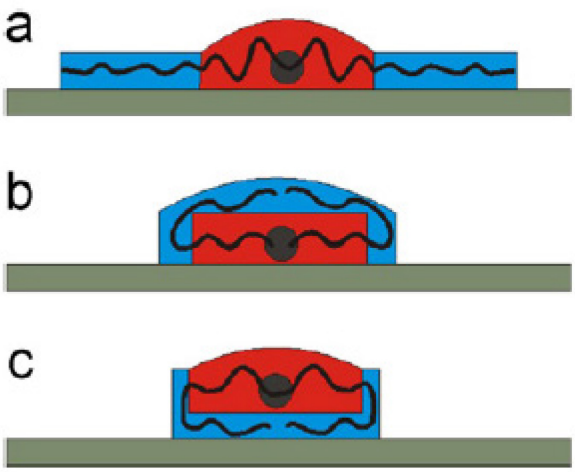

Figure 2-18. Adsorption of polymer brushes with block copolymer side chains on a surface: a) both side chain blocks have good affinity to the surface, b) and c) the surface attracts one block but repels the other. [78]

2.3.3 Amphiphilic cylindrical polymer brushes

Block polymer brushes with amphiphilic hetero side chain blocks are known as "giant surfactant",[29] which is characterized by their large molecular weights and an enormous number of possible molecular architectures and supramolecular structures in solution. Compared with small molecule surfactants with a typical molar mass from 200 to 600 g/mol and a block copolymer "macro surfactant" with a representative molar mass from 2000 to 50 000 g/mol, a "giant surfactant" may exceed a molar mass of 200 000 g/mol. The pre-

structured amphiphilic side chains of the "giant surfactant" by chemical bonding provide more complex molecular structures in different solutions.

Fig. 2-19 demonstrates possible molecular structures of amphiphilic cylindrical molecular brushes. Cylindrical polymer brushes with amphiphilic block copolymer side chains form core-shell structures in an aqueous solution and inverse core-shell structures in an organic solvent (Fig. 2-19a, b).[58] Polymer brushes, which were made by alternating copolymerization of hydrophilic and hydrophobic macromonomers form Janus-like structures (Fig. 2-19c). [79] Polymer brushes composed of one hydrophilic and one hydrophobic brush exhibit dual brush structures (Fig. 2-19d).[29]

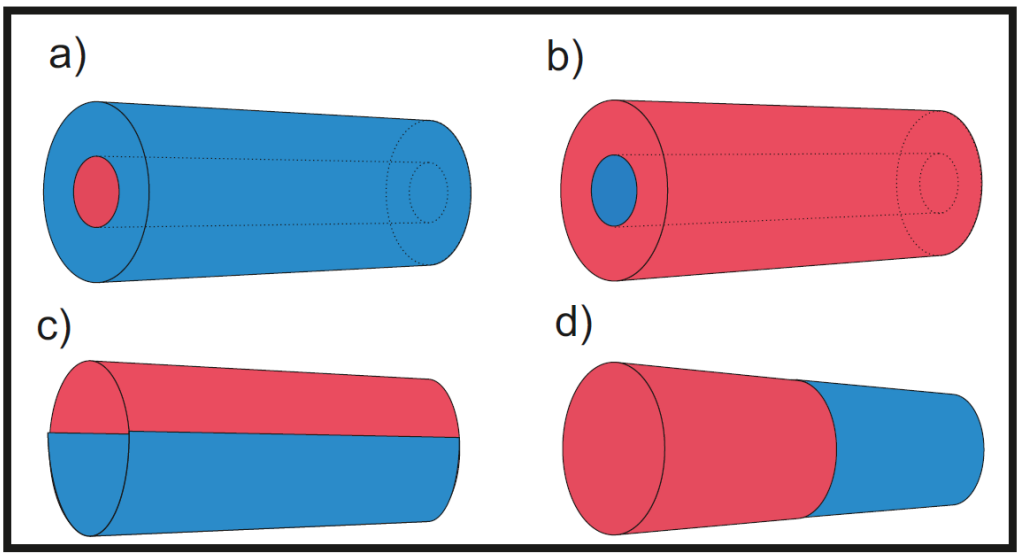

Figure 2-19. Possible topologies of amphiphilic polymer brushes: a) core-shell, b) inverse core-shell, c) Janus-like, and d) dual brush. Blue indicates the hydrophilic part and red the hydrophobic part. [29]

Theoretically, amphiphilic dual brush block copolymers can be prepared in three different strategies (Fig. 2-20). The first one combines two "grafting through" synthesis steps. Hydrophilic and hydrophilic macromonomers are sequentially polymerized. The second approach involves coupling of two pre-synthesized hydrophilic and hydrophobic cylindrical brushes. This approach requires a highly efficient coupling reaction such as "click" chemistry. However due to the poor incompatibility of hydrophilic and hydrophobic brushes, this approach

is limited to coupling of two hydrophilic polymers. The third approach combines two "grafting from" steps. Macroinitiators with two different types of active sites are first prepared. These two different active sites are accessible to hydrophilic, and the other to hydrophobic side chains, respectively.

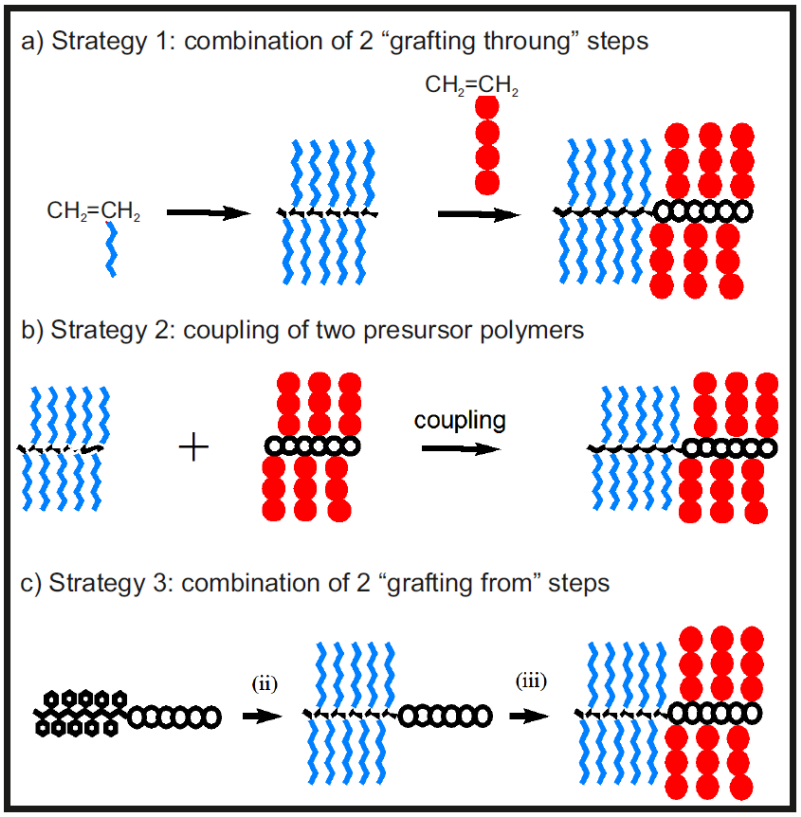

Figure 2-20. Synthetic strategies to amphiphilic dual brush block copolymers. [30, 31]

Conformation of amphiphilic cylindrical polymer brushes

The studies on conformation and structure of amphiphilic cylindrical polymer brushes in aqueous solution and on surfaces were carried out and the results are discussed in the Results and Discussion section.

2.4. Hyperbranched polyglycerol (hPG) as nanocarrier system for drug delivery

2.4.1 Drug development and challenge

Around 40 to 60% of new drug candidates possess poor aqueous solubility. The solubility issue of drug candidates became a major challenge for the pharmacist in new drugs development. Although there are several ways to state the absolute solubility of a solute, for biopharmaceutical purposes, a solubility description focused on the clinical dose is appropriate.

Based on biopharmaceutical classification system (BCS), [80] a drug candidate is regarded as sufficiently solubile when its highest dose could be dissolved in 250 mL or less of buffer within pH 1~7.5; if more than 250 mL is required the drug candidate is defined as poorly soluble. BCS classifies drug candidates into four categories in terms of their aqueous solubility and permeability through biological membranes (Fig. 2-21). Class I drugs are both highly soluble and highly permeable and tend to have good oral bioavailability. Class II drugs have good bioavailability but poor solubility. The formulation methods that enhance solubility could "move" class II candidates into class I.

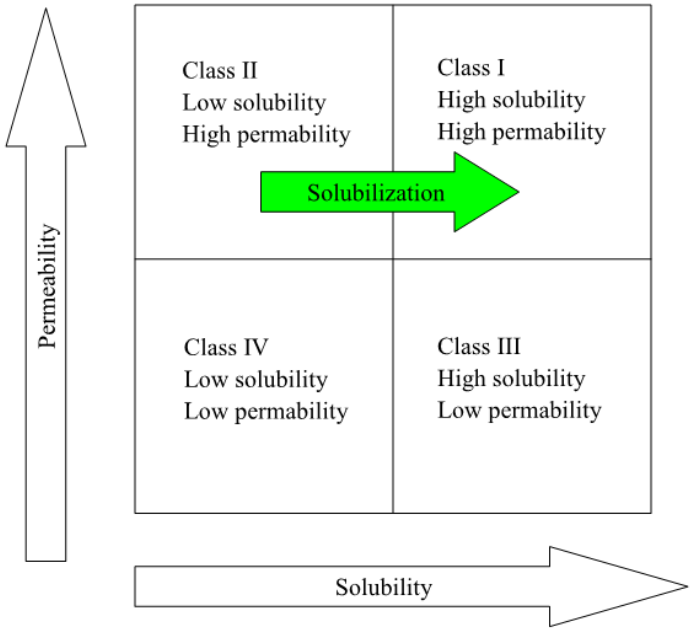

Figure 2-21. Biopharmaceutical classification system (BSC) of drug candidates [80]

Solubilization techniques

There are available ways to improve the solubility of drugs, including co-solvents, pH adjustment, salt formation, complexation, and amorphous solid micelles formed by small surfactant. The techniques can be used individually or in combination to enhance the solubility of drugs.[81-83] All these methods are successful to some extent, but all do have disadvantages for oral or parental administration. Altering pH or salt makes use of a higher solubility of the ionic form of the solute, but it has potential issues of chemical stability of drugs and biocompatibility of pH extremes. Co-solvent technique use mixtures of water and physiologically acceptable organic solvents, such as propylene glycol, ethanol, and glycerin; to improve solubility has the issue of a pharmacological effect of organic solvents and possible precipitation of drugs upon dilution. Complexation could shift monomer forms of drugs into complexes with complexing agents, such as cyclodextrin, and improve solubility. The drug strongly interacting with a complexing agent leads to slow release rates of drugs from complexes. Even though amorphous solids could be applied to enhance the solubility of drugs, they exhibit poor long term physical/chemical stability.[84] To improve the solubility of potential drugs and increase therapeutic effectiveness, a number of macromolecular delivery systems, such as block copolymers and dendritic polymers, are under investigation. Nanocarrier systems based on amphiphilic macromolecules for drug delivery have become increasingly interesting in recent years due to the unique properties of these polymer systems, such as their enhanced permeability and retention (EPR) effect into tumor tissue,[85, 86] and their high aqueous solubility and biocompatibility. They help to improve therapeutic efficiency and lower toxicity by increasing drug solubility and by a targeted delivery and controlled release.

2.4.2 Block Copolymers

Amphiphilic block copolymers form micelles by self-assembly in water due to hydrophobic interactions when the concentration increases above the critical micelle concentration (CMC) (Fig. 2-22). Compared with micelles formed by small surfactant molecules, polymeric micelles have generally a lower CMC. Therefore they are more stable and retain the loaded drug for a longer period of time.[87] The size of block-copolymer micelles is determined by thermodynamic parameters, but partial control over the size is possible by variation of the block length of the polymer.[88] In general, these block copolymer micelles are 20-50 nm in diameter with a relatively narrow distribution and are similar in size to viruses, lipoproteins and other transport systems.[87] Block copolymers based on polyethylene oxide (PEO) and polypropylene oxide (PPO) blocks, commercially known as Pluronics^{TM} have been used for solubilization of drugs such as indomethacin, haloperidol, amphotericin B, doxorubicin, and digoxin. [89, 90] A major problem for these nanocarrier systems is their nonspecific uptake by the reticuloendothelial systems (RES). Therefore, the size and the surface properties of the nanocarrier based on block copolymers require careful design to achieve long circulation times in the blood and site-specific drug delivery. Furthermore polymeric micelles are not very stable at varying conditions like upon changes of temperature and pressure used in sterilization. They also break apart when the concentration is lower than its critical micelle concentration (CMC). Therefore the polymer concentration needs always to be kept above the CMC during application, which leads to an increase in dose and toxicity.

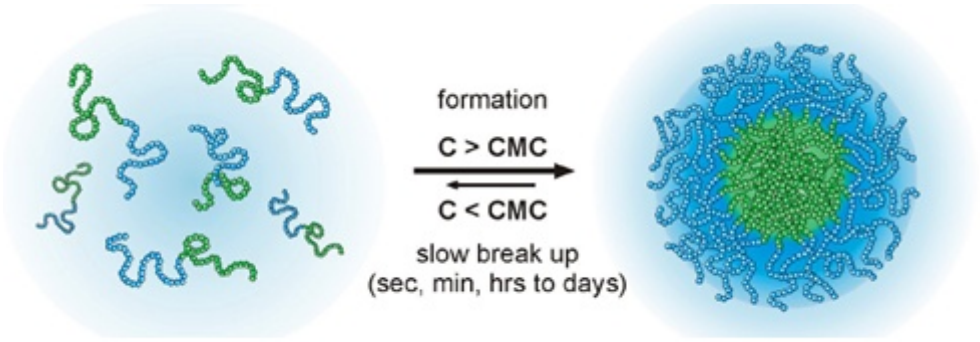

Figure 2-22. Formation of micelles by amphiphilic linear polymer [87]

2.4.3 Dendritic polymers

Single amphiphilic dendritic and star polymer molecules behave like micelles in aqueous solution. They are known as unimolecular polymeric micelles (UPM).[91] Unlike polymeric micelles, unimolecular polymeric micelles (UPM) are stable under shear stress or in high dilutions. Dendritic polymers can be prepared by controllable branching chemistry. Therefore, they possess a unique dendritic structure with attractive features, including their nano-size range, rigid globular structure with high physical stability, and a large number of peripheral functionality for versatile chemical modification.[92] Because of these unique properties, the emerging role of dendrimers in pharmaceutical fields has been highlighted by their extensive applications for therapeutic and diagnostic purposes, including the passive or active delivery of anticancer drugs,[93] noncovalent encapsulation of guest molecules (Fig. 2-23),[94] contrast agents,[95] and nucleic acid drugs.[96]

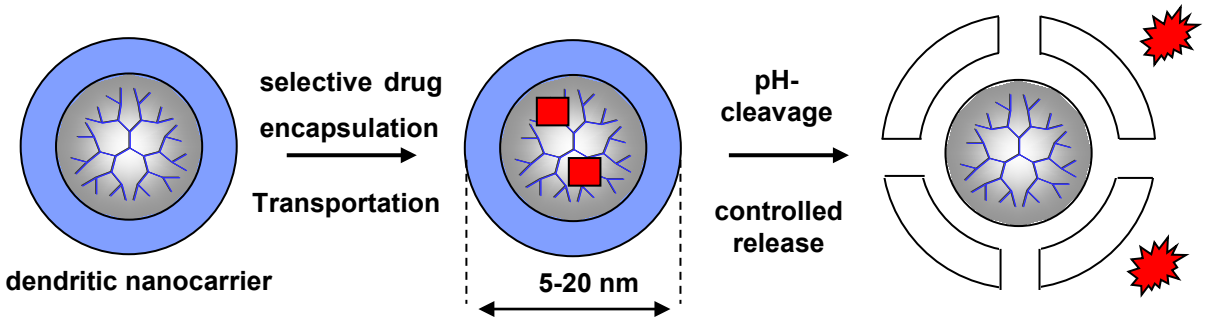

Figure 2-23. Unimolecular dendritic nanocarrier for encapsulation of guest compounds such as drugs. Guest molecule can be release in acidic media such as tumor tissue when the acid labile linkers are cleaved. [94]

As a general principle for designing dendrimers, there are many critical factors, such as their biocompatibility and pharmacokinetic characteristics, before dendrimer-based drugs can be used as biomedicines. In association with alterations in the toxicity and bio-distribution of dendrimers and dendrimer-based drugs, the dendritic structure, modification and physicochemical properties of dendrimers have been reported as following.

Dendrimers

Dendrimers, consisting of a central core, an internal cavity, and peripheral groups, are well-defined and highly branched macromolecules which govern a globular structure with mono-dispersity. Dendrimers are generally synthesized stepwise using divergent or convergent methods.[97] According to the divergent method, first developed by the Tomalia and Newkome groups, dendrimers grow exponentially outwards by conjugation of repeated branch units to the end groups of the central core. On the other hand, there is the convergent synthesis developed by the Fréchet group starting from the periphery of dendrimers toward the central core, in which this part is termed “dendron” and finally linking to the core molecule to introduce a complete dendrimer.[98] Generally, a theoretically mono-disperse dendrimer size can be obtained by both synthetic methods. However, a perfectly dendritic structure of a higher generation dendrimer could be successfully prepared by the convergent method due to the lower steric hindrance of the crowded peripheral groups during synthesis.[99]

A vast number of dendrimers have been designed with structural differences used in biological applications, including poly-amido-amines (PAMAM),[100] poly-propylene-imines (PPI),[101] polyamides or polypeptides,[102] polyester dendrimer.[103] Recently, poly-triazole dendrimers synthesized by "click chemistry"[104] and "geometrically disassembling" or degradable dendrimers have been developed for controllable structure cleavage by light, enzymes or single triggering events[105] This is a new concept in dendrimer chemistry for improved biological applications although these approaches are still in their infancy. Some dendrimer structures are presented in Fig. 2-24.

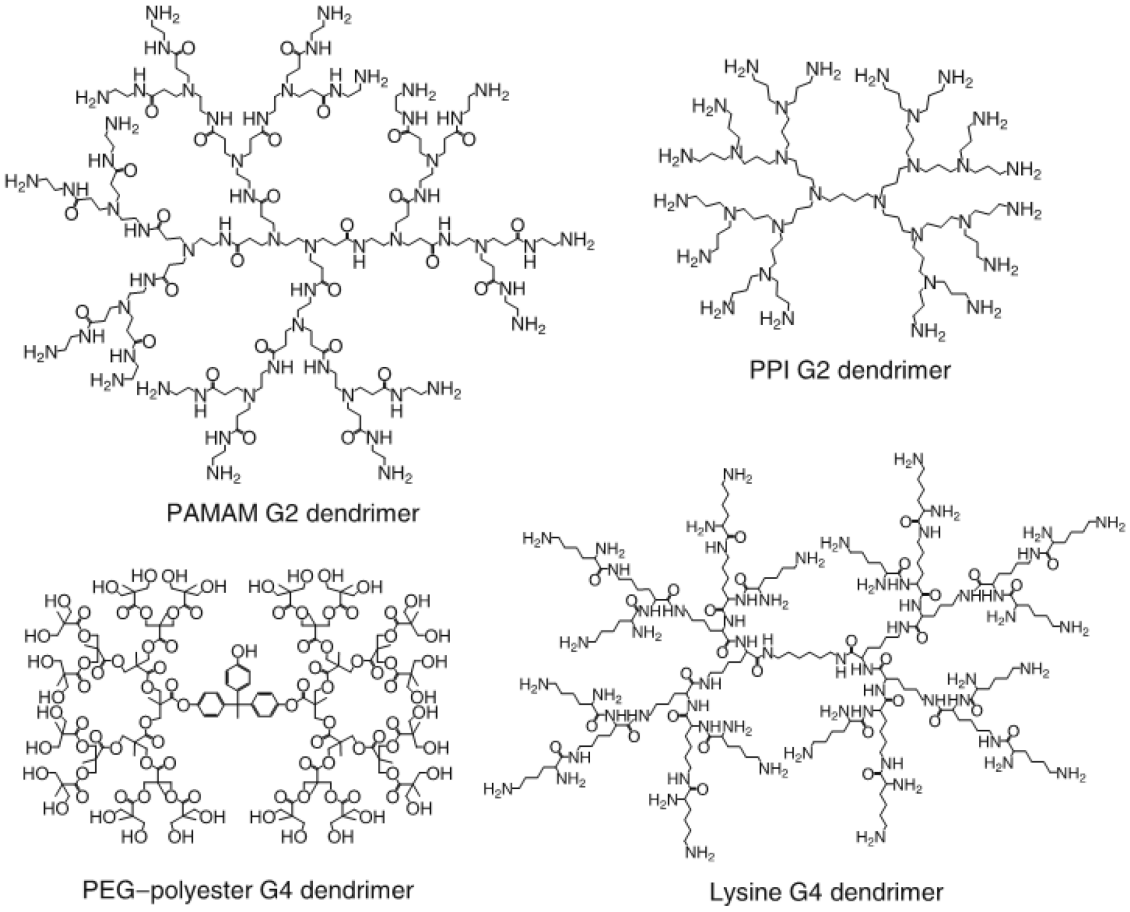

Figure 2-24. Examples of dendrimers used in biomedical application [100, 101, 103]

Hyperbranched Polyglycerol (hPG)

Kim and Webster introduced the term of "Hyperbranched Polymer"[106] when they synthesized soluble hyperbranched polyphenylene. Compared with a dendrimer that was synthesized by a multistep reaction, a hyperbranched polymer can be obtained by a single reaction step. For this reason, the problematic purification, especially for higher generation dendrimers is avoided. The main advantages of hyperbranched polymers are their low price and relatively well defined structure. In some cases the imperfect structure of hyperbranched polymers is even helpful for applications in drug or gene delivery and organic synthesis.[107]

Hyperbranched polyglycerol (hPG) was synthesized through ring-opening multi-branching polymerization (ROMB) of glycidol in the Mülhaupt group in 1999.[32, 108] Fig. 2-25 demonstrates the synthesis steps. The outcoming hPG is an amorphous material, which exhibits very good water solubility and biocompatibility. The biocompatibility of hPGs with different scaffolds was evaluated *in vitro* for blood compatibility, viscosity, complement activation, platelet activation, plasma protein precipitation, and cytotoxicity. In all cases PG appeared to have very little effect on the tested parameters and outperformed PEG in some cases which makes hPG an excellent candidate for drug solubilization and delivery.[109]

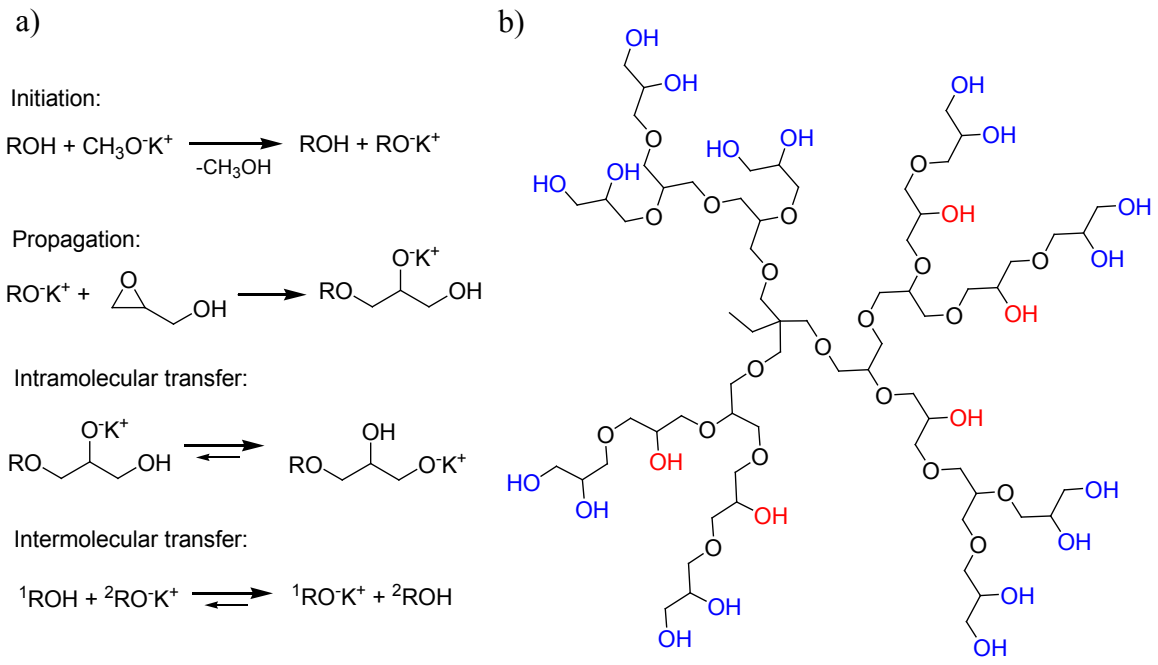

Figure 2-25. a) Anionic ring-opening multibranching polymerization of glycidol and b) schematic structure of hyperbranched polyglycerol used 1,1,1-tris(hydroxymethyl)propane (TMP) as initiator. [110]

Another important figure of hPG as carrier is that its transportation capacity is tunable through chemical modification on the polymer shell and core. In contrast to glycerol dendrimers, hyperbranched PG has terminal OH groups on the periphery of the polymer as well as linear OH groups in the core (Fig. 2-25). Chemical modification of the linear OH and the terminal OH groups tune the affinity of the polymer to the guest molecules and the solvent as well. For example, introduction of unipolar groups such as aromatic groups or fluorinated chains to the core increases the hydrophobicity and enhances the affinity to hydrophobic drugs.[94, 111]

Interactions in dendritic based drug delivery systems

There are two major types of interaction between dendritic polymer hosts and drug guest molecules: non-covalent and covalent interactions. Both types of interaction are widely used in drug delivery systems. In the covalent interactions, the drug molecules were covalently linked

in the dendritic polymers by hydrolysable or biodegradable linkages to get controllable and efficient drug formulations.[112, 113] Special targeting moieties can be further attached to get a favored distribution of drug cargo in the specific targeted cells and tissues. In the case non covalent interaction, it can be classified into different forms according to the types of interaction: (1) electrostatic interaction between the oppositely charged dendritic polymers and drug molecules, (2) hydrophobic or π-π interactions between the interior cavities of dendritic polymers and drugs, (3) hydrogen-bond, van der Waals, or ion-dipole interactions.

An example of electrostatic interaction between dendritic polymers and a drug molecule has been described by Xu and coworkers.[114] They reported the titration of various amine-based drugs (guest molecule) to the negatively charged carboxylate based G4 PAMAM dendrimer and positively charge PAMAM. The dendrimer drug interaction was monitored by the chemical shifts in NMR spectra. The location of the drugs on the dendrimer was suggested. They concluded that the cationic drug molecules attached on the surface of carboxylate based PAMAM by electrostatic interaction, whereas an anionic drug was localized at the surface of PAMAM, and the neutral drug sat in the core of PAMAM (Fig. 2-26). The strength of these interactions is based on the pKa values of the molecules.[114]

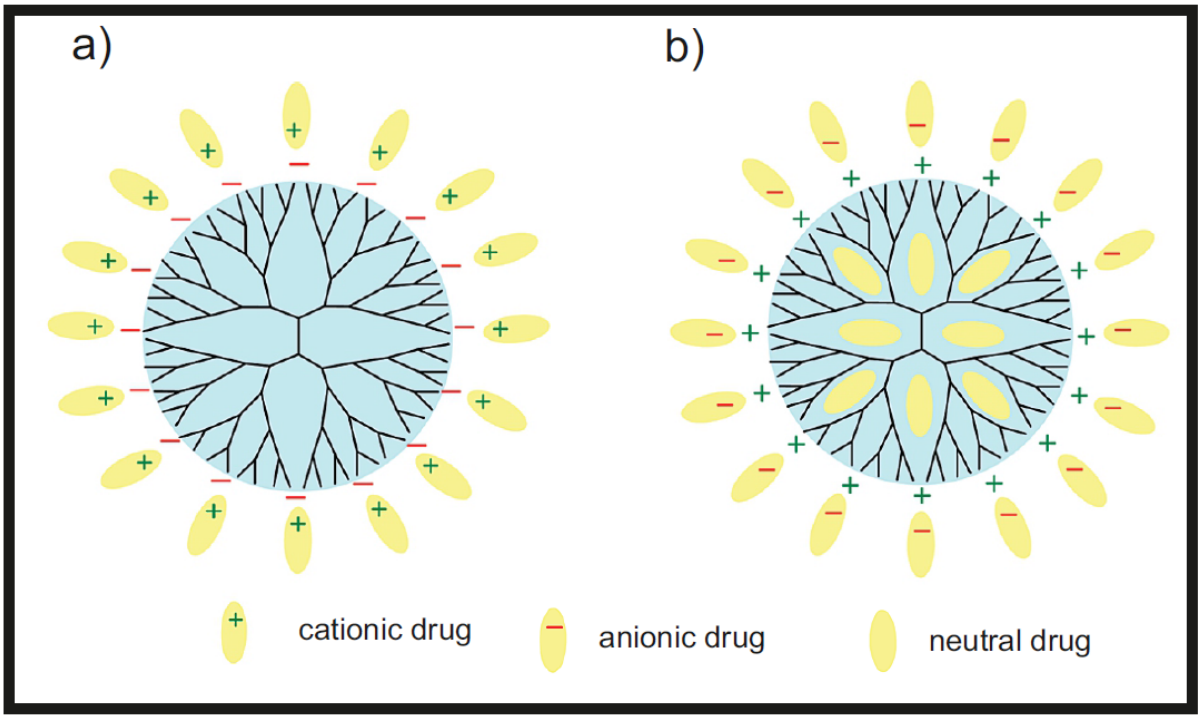

Figure 2-26. Dendrimer drug complexes: a) positively charges drugs locate only at the surface of negatively charged carboxylate terminated PAMAM, b) negatively charged drugs distribute themselves at the surface as well as inside the PAMAM molecules. [114]

π-π interactions between the interior cavities of dendritic polymers and drugs have been demonstrated using an UV-VIS spectroscopy technique by Turk and coworkers. They showed strong specific π-π interactions of polyglycerol derivatives with biphenyl groups in the core of the polymer and the aromatic guest molecules such as pyrene and nimodipine.[111]

3. Experiments and Data Analysis

3. 1. Scanning Force Microscopy and data analysis

The conformation of single polymer molecules on surfaces in this work was mainly investigated by Scanning Force Microscopy (SFM), which belongs to the Scanning Probe Microscopy (SPM) family. SPM utilizes a very sharp tip, which is typically from nano-size down to a few atoms across the tip, to scan back and forth over the surface of a sample. During the scanning, the interaction between the tip and the sample surface is recorded from point to point. The SPMs are classified according to the tip-sample interaction. For example, the Scanning Tunneling Microscopy (STM) records the tunneling current between the tip and the substrate; SFM records the force; Electrostatic Force Microscopy (EFM) the electrostatics interaction; Scanning Near Field Optical Microscopy (SNOM) the fluorescence. The strength of the interaction is then correlated to form an image of the sample, proving information such as topography. STM is the first microscopy of this kind. After that a vast family of the SPM has been developed.

SFM is the most widely used SPM. It finds its applications in various fields of science such as surface science, soft material, microbiology, nano-science and so on. The Van der Waals force between the tip and the sample is included in the Lennard-Jones potential:

$$V_{LJ} = 4\varepsilon\left[\left(\frac{\sigma}{r}\right)^{12} - \left(\frac{\sigma}{r}\right)^{6}\right]$$

$$= \varepsilon\left[\left(\frac{r_m}{r}\right)^{12} - 2\left(\frac{r_m}{r}\right)^{6}\right] \qquad (3-1)$$

where ε is the depth of the potential well, r_m is the distance at which the potential reaches its minimum, and r is the tip-sample distance. When the tip approaches the sample surface from a far distance, an attractive force exists, which reaches its maximum at r_m. A repulsive force is recorded when the tip contacts the sample, and it increases dramatically, when the tip approaches further.

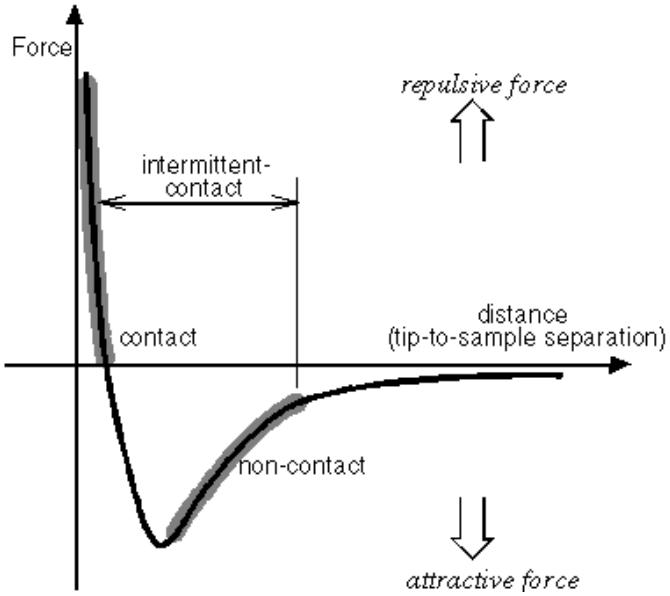

Figure 3-1. Forces *vs* distance between tip and sample. (Paolo Samori's Dissertation, Humboldt Universität zu Berlin, 2000)

The force between the tip and the sample is monitored by the deflection of a cantilever on which the tip is mounted. A laser beam focuses on the end of the cantilever and the reflected beam is detected by a position sensitive detector (PSD), which consists of an array of photodiodes. The deflection signal is used as a feed-back for the controller to control the movement of the piezo-scanner to keep the deflection of the cantilever constant (constant force mode). The movement of the scanner in Z-direction represents the height of the surface.

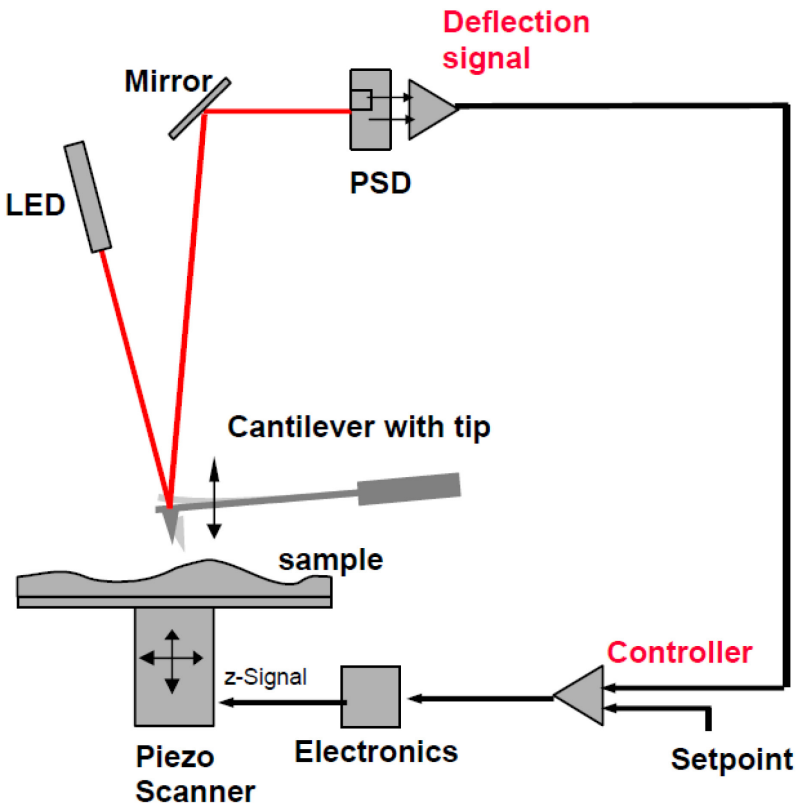

Figure 3-2. Working principle for SFM: the interaction between the tip and the sample is presented by the deflection of a soft cantilever. The deflection is measured by a laser beam and a position sensitive detector, which acts like a fit-back signal to control the movement of the piezo scanner through a computer. The surface topology is given by movement signal of the scanner in Z-direction.

Depending on the samples and the sample properties that should be measured, different SFM modes can be used. There are three main modes: Contact mode, noncontact mode and tapping mode.

Contact mode

Most of early SFMs employed contact mode only, in which the tip is in contact with the sample surface all the time during the measurements. Thus the tip samples the surface in the repulsive region of the Lenard-Jones potential. The contact mode can be rather destructive; therefore it is not suitable for soft surfaces, such as typically found in biomaterials. There

tapping mode is preferred. However, the manipulation of nano-particles on surfaces and the so-called nanolithography utilize the contact mode.

Non-contact mode

In order to measure the local electric or magnetic properties of the sample surface, the non-contact mode is used. In noncontact mode, the tip is set close to the surface, but not in contact with the sample, and either the columbic interaction between the tip and the sample is measured (known as Electric Force Microscopy) or the magnetic interaction between tip and sample is measured (known as Magnetic Force Microscopy). In noncontact mode, the tip samples the surface in the attractive region of the Lennard-Jones potential. Thus the effect of friction and the capillary forces are minimized while the effect of the electric force or the magnetic force is emphasized. Since the tip does not contact the sample, the sample surface is not damaged during the experiment.

Tapping mode

Since the contact mode damages the samples and the noncontact mode cannot provide high lateral resolutions due to the relatively large tip-sample distance, the tapping mode is a solution to this problem. In tapping mode, the tip is oscillating near its resonance frequency over the sample surface, periodically tapping the surface. The tip-sample force is oscillating between the attractive region and the repulsive region in the Lennard-Jones potential. As a first approximation, the tapping cantilever can be modeled as a driven damped harmonic oscillator. The equation of motion reads:

$$\frac{d^2x}{dt^2} + 2r\frac{dx}{dt} + \omega_0^2 x = \frac{f_0}{m}\cos(\omega t) \qquad (3-2)$$

where

$$r = \frac{B}{2m}, \qquad \omega_0 = \sqrt{\frac{k}{m}}$$

B is the damping constant, k is the spring constant, and f_0 is the driven force.

The general solution for the steady state is:

$$x(t) = \frac{f_0}{Z_m \omega}\cos(\omega t + \varphi) \qquad (3-3)$$

where

$$Z_m = \sqrt{B^2 + (\omega m - {}^{k}/_{\omega})^2}, \qquad \tan\varphi = {}^{B}/_{(\omega m - k/\omega)}$$

Z_m is the absolute value of the impedance. And ϕ is the phase of the oscillation relative to the driving force. The phase shift of the cantilever's oscillation is reflected in the phase image. Scanning in tapping mode disturbs the samples only weakly and provides a relatively high spatial resolution; thus it is suitable for most biological samples.

Tip Broadening effect and tip characterization

The size of the tip plays an important role in the resolution of an SFM image. Ideally, an SFM tip with one single atom at the apex gives the "true" size of an object. However, the typical radius of a commercial silicon tip is about a few nanometers, for example 7 nm from an Olympus tip used in this work (Fig. 3-3). Therefore before the apex of the tip reaches the object, the tip already "sees" the object. An artifact is induced by the tip (the dark area in Fig. 3-4a). This phenomenon is known as "tip broadening" in SFM imaging. The "tip broadening" effect becomes significant when the object has structure sizes in the range of the tip radius or smaller, i.e. in nanometer range. For example the width of a DNA molecule is typically around 15 nm as measured by SFM instead of with the true width of 2 nm. In order to reconstruct the image to give a "true" topography of a sample surface, one needs to characterize the tip geometry.

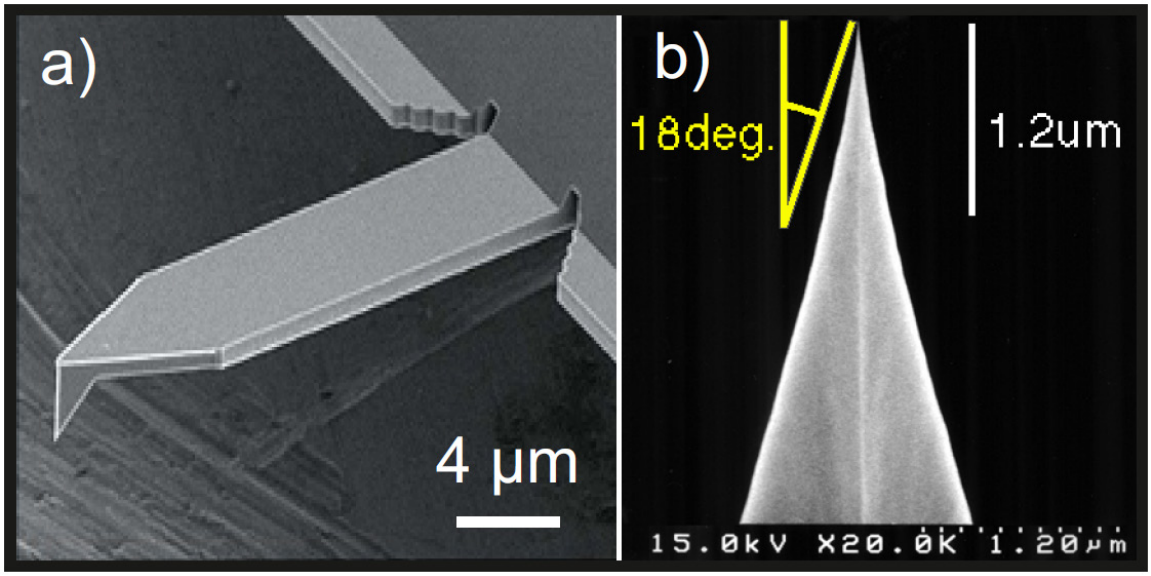

Figure 3-3. SEM images of a commercial cantilever and tip from Olympus: a) the dimension of the cantilever is 160 × 40 μm, b) the radius of the apex is typical 7 nm. (From Olympus website)

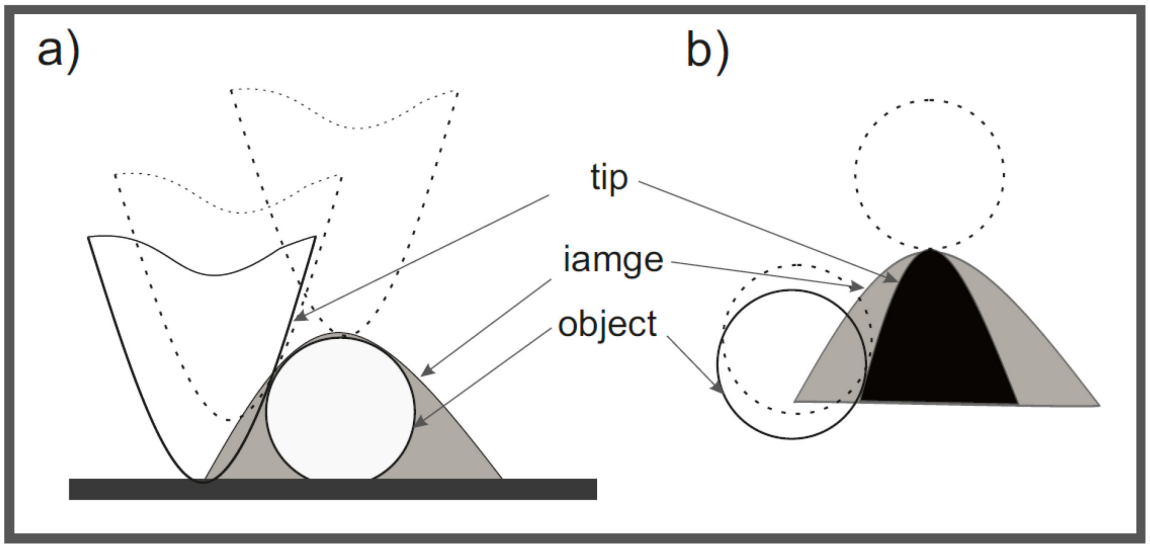

Figure 3-4. a) Tip broadening effect: an artifact (dark area) is induced due to the size of the tip, b) tip characterization: the tip image is obtained with the help of known sample geometry and the SFM original data.

The shape and the size of the tip can be reconstructed using, e.g., gold colloid spherical particles with known radius close to the size of the tip, i.e. a few nanometers. We denote the

sphere surface by S(X, Y), the tip surface by T(x, y) with a minimum point at the apex, where x=y=0 in the tip coordinate and (σ_1, σ_2) in the sample coordinate. Therefore the SFM image, denoted by I (σ_1, σ_2), is the trajectory of the minimum point of the tip during the tip in contact with the sample. Let the sphere sit at the origin of the coordinate (0, 0). We obtain

$$\sigma_1 + x = X;\ \sigma_1 + y = Y \qquad (3-4)$$

$$I(\sigma_1, \sigma_2) + T(x, y) = S(X, Y) \qquad (3-5)$$

At the contact point, we have

$$\frac{\partial T}{\partial x} = \frac{\partial S}{\partial X} = \frac{\partial I}{\partial \sigma_1} \qquad (3-6)$$

$$\frac{\partial T}{\partial y} = \frac{\partial S}{\partial Y} = \frac{\partial I}{\partial \sigma_2} \qquad (3-7)$$

At the boundary, where the minimum point of the tip reach the highest point of the sample, all variables equal zero. This boundary condition together with the equations above gives the exact solution of the tip size and shape T(x, y) (Fig. 3-4b). Knowing the shape of the tip, one may reconstruct the SFM image of other arbitrary sample surface.

A tip characterization example is given in Fig. 3-5 using spherical gold nano-particles with a size of 15 ± 1 nm. The geometry of the tip is characterized and a radius around 10 nm on the apex is obtained.

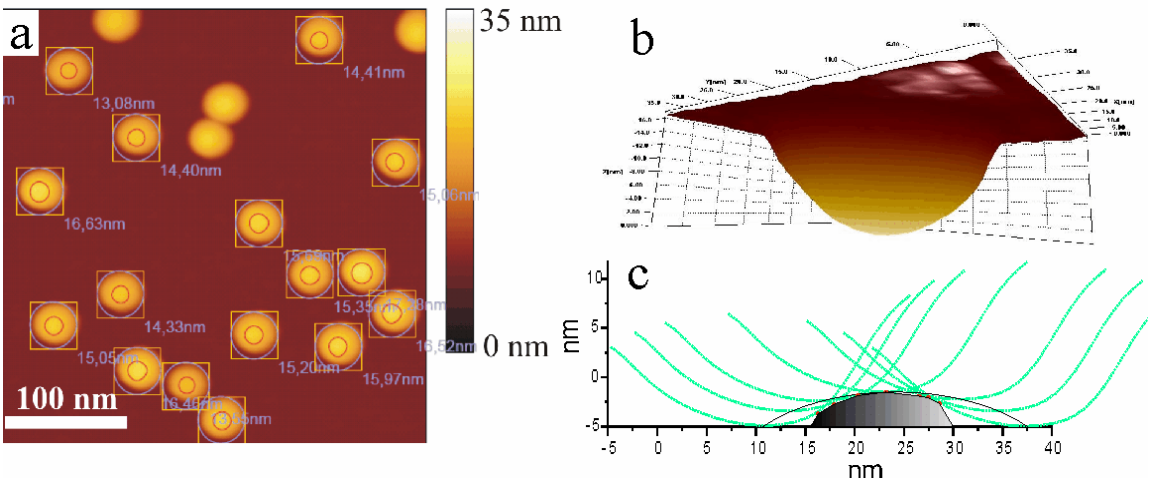

Figure 3-5. a) SFM height image of spherical gold nano-particles of 15 nm: the red circles

demonstrate the “true” spheres, b) the reconstructed tip geometry with a radius around 10 nm, c) tip broadening effect. (Wei Zhuang’s dissertation, Humboldt Universität zu Berlin, 2009)

3.2. Sample preparation

3.2.1 DNA on the graphite surface

Under ambient conditions a droplet of alkylamine solution in chloroform was deposited onto a freshly cleaved Highly Oriented Pyrolytic Graphite (HOPG) surface mounted on a spin coater rotating at 40 rps. A few seconds thereafter the spinning was switched off and the sample surface was optionally imaged by SFM in tapping mode. DNA molecules (pUC 19, 2686 base pairs; pUC 322, 4361 bp; pMEX5 (ss-DNA), 3631 bp; Mobitec GmbH, Göttingen) were deposited on the alkylamine pre-coated surface by applying a droplet of DNA aqueous solution (1 μg/ml) and thereafter by spinning it off after 5 seconds. The sample was then imaged with SFM) in tapping mode with a Nanoscope 3a (Digital Instruments Inc., Santa Barbara, Ca.), using silicon cantilevers (Olympus, Japan) with a typical resonant frequency of 300 kHz and a spring constant of about 42 N/m.

3.2.2 Polymer brushes and hyperbranched polyglycerol on the mica surface

The polymer was either dissolved in water or in chloroform. A droplet of the solution was deposited onto the freshly cleaved mica surface. The droplet was spun off after 5 seconds. The surface was dried under a nitrogen flux and then measured by SFM.

4. Result and Discussion

The properties and application of polymer materials relate strongly with their structures. In this section I characterize this relationship on a single molecule level. To do this, I investigated three systems: plasmid double stranded DNA, amphiphilic tri-block copolymers, and dendritic hyperbranched polymers. They formed quasi one-dimensional, two-dimensional and three-dimensional structures at a surface, which were then characterized mainly by SFM and other characterization methods. In the following I start with the investigation of DNA conformations and their mechanical properties (Section 4.1) and continue to study an amphiphilic tri-block copolymer (Section 4.2) and dendritic hyperbranched polyglycerol (Section 4.3) on different substrates.

4.1 Single DNA conformation and mechanical properties on a surface

4.1.1 Single DNA conformation on a nanostructured template

Besides its renowned role in biology, DNA has been recognized promising for molecular nanotechnology, e.g. for DNA-templated assembly of nano-objects,[17-19] DNA scaffolding and computation,[20, 21] and DNA-based nano-devices.[22-24] These applications benefit from DNA's unique structure properties, which relate strongly with the DNA conformation. For example, direct DNA sequencing by scanning probe techniques requires fully stretched single-stranded DNA (ss-DNA) on a surface.[25, 27] It is still a challenging task to control the molecule conformation in a predicted manner.

Molecular self-assembly on a surface introduces a "bottom up" approach to control and design desired nanostructures. Long-chain alkanes and their derivatives self-assemble into highly ordered lamellar structures on Highly Ordered Pyrolytic Graphite (HOPG),[115] which can be utilized to fully stretch polyelectrolyte molecules on the surface.[116, 117] An HOPG surface pre-coated with a molecular layer of an amphiphile such as an alkylamine or a fatty acid can be regarded as a molecular "workbench" for adsorption of polyelectrolytes and further

manipulation and fabrication of structures on the single molecule scale with a scanning probe tip.[28]

In the following I report a method to tune the surface properties by varying the surface coverage of pre-coating alkylamine, which allows to control the conformation of vector double-stranded DNA (ds-DNA) and ss-DNA on an alkylamine pre-coated HOPG. It will be shown that plasmid DNA exhibits supercoiled conformations at low surface coverage, slightly stretched circles with a split part of the double helix into two single strands, fully stretched and over-stretched conformations at sub-monolayer coverage, relaxed circles at monolayer coverage, and condensed coils above monolayer coverage. ds-DNA is stretched up to 1.25 times its original B-form length and ss-DNA is stretched to 0.44 nm/bp. The different conformations are attributed to the interplay of topological constrains of the plasmid DNA and its interaction with the amphiphiles and the substrate.

The nanostructured template

Fig. 4-1 shows HOPG coated by an octadecylamine solution of different concentrations. HOPG coated from a solution at a concentration lower than 30 mg/L reveals no significant features except the typically flat graphene planes with step edges. Straight domains of lamellae can be detected for concentrations above 30 mg/L, with their surface coverage increasing with the increase of the octadecylamine concentration (Fig. 4-1 b-c). The inserts in Figures 4-1b and 4-1c show the height histograms for both images. Nearly perfect monolayer coverage is observed for a concentration of 100 mg/L (Fig. 4-1d). The angle between the lamellae in different domains is 60°, as indicated by the arrows in Fig. 4-1d, reflecting the 3-fold symmetry of the underlying graphite substrate. Further increase of the concentration leads to the formation of islands on top of the monolayer (Fig. 4-1e).

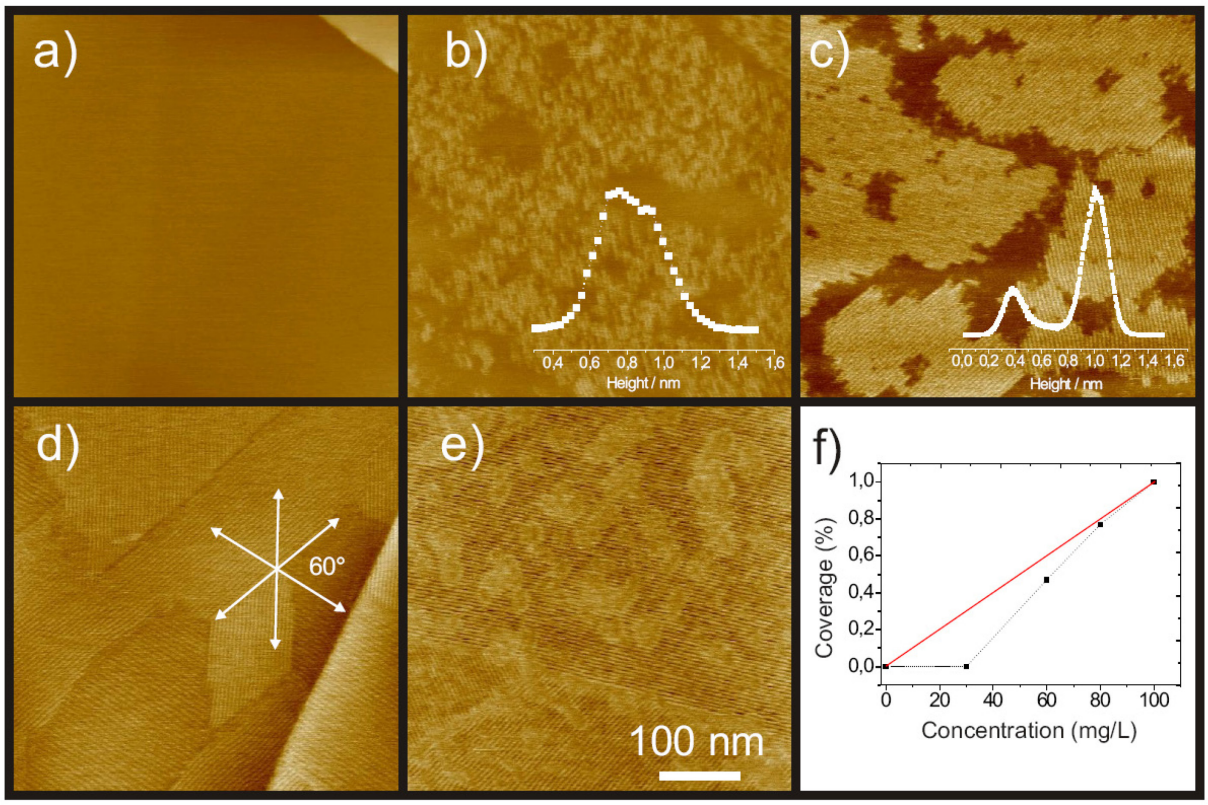

Figure 4-1. SFM height images of HOPG surfaces covered with octadecylamine spin coated from different concentrations: a) 10 ml/L, b) 60 mg/L, c) 80 ml/L, d) 100 mg/L, and e) 160 mg/L. The arrows in d) show the three domain orientations. Inserts in b) and c) demonstrate height histogram employed to estimate the surface lamellar coverage dependence on solution concentration shown in f) (squares). The straight line from zero to a hundred percent is added as a guide to the eye.

Absence of any visible structures for low concentrations of octadecylamine can be attributed to a homogeneous liquid monolayer phase, undetectable with SFM. Nucleation of solid domains at concentrations higher than 30 mg/L implies that a critical surface concentration of liquid phase must be achieved to promoted lamellae crystallization. The height histograms clearly show two peaks, which can be assigned to the liquid phase and the crystalline phase. The surface crystalline coverage is assigned to the ratio of the areas of the Gaussian fits of the peaks and plotted in Fig. 4-1f.

The total concentration of the amphiphile molecules on the surface C_t may be expected to grow linearly with their concentration in solution C_s,[118] i.e. $C_t=aC_s$. A linear dependence

of the crystalline domains surface coverage x on the concentration in solution (Fig. 4-1f) and C_t, correspondingly, implies that the concentrations of molecules in the crystalline, C_c, and the fluid, C_f, phase domains do not depend on C_t, i.e.:

$$C_c x + C_f(1 - x) = aC_s \qquad (4-1)$$

A fit of the experimental data (Fig. 4-1f) with Eq. (4-1) allows to estimate the C_c/C_f ratio to be about 3, which is substantially larger than 1. This furthermore supports the model of coexisting fluid and crystalline phases of molecules, with the excess of molecules in the fluid phase condensing into the crystalline phase.

Double-stranded DNA on the nanostructured template

Fig. 4-2 displays DNA on a HOPG surface covered with different amounts of octadecylamine. At low surface coverage (5% of monolayer coverage), DNA molecules on the surface exhibit supercoiled conformations. An increase of the octadecylamine surface coverage to 10% promotes the formation of slightly over-stretched open circle DNA conformations with a part of the double helix of 95 ± 10 nm long splitting into two single strands (Fig. 4-2b). Similar melting of ds-DNA on a dodecylamine pre-coated graphite surface has been previously observed, but the mechanism was not understood.[28] It has been argued that the melting occurs already in buffer solution.[7] In our case, however, we attribute the melting to the twist-stretch coupling of the plasmid DNA on the surface, which we will discuss in detail below.

DNA exhibits straight long segments on the surface covered with a mixture of crystalline and fluid octadecylamine domains (30% - 80% of monolayer coverage) (Fig. 4-2c). The straight segments are oriented along the lamellar axes of octadecylamine. An octadecylamine monolayer promotes DNA adsorption in relaxed conformations (Fig. 4-2d). Molecules form condensed coils on the surface covered with 130% octadecylamine monolayer (Fig. 4-2e). The contour lengths of a DNA backbone at different amphiphile surface coverage are measured and compared to the expected length in B-form (Fig. 4-2f). The DNA length

increases with an increase of the surface coverage up to 30% of monolayer coverage, where it saturates and remains constant at a value of 1.25 of B form length. The DNA length drops down to around 1.0 at monolayer coverage. The DNA backbone length cannot be measured above the monolayer coverage.

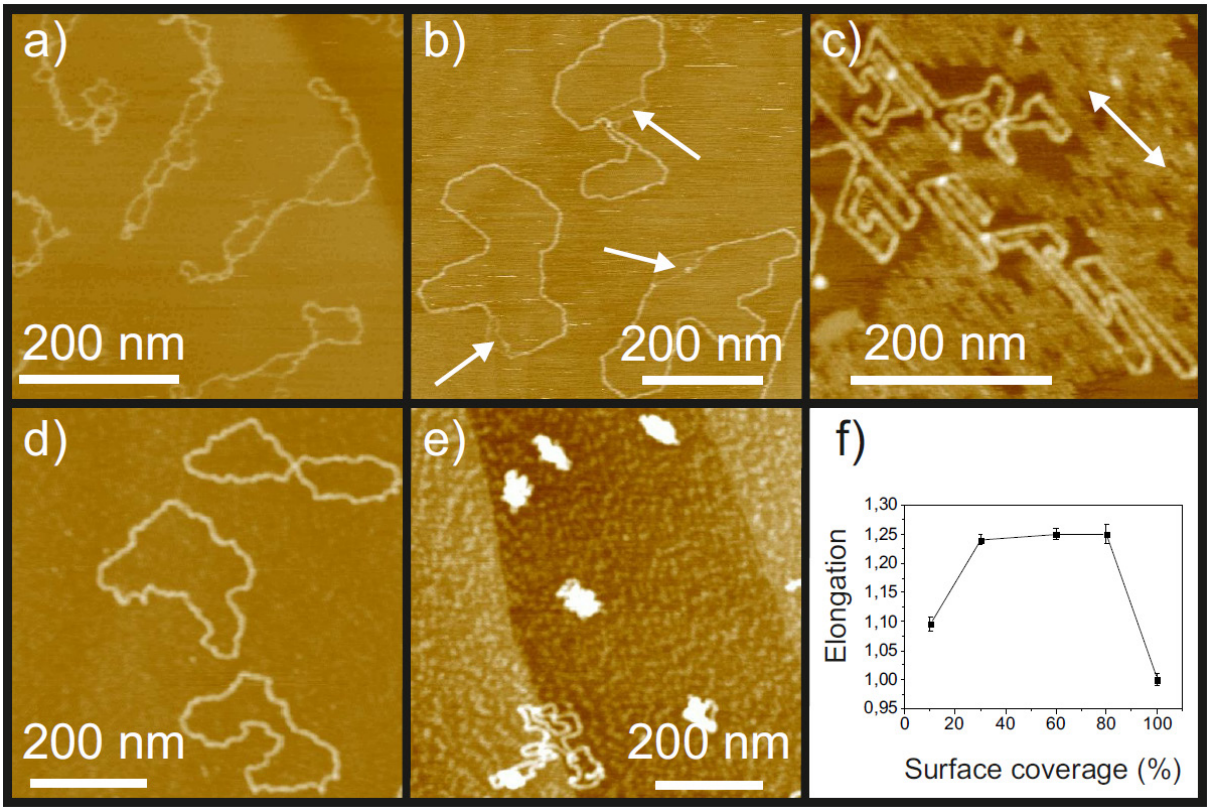

Figure 4-2. SFM height images of ds-DNA on HOPG surface coated with octadecylamine at different surface coverages: (a) 5%, (b) 10%, (c) 60%, (d) 100%, (e) 130% of a monolayer coverage. f) Elongation of ds-DNA contour lengths plotted versus surface coverage with octadecylamine in % of a monolayer.

We attribute variable conformations of plasmid DNA on the octadecylamine coated surface to the surface regulated release of the topologically caused strain, built up due to effectively different ionic strength at the surface and in solution, as well as the interaction with the surface. The topological state of a covalently closed circular DNA molecule can be described by the linking number *Lk*.[43] It is the sum of two components the twist number *Tw* and the writhe number *Wr* and remains constant as long as the two strands remain covalently

closed. However changes of environmental conditions such as pH and ionic strength vary the number of base pairs per double helix turn γ, and thus the number of helical turns, i.e. the twist number *Tw*, which is defined as the total number of base pairs *N* divided by γ: $Tw = N/\gamma$. In order to keep the *Lk* constant, the plasmid DNA double helix backbone requires to writhe and coil across itself to form supercoiled DNA, which is described by the changes of writhe number *Wr*. During DNA application from aqueous solution onto the surface, the positively charged protonated amine head groups of the amphiphile molecules bind to the negatively charged DNA backbone, screening the repulsive electrostatic forces along the backbone, changing the optimal number of base pair per helical turn, thus *Tw*, and thereby also *Wr*, i.e. changing the supercoiling extent and building up stress in the chain.

Plasmid DNA can release the stress by super-coiling in solution, thanks to free rotation in space. Similarly, plasmid DNA formed condensed coils on an above monolayer coverage surface, since the DNA amphiphile complexes could rotate freely due to the relative weak interactions with the surface. On monolayer coverage surfaces, however, DNA was anchored by the amphiphile molecules onto the surface, which must hamper DNA mobility. A perfect monolayer of octadecylamine freezes the DNA molecules upon their adsorption, such that the DNA conformation on the surface can be regarded in first approximation as the 2D projection of the conformation in the solution. Reduction of the surface octadecylamine concentration must reduce also the number of the molecules anchoring the DNA backbone, such that at very low octadecylamine surface coverage (~below 5%) the DNA backbone can detach from the surface to release the stress by supercoiling (Fig. 4-2a). However an increase of the surface coverage to 10% prohibits the detaching. In this case the topological stress is reduced by partly unwinding of the double helix into two single strands (Fig. 4-2b). It has been argued that plasmid DNA splits partly in solution under physiological conditions.[7] However, in our case, the dependence of DNA splitting on the surface coverage with octadecylamine implies that DNA splitting occurs at the surface instead of in solution. We attribute over-stretching of DNA

molecules on sub-monolayer coverage to the steric repulsion of the octadecylamine molecules attached to the DNA [119] and the mobility of the amphiphile layer. Furthermore, we found the utilized surface coverage to be optimal for ds-DNA overstretching and to stretch ss-DNA as we will demonstrate in the following and then discuss the self-stretching mechanism.

Single-stranded DNA on the nanostructured template

Fig. 4-3a displays ss-DNA on HOPG with 30% ordered octadecylamine coverage. Similarly to ds-DNA, the ss-DNA backbone is stretched segment-wise. The angles between two adjacent segments along the backbone is measured and plotted in Fig. 4-3c. Two most frequently angles around 60° and 120° are observed. The angle between two lamellar domains is 60° (Figure 4-1d). This implies that the DNA segments are stretched along the lamellar axis. The average contour length of the molecules is 1588 ± 35 nm, which corresponds to 0.44 nm/bp. This value is 30% larger than 0.33 nm/bp measured on a dodecylamine pre-coated surface (Fig. 4-3b), where no lamellae are formed.

Both ss- and ds-DNA self-stretching on the surface can be explained as following: The DNA on the HOPG surface coated with a fluid phase prompts condensation of amphiphiles onto the DNA backbone. The large adsorption energy of the alkyl chains forces them onto the HOPG surface thereby sterically stretching DNA backbone.[119] The maximal stretching is then defined by the distance between two adjacent octadecylamine molecules in the lamellae, which is indicated by *L* in Fig. 3c. *L* is known to be 0.45 nm from high resolution STM images.[120] This value is very close to the observed 0.44 ± 0.01 nm per base for ss-DNA, which allows us to suggest the model that each charge along the DNA backbone is bound to one octadecylamine molecule and that the octadecylamine molecules adsorb on one side of the stretched segment. However this is not necessarily true for ds-DNA due to its 3D helical structure.

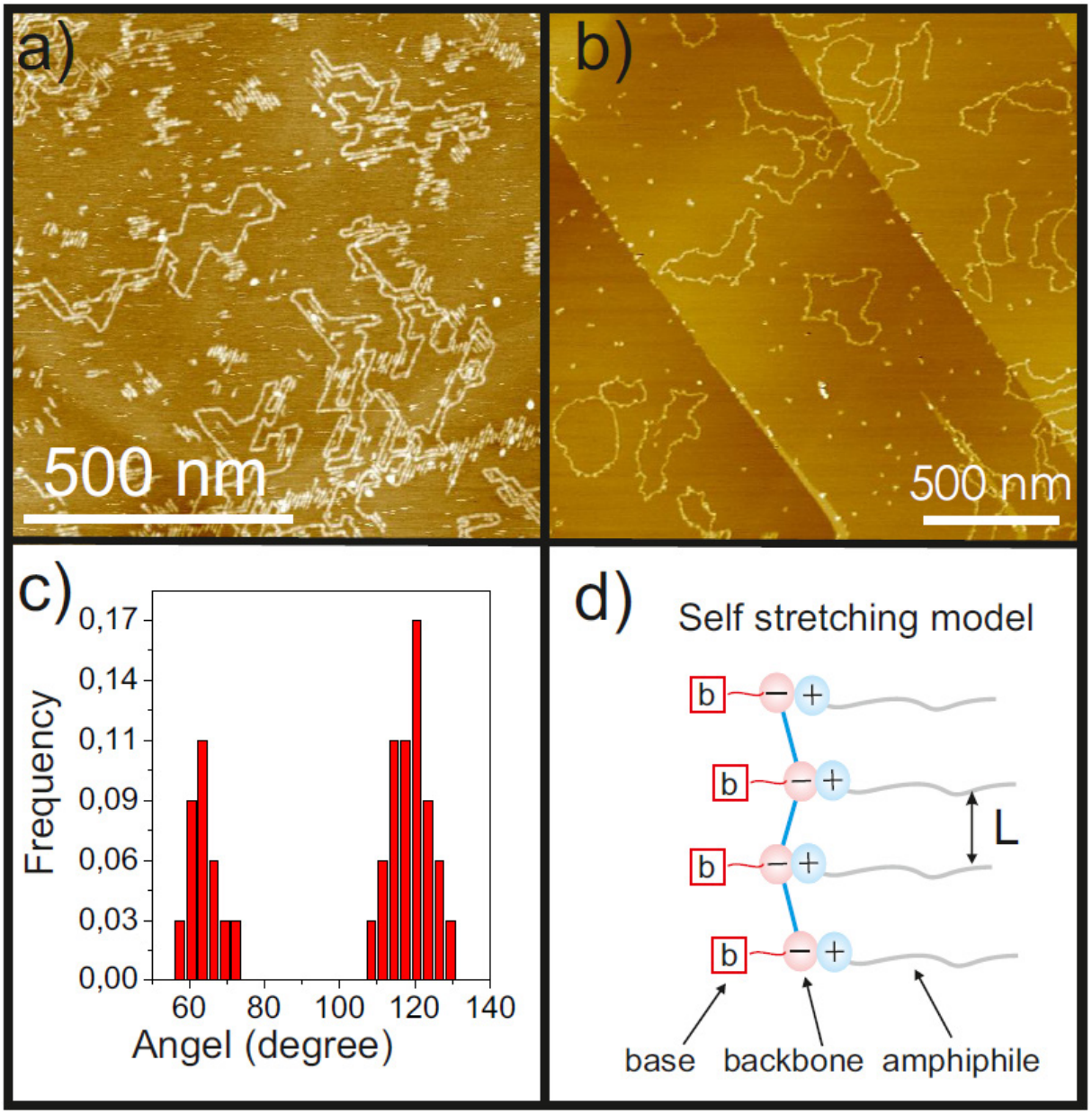

Figure 4-3. a) SFM height image of ss-DNA on HOPG pre-coated with 30% of a monolayer of octadecylamine. The large number of short segments is attributed to short pieces of ss-DNA molecules, resulting from fragmentation of ss-DNA molecules in solution; b) ss-DNA on HOPG pre-coated with 30% of a monolayer of dodecylamine; c) Angles between two adjacent segments along the backbone of ss-DNA in a); d) Proposed self-stretching model.

Stretching related splitting of double strand

The partial splitting of ds-DNA when adsorbed onto the surface is in particular interesting because unwinding and splitting of the DNA double helical structure at a specific region is the initiation step for DNA replication (Kornberg A., Baker T., DNA Replication, Freeman, New York, ed. 2, 1992). In bacteria, e.g. in *Escherichia coli*, replication initiation has been reported to involve the initiator protein DnaA binding to DnaA boxes at the *oriC*,[36] forming a big nucleoprotein complex which facilitates the melting of a nearby A-T rich region named DNA-unwinding Element (DUE).[37, 38] However the original mechanism of strain translocation from oriC to DUE remains ambiguous[121] and should be based on the specificity of DNA mechanics. Therefore studies on single DNA mechanics should help to understand DNA melting.

Recent experiments and theoretical studies on pulling and rotating single double-stranded (ds-) DNA reveal its charity in mechanical twist-stretch coupling: small stretchings along the DNA backbone induced tortional stress along the molecule backbone and vice versa.[5, 6, 122] It has been theoretically shown that ds-DNA may release its torsional stress inhomogeneously along the backbone with localized, sequence-dependent structural failure to preserve the B-form, when supercoiling is not allowed.[123] Therefore, stretching may cause double helix splitting. However, the pulling experiments were carried out in solution, where it is difficult or impossible to access the direct conformational changes during stretching. Self-stretching of DNA upon adsorption on the surface allows us to look into this issue.

Fig. 4-4a shows pUC 19 DNA molecules self-stretched on a graphite surface, pre-coated with octadecylamine ($C_{18}H_{37}NH_2$). The DNA presents a slightly stretched backbone with one part splitting into two single strands. The length of un-split double-stranded part is 954 ± 30 nm while each single strand in the split part is 98 ± 10 nm. Fig 4-4b shows a mixture of pBR 322 and pUC 19 molecules adsorbed on the surface. Note that there is only one splitting part for

each molecule. The splitting length in pBR 322 is about 1.6 times as long as that in pUC 19. The exact ratio is obtained by comparing the molecule's contour lengths.

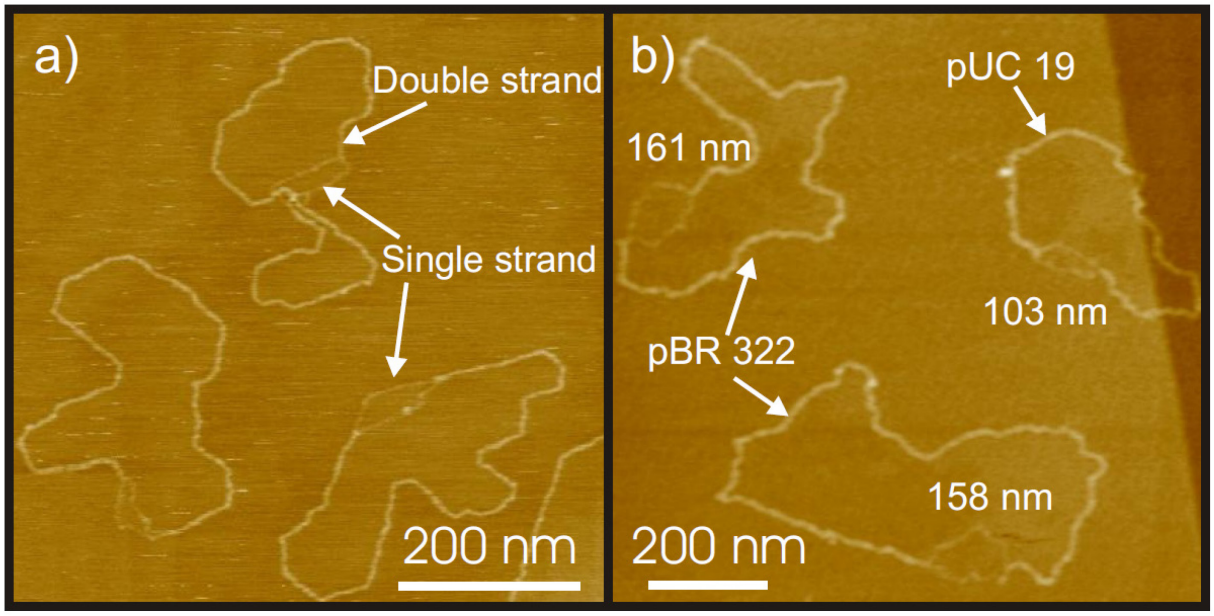

Figure 4-4. SFM height images of a) pUC 19 (2686 bp) overwinding and splitting when stretched on a surface, with a splitting length of 98 ± 10 nm; b) mixture of pUC and pBR (4361 bp), with splitting lengths of 103 nm, 158 nm, and 161 nm, respectively. (Wei Zhuang's dissertation, Humboldt Universität zu Berlin, 2009)

The contour length of the un-split part (945 nm) is slightly longer than the B-form length (913 nm) of pUC 19, which reveals that the DNA backbone is overstretched on the surface. The stretching is attributed to the repulsive interaction between the adjacent amphiphile molecules which attach to the DNA backbone through Coulomb interaction.[119] In the splitting part, assuming 0.44 nm per base for ss-DNA we obtain that 216 base pairs were melt, which is corresponding to 22 helical turns in B-form. For an un-nicked plasmid DNA, its linking number is constant. Therefore, the changes of twist number in the split part must be compensated in the other part of the molecule, forming partially overwinding DNA. Therefore we observe an overwinding plasmid DNA double helix with localized splitting, when it is slightly stretched

on surface. In the following, I continue the discussion on the mechanism of overwinding and splitting.

In solution, DNA only overwinds in a certain stretching force range (0 ~ 30 pN) to keep the base pair stacking.[5] Similar results are found in here: DNA overwinds and splits only in a certain chain extension window. DNA adsorbed on the surface without chain extension and with a chain extension 20% longer than its B-form length presents a homogenous backbone without overwinding and splitting (Fig. 4-2). Furthermore, a structural transition, similar to the ds-DNA B- to S-form transition, is detected when plasmid DNA is stretched to more than 1.7 times its B-form length on the surface, which suggests that the DNA helical structure is conserved on the surface (details in DNA mechanics section above). Therefore, we attribute DNA overwinding on the surface to surface stretching. To test this statement, we performed experiments under the same conditions with pBR 322, which is 1.62 times longer than pUC19. Under the same extension both DNA molecules should exhibit the same overwinding per unit length. This predicts that the split length of pBR 322 should be 1.62 times longer that of pUC 19, i.e. 159 nm. This prediction agrees well with the experimental data (Fig. 4-4b). However, in our case a 10% stretching of DNA leads to around 5% increase in the twist number, which is about four times larger than that obtained from experiments in solution, which extrapolates to a ~1% increase in twist number.[5] The difference may reflect an effect of the surface.

Stretching induces torsional stress along the DNA backbone. In the absence of supercoiling, the torsional stress may either be distributed homogenously throughout the whole backbone or released by localized structural failure.[123] Single DNA molecule studies show that DNA's mechanical properties are inhomogeneous and sequence dependent.[44] The reason may be that there are two hydrogen bonds in an Adenine-Thymine (A-T) pair and three hydrogen bonds in a Guanine-Cytosine (G-C) pair, which leads to different bonding energies and different separation forces of the base pairs.[124] Fig. 4-5 shows the average A-T pair percentage in every 100 base pairs along the DNA sequence for pUC 19 and pBR 322. Two

maximum peaks are observed in both plasmid DNAs. The value reaches as much as 76% in the maximum peak and lowers to 27% in the minimum peak. Under the same torsional stress, the A-T rich region thus has a higher possibility to unzip. In this case, I attribute the splitting of the double helix to release the torsional stress to where DNA supercoiling is prohibited. The splitting position is most probably in the A-T rich domains.

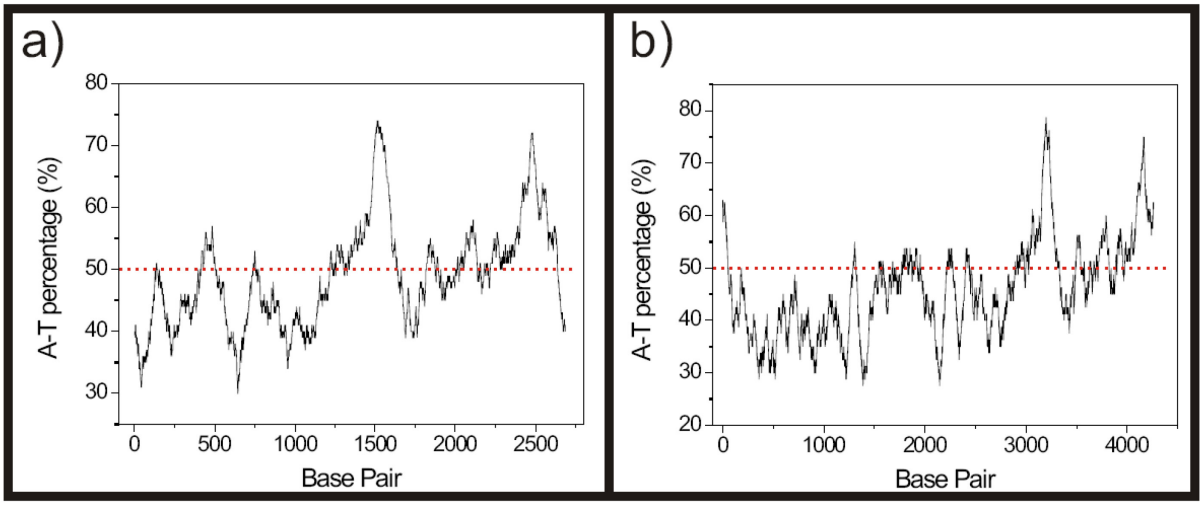

Figure 4-5. A-T base pair percentage in every 100 base pair along the sequence: a) pUC 19 and b) pBR 322

A special feature observed in our experiments is that there is only one split part in one molecule and the splitting length is proportional to the total length of the molecule. Only one split part can be understood by the cooperative effect of breaking the base pairs stacking [125]: once one base pair breaks, its adjacent base pairs loses a portion of π-π stacking and becomes less stable. Therefore it is more energetically favourable to break further from the already existing failure point. Only one splitting part in each molecule also suggests that the torsion-splitting effect is a long range effect, which correlates the whole micrometers long chain. This suggestion is strengthened by the fact that the splitting length is proportional to the length of the chain.

The results may help to understand biological processes which require splitting of a double helix such as DNA during replication and transcription. The results also imply a general

melting mechanism analogue to DNA replication initiation *in vivo*: the formation of a nucleoprotein complex may induce torsional stress, which propagates to a nearby A-T rich region and releases thereby the splitting. Further experiments on DNA with protein markers are required to define the splitting position.

4.1.2 DNA tensile strength

Double-stranded DNA can be stretched to 125% percent of its native B-form length by self-stretching on the nanostructured surface. Further extension up to 210% was obtained by single molecule manipulation methods such as pulling with SFM tips,[12, 14] micropipettes,[1] an optical trap,[2] and dragging with a receding meniscus.[11] In such experiments, the bond rupture strengths was acquired with typical dynamic force loads, i.e. the force was increased with time until the bond broke, with the bond strengths under dynamic load depending on the force loading rate.[13, 14, 126] Under a static load, i.e. when a bond is stretched with a constant force, different bond strengths and rupture mechanisms are predicted by theory.[16, 127] The specific experimental setups mentioned above limit the time under which a constant load can be maintained, and hence restrict the possibility to investigate relatively long-living bonds. To the best of my knowledge the longest reported time for constant force holding in a force-clamp SFM has been about 30 seconds.[128] In nature, however, many processes which involve breakage of a single covalent bond occur on a time scale of hours or even longer, e.g. polypeptide chains strained by proteins degrade *in vivo* from minutes up to days.[129] Also engineering materials are typically under stress on times exceeding seconds substantially. Direct conformational information on the target molecule is usually not accessible in such pulling experiments. In the following I demonstrate the employment of a recently developed method, “blowing manipulation”,[49] which allows to expose plasmid ds-DNA molecules on a surface to a constant strain for a time on the order of an hour to study the time-dependent

mechanical properties of single DNA. Stretching of the DNA molecules was achieved through a SFM tip interacting with an ultrathin film of an organic liquid coating the surface.

Blowing manipulation

Plasmid DNA was deposited on the alkylamine pre-coated HOPG surface by the method described above. Thereafter a droplet of organic solvent such as chloroform was spin-coated onto the surface to form a thin liquid layer. DNA molecules remain in the relaxed conformations after their deposition on the surface in the absence of scanning. The loops start to increase their size and eventually "blow" to almost perfect circles and eventually even broke during their imaging in tapping mode SFM. This has been attributed to the interaction of the SFM tip with the thin liquid layer, which remains on the surface for a certain period of time after spin coating of the organic solvent. This time has been named as the "active time", which depends on the affinity of the liquid to the graphite surface.

Fig. 4-6 presents SFM height images of one DNA molecule, which formed two loops by self-crossing on the surface. The loops increased their sizes and grew into round circles during the first few scans, and then stabilized in size. The smaller loop increased 20% in length while the bigger one increased by 85%. The bigger loop broke one hour after its size stabilization while the smaller one remained unaffected.

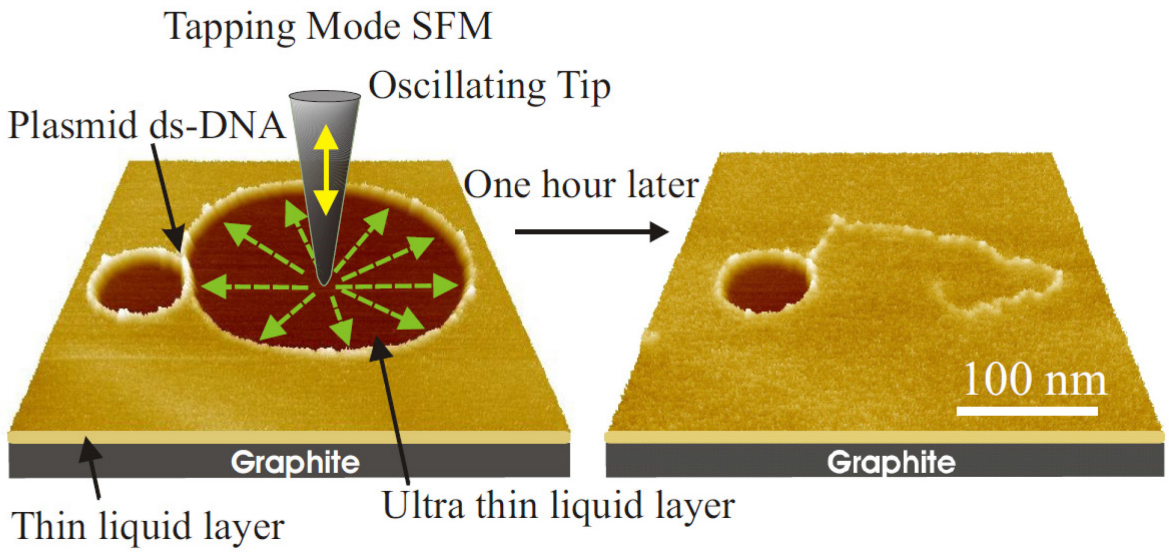

Figure 4-6. Blowing manipulation: a thin liquid layer was formed on the surface by spin coating a droplet of organic solvent onto the HOPG surface; an ultra-thin liquid layer around 1 nm was formed inside the loop while the SFM tip was scanning the molecule, which created a surface pressure difference between inside and outside of the loop. This pressure "blew" the DNA loop isotropically along the surface to perfect circles and broke the loop. Loops formed by the same DNA molecule grows independently, the rupture of one loop does not affect the other. [49]

Different elongation of the loops implied different tangential force along the two loops. The tangential force along the DNA backbone is defined by the surface pressure difference and the length of the loop as follows:

$$f_t = \Delta\sigma \times l/2\pi \qquad (4-2)$$

where $\Delta\sigma$ is the surface pressure difference, and l is the contour length of the loop.

For the loops in the same scanning area within the "active time" of the liquid layer, the surface pressure difference stays constant. Therefore the tangential force is a linear function of the contour length of the loop. This fits well with the experimental observations: in the same scanning area large loops grow faster than the small ones and break first. Thus the "blowing manipulation" method extends the time of applying a constant force to a single molecule from seconds in a conventional single molecule vertical pulling experiment to hours. The tangential force is defined by the interaction between the tip and the thin liquid layer as well as between the liquid layer and the surface. Therefore it depends on the type of the tip used, the scanning

parameter such as the scanning area, and the liquid type. By optimizing these conditions carefully, one can obtain enough data to study statistically the time dependent mechanical properties of the DNA.

Statistics of time dependent rupture of single DNA

Large scanning areas in the blowing manipulation experiments are chosen to include more molecules for better statistics.

Fig. 4-7 shows SFM images of pUC19 plasmid DNA, on the same area (3 μm × 3 μm), at different times. The first image displays almost unstrained single DNA molecules on the surface. As imaging continues, the irregularly shaped loops grew into circles with the larger loops growing faster than the smaller ones. The loops continued to grow until the force stretching the molecules became either balanced by the restoring force of the DNA backbone, or the force became large enough to break the largest loops, such as for the molecules indicated by the arrows 1 and 2. We will refer in the following to such breakage as "dynamic". The smaller loops that did not break stabilized their size after 15 minutes of scanning (Fig. 4-7c). Breakages of these loops could be still observed up to 20 minutes after the size stabilization such as the molecule indicated by arrow 3. We will refer in the following to such breakage as "static". Dynamic breakage occurred mostly when the tip was scanning over the molecules; examples are indicated by the arrows 1 and 2 on Fig. 4-7b. This can be attributed to the growth of the force during SFM tip scanning inside the DNA loops. These loops increased their sizes up to 2.1 times of their original *B*-form lengths until they broke. Broken molecules relaxed into less stretched conformations with the length 30% longer than that expected for *B*-form DNA. On the contrary, static breakage happened typically after size stabilization of the loop and mostly when the tip was tapping outside the loop; an example is indicated by the arrow 3 on Fig. 4-7c and Fig. 4-7d. This can be attributed to a constant force maintained inside the loop, also when the tip was scanning outside of the loop. In some cases the molecules formed a few

topological loops on the surface. In case if one of such loop broke, connected loops remained visually unaffected, as such indicated by the arrow 4 on figure 4-7d. Therefore we included such topological loops into the statistics.

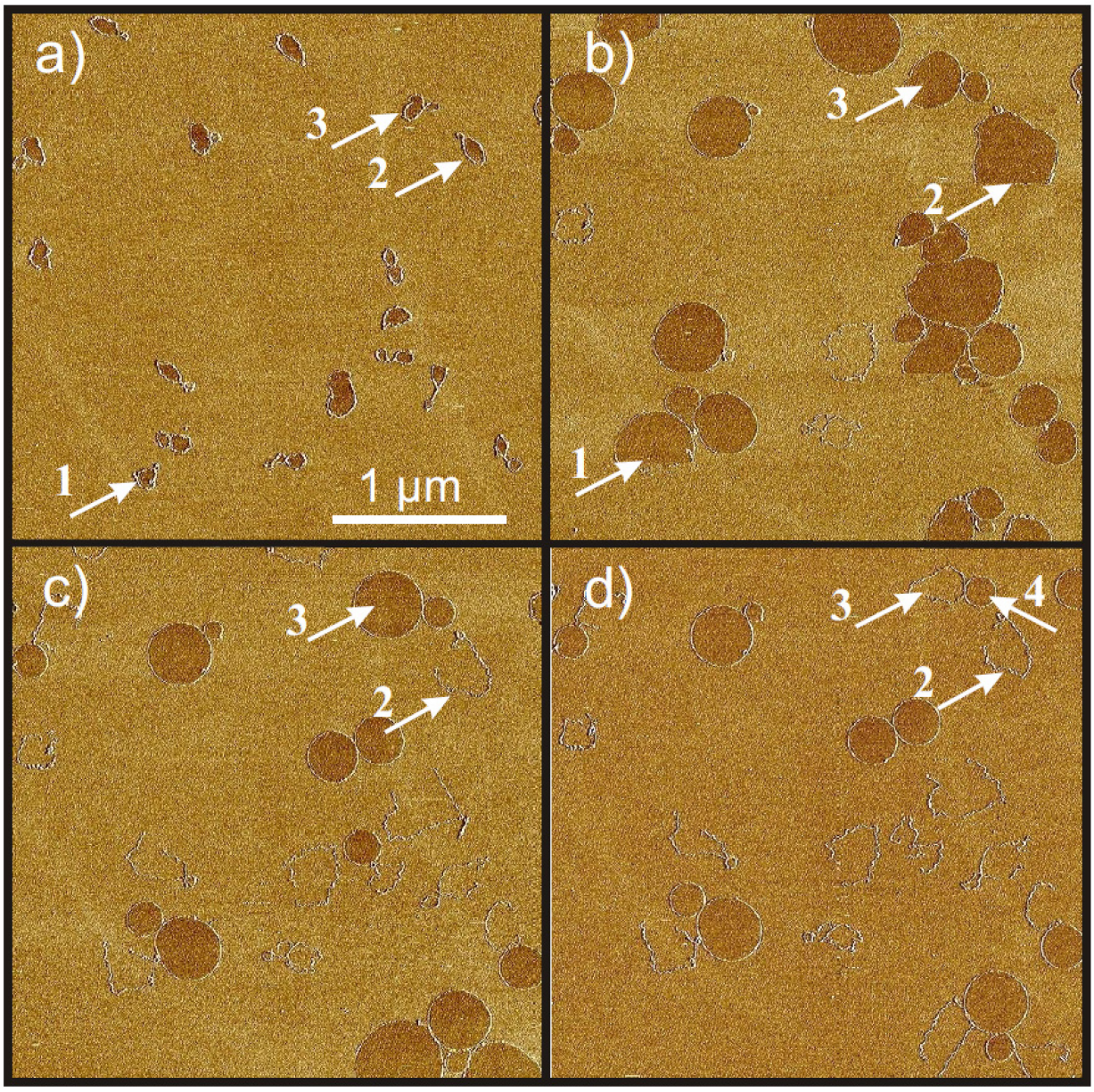

Figure 4-7. A few selected SFM phase images from a sequence of images of ds-DNA on HOPG precoated with dodecylamine in chloroform taken at the same scanning area as a function of time: a) 3 minutes, b) 9 minutes, c) 15 minutes and d) 35 minutes after the experiment started. Arrows 1, 2 and 3 mark three loops, which break as one goes from b) through d). Loop 1 and 2 breaks during growth in size which present the breakage in a dynamic force load; Loop 3 breaks after its size stabilization which introduces the breakage under a constant force. The images were scanned from top to bottom. Phase contrast between inside and outside of the DNA loops

implies different SFM tip-surface interactions indicating different surface pressures inside and outside of the loops, giving rise to tangential forces stretching the molecules.

The experiment was repeated seven times and the size of each loops was traced and recorded at different time after the experiment started. We analyzed the loop size growth and breakages with the cumulative distribution functions of the loop sizes in order to avoid binning of the data. The results from different experiments were accumulated in one graph (Fig. 4-8).

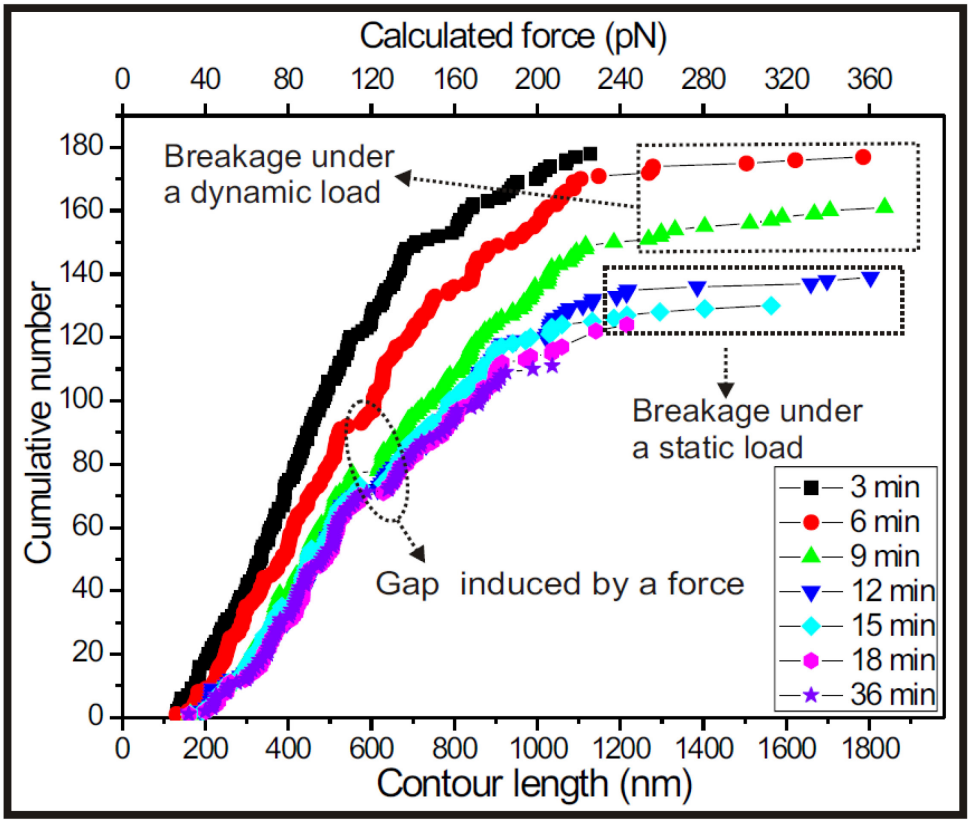

Figure 4-8. Time development of the cumulative distribution function of loop sizes of pUC19 ds-DNA. The data were taken from seven independent experiments. The dynamic load regime, characterized by loops increasing in size, is followed by a static regime. [130]

180 DNA loops with size varying from 150 nm to 1100 nm in seven independent experiments have been identified on the images taken within the first 3 minutes of the blowing experiment. The length of the longest non-supercoiled DNA was 1100 nanometers, slightly longer than the expected *B*-form length of 913 nm. Loops with size smaller than 913 nm were formed by supercoiled DNA molecules. During the next 12 minutes the 40 largest loops broke,

while still increasing their sizes, i.e. in a dynamics load regime. The rest of the loops stabilized in their size. Breakage events of size stabilized loops still could be observed up to 24 minutes thereafter (Fig. 4-8). Listed in Table 4-1 are the average survival times in the static load regime for loops, which broke at around 1780 nm and loops breaking at lengths from 1000 and 1075 nm. In order to exclude the uncertainty of coiled loops, we chose a shorter plasmid DNA sample with 1650 bp. (sk13.3). The surviving time of sk13.3 in the static load regime for non-coiled loops is also listed in Table 4-1.

Table 4-1. List of average time period *t* for breaking DNA loops of lengths *l* (error bars are the standard deviations) and number of base pairs n_{bp}

Plasmid DNA	Length at breakage (nm)	n_{bp}	***t*(s)**
pUC 19	1787 ± 78	2686	337 ± 230
Sk13.3	1102 ± 69	1650	762 ± 320
pUC 19 (coiled)	1000 to 1075	1563	876 ± 144

13, 9 and 6 single breakage events were analysed for pUC19, Sk13.3 and pUC19 (coiled) respectively. "coiled" stands for the DNA loops formed topologically, i.e. by self-crossing of DNA.

The tangential force has been previously attributed to the surface pressure developed by the SFM tip within the area enclosed by the loops. Thereby the force was argued to grow linearly with the length of the loop. The phase contrast in tapping mode reflects the difference between surfaces covered with different liquid films. Therefore, a homogeneous phase contrast between inside and outside of the loops (Fig. 4-7) on the images complies with the proposed surface pressure difference. Furthermore, the results imply that the force grows indeed with the length of the loops, since large loops break faster. We cannot, however, verify directly that the force grows linearly with the length of the molecules, and we will have to assume it in the following.

Theoretical Basis

In the following we will adopt the existing theories of polymer chain breakage under static load to our case. Let $U(x)$ be the (free) energy of a bond as a function of a reaction

coordinate x with a minimum located at x_-, corresponding to the equilibrium bond length and a barrier at x_+, separating the bound from the unbound state. For a single covalent bond under a load f the combined energy surface is given by $U_f(x) = U(x) - fx$. For small forces the location of the transition state $\Delta x = x_+ - x_-$ is only slightly perturbed and the activation rate $k(f)$ can be well described by the phenomenological Bell form[131]:

$$k(f) = k_0 \exp\left(\frac{f\Delta x}{k_B T}\right) \qquad (4-3)$$

to which several different approximations for bond failure processes are deduced in the quasistatic regime.[132, 133] In our case this approximation is applicable since the molecules are kept under constant tension over long time intervals. The thermal activation rate of an unloaded bond k_0 increases exponentially upon application of a static force f. In Eq. (4-3) k_BT is the thermal energy with temperature T and k_B being the Boltzmann constant. Note, that the mean time for breaking DNA loops and their corresponding standard deviations given in Table 4-1 are of the same order of magnitude, which justifies our assumption of having a single-exponent process underlying bond breakdown.

In our experiment, the two strands of the double helix of the ds-DNA are loaded in parallel and therefore the force acting on a single strand is half of the applied force f. We assume that as soon as one strand breaks, the second one fails immediately under double the force load. Then, the thermal activation rate k of the whole loop is proportional to the number of weak bonds in the two strands of the double helix, which is proportional to the number of base pairs n_{bp} and to the number of weak links per base pair n_w i.e.,

$$k \propto 2 n_{bp} n_w \qquad (4-4)$$

yielding

$$k(f) = 2 n_{bp} n_w \; k_0 \exp\left(\frac{f\Delta x}{k_B T}\right) \qquad (4-5)$$

Considering two DNA molecules with different numbers of base pairs $n_{bp}^{1,2}$ the ratio of the activation rates is given by

$$\frac{k_1(f_1)}{k_2(f_2)} = \frac{t_2}{t_1} = \frac{n_{bp}^1}{n_{bp}^2} \exp\left(\frac{\Delta x}{2k_B T}\Delta f_{12}\right) \qquad (4-6)$$

with $\Delta f_{12} = f_1 - f_2$. Combining Eq. (4-5) and (4-6) allows for the estimation of Δx and k_0, given the knowledge of the forces acting on the DNA molecules. Although we will the force calibration discuss in the following, we will first estimate k_0 without the explicit knowledge of the forces:

$$k_0 = \frac{k_1(l_1)}{2n_{bp}^1 n_w}\left(\frac{k_1(l_1)n_{bp}^2}{k_2(l_2)n_{bp}^1}\right)^{-l_1/\Delta l_{12}} \qquad (4-7)$$

Eq. (4-7) does not require explicit knowledge of the forces acting on the molecules; rather it relies on the assumption of a linear relation between forces acting on the molecules and their lengths. Assuming that there is one weakest link in every phosphodiester group, we can set $n_w = 1$ in the following. Since Eq. (4-7) depends only linearly on n_w, variation of n_w in a reasonably range does not change the result dramatically. Substitution of the experimental data from Table 4-1 into Eq. (4-7) gives an intrinsic activation rate of

$$k_0 = (2.2 \pm 0.1) \times 10^{-7} s^{-1} \qquad (4-8)$$

We will attempt in the following to explicitly calibrate the forces acting on the DNA molecules. Inspection of the cumulative length distribution curves reveals the formation of a gap around 550 nm after the first 6 minutes, which is absent at the beginning and persisting until the end of the experiment. Comparison of the loop sizes at the end of the experiment with their original size in the beginning of the experiment reveals that all loops above the gap have a stretching ratio larger than 1.5, while the loops below the gap have a stretching ratio smaller than 1.3. The gap implies a strongly non-linear dependence of the DNA restoring force on its length, e.g. a structural transition. The gap position remains in the same size region in the curves

after 6 minutes in Fig. 4-8, which indicates that the transition does not depend on the force loading rate in these experiments.

ds-DNA is an extensible molecule, with stretching behavior in solution that has been amply studied with the aid of single molecule manipulation methods. The force-extension curves recorded in such experiments reveal a highly cooperative structural transition from *B*-form to a stress induced *S*-form of DNA. The transition occurs at around 110 pN for un-nicked ds-DNA and is independent of force loading rates in the typical experimentally accessible range.[1-3] The ds-DNA structural transition takes place in solution at a broad range of different pH values and ionic strengths.[134, 135] The length of the ds-DNA increases from around 1.2 to 1.7 times its native *B*-form during the transition.

It is tempting to attribute the gap in the length distribution we observe on the surface to a structural transition similar to that in solution. Although the interaction with the surface (e.g. mica) may influence the DNA structure,[136] we assume in the following that the transition we observe on the surface happens under the same load as in solution, i.e. 110 pN for un-nicked DNA, thus obtaining an internal force calibration. Consequently, the force acting on each loop was calculated from the plot in Fig. 4-8, using a linear dependence of force on the length of the molecules: $f_1=f_2(l_1/l_2)$ with l being lengths of the molecules and F forces acting on them. Solving Eq. (3.3) for Δx and inserting the values given in Table 4-1 (together with the estimated values of the forces) one obtains for both combinations of measured data (pUC19/SK13.3 and pUC19/pUC19 (1 crossing)) Δx = 0.020 nm. This value agrees well with the one derived for a siloxane bond (Δx = 0.021 nm).[137]

Knowledge of Δx together with the previously estimated force values allows us to estimate an intrinsic activation rate k_0 with the help of Eq. (4-5):

$$k_0 = (2.2 \pm 0.1) \times 10^{-7} s^{-1} \qquad (4-9)$$

which is in a good agreement with the estimation without force calibration. This supports the assumption that the gap in the length distribution is indeed due to the DNA

structural transition. A rather unexpected result that DNA molecules on the surface tend to keep the B-form, i.e. base pair stacking, is supported by the observation of length relaxation of broken molecules (Fig. 4-7).

The results can be extrapolated to other force application dynamics and thus compared to those of other groups. Stretching experiments utilizing a receding meniscus breaks λ-DNA (48.502 bp) with a force of 476 pN in about 20 seconds.[11, 138] Here, 15 seconds were obtained from Eq. (4-5) with the same force and number of base pairs. When extrapolating to zero force one finds an apparent intrinsic activation barrier height of 45 k_BT, assuming the Arrhenius pre-factor of the order of 10^{13} s^{-1} as in vacuum. Note that this result is obtained from the knowledge of k_0, which did not require any questionable force calibration, and that this value is the upper limit of the barrier height, since the Arrhenius pre-factor is smaller under the experimental conditions. This value is still much smaller than the average bond energy of a single C-C (~140 k_BT), C-O (~145 k_BT), and P-O (~135 k_BT) bond, which are included in the DNA sugar-phosphate backbone. At first glance this result differs from our knowledge that the ds-DNA backbone is quite stable without external forces. However similar results were reported, e.g. an unexpected small energy barrier ~ 30 pN nm or 7.4 k_BT for single Si-O bond (average bond energy ~182 k_BT) was obtained in stretching experiments with an SFM tip.[137] It has been argued that external forces cannot only lower the energy barrier to enhance the thermal activation of bond breakage but also may act as a catalyst to increase the reaction rates.[139, 140] These features may increase the dissociation rate dramatically. An example is the exponentially increased dissociation rate of a disulfide bond upon the application of an external force.[141] The phosphate groups in the DNA backbone can undergo a hydrolysis process and the reaction rate increases significantly in the presence of a catalyst, e.g. from a rate constant of $\approx 2 \times 10^{-13}$ s^{-1} for uncatalyzed hydrolysis to a value of 6×10^{-7} s^{-1} for alkaline catalyzed hydrolysis, which is on the same order with our result.[142] We attribute the high dissociation rate ($\approx 2 \times 10^{-7}$ s^{-1}), low activation energy as well as low rupture forces for DNA

obtained in the present work to force-catalyzed chemical processes such as DNA hydrolysis. It is tricky to determine directly from the experimental data which chemical bonds are ruptured in the DNA backbone. It has been reported that in vacuum DNA is fractured by low energy electrons (3 to 20 eV) with a major cleavage of C-O bonds at the 3′ or 5′ position through a resonance process, namely dissociative electron attachment, which leads to the formation of stable anions and radical fragments.[143, 144] The hydrolysis of phosphodiester groups in neutral solution occurs at least to 99% by C-O cleavage.[145] We speculate that in our case C-O bond may probably be the bond ruptured in the DNA backbone.

Therefore we conclude that the rupture of a ds-DNA chain, consisting of homogeneous covalent bonds in series, does depend on both the time period under an external force as well as the environment. The height of the activation barrier of the covalent bonds in the DNA backbone on a surface in the liquid environment differs markedly from the isolated situation in vacuum and depends sensitively on the experimental conditions. The estimated small activation barrier of 45 k_BT can be explained with force-catalyzed chemical reactions such as hydrolysis. A relatively low rupture force in the range from 220 pN to 380 pN with a mean breaking time of 20 to 5 minutes, respectively, was obtained by using the DNA structural transition as a force calibration.

4.1.3 Conclusions from DNA part

In this section, studies on conformational and mechanical properties of single DNA were carried out. The conformational and mechanical properties of plasmid DNA correlate strongly with its double helix structure and the close circular form.

The DNA conformation can be defined in a controlled manner on a nanostructured template by variation of only one parameter i.e. the surface coverage: from supercoiled, double strand splitting, through stretched, over stretched backbone to relaxed circles and compact coils. The intrinsic topological properties of plasmid DNA plays an important role in the formation

of supercoiled and split conformations at low surface coverage and condensed coils at coverage above a monolayer. The self-assembly of DNA-amphiphile complexes on a surface leads to a stretched backbone. On monolayer coverage the DNA conformation can be regarded as close to the 2D projection of the conformation in the solution. Condensed coils are formed on and above monolayer coverage.

There is a coupling of force and conformation when plasmid DNA is stretched with small elongation. Plasmid DNA overwinds and splits locally to keep the base pairs stacking when stretched on a surface. The splitting of the double helix to two single strands is attributed to the release of torsional stress, which is built up during DNA stretching. The observation of only one splitting part in each molecule and the splitting length being proportional to the total length of the DNA chain suggests that the torsion-splitting effect is a long range effect which correlates the whole molecule.

DNA was also stretched to extreme elongation and eventually broken by the blowing manipulation, which allows the combination of dynamic load and static load to study the time-dependent mechanical properties of single DNA chains and extends the accessible pulling time from seconds in a conventional SFM vertical pulling experiment to more than half an hour in our case (and for less volatile pre-coatings for a day or more). A relatively large intrinsic activation rate constant of $(2.2 \pm 0.1) \times 10^{-7}$ s^{-1} is obtained and an activation barrier with an upper limit of 45 k_BT under the given environmental conditions is estimated. Furthermore, the conformational changes of DNA were traced in real time and a structural transition was observed during stretching. Using the internal force calibration given by the assumed transition from *B*-form to S-form DNA under force we have shown that ds-DNA has a mean breaking time of 5 minutes under a static load of 380 pN, which increases to 15 minutes at about half of the force load.

4.2 Amphiphilic dual molecular polymer brush

4.2.1 Synthesis of the dual brush block copolymer

The synthesis described here is part of a collaboration work with Prof. A. Laschewsky's group in University Potsdam and has been carried out by Dr. D. Zehm. The cylindrical brush block copolymer poly((ΦTEA-*g*-PS)-*b*-(CIPEA-*g*-NIPAM)) was synthesized by a combination of different controlled radical polymerization methods, mainly Reversible Addition Fragmentation Chain Transfer (RAFT), Atom Transfer Radical Polymerization (ATRP), and Nitroxide-mediated Polymerization (NMP) techniques. 2-phenyl-2-(2,2,6,6-tetramethyl-piperidine-1-oxyl)ethyl acrylate (ΦTEA) was polymerized through RAFT to form poly(ΦTEA). A second monomer named 2-chloropropionyloxyethyl acrylate (CIPEA) was attached to the polymer backbone via the same polymerization method to form block the copolymer poly(ΦTEA-*b*-CIPEA) (Fig. 4-9). Both monomers are so called inimers, which have not only a polymerizable double bond but also an initiating group. The different orthogonally addressable initiating sites along the poly(ΦTEA-*b*-CIPEA) backbone allow selective grafting polymerization steps through a "grafting from" strategy. Two different brushes were grafted to the polymer: a hydrophobic polystyrene brush and a hydrophilic poly(N-isopropylacrylamide) (NIPAM) brush, through ATRP and NMP respectively (Fig. 4-9). The final products were characterized by size exclusion chromatography (SEC), NMR and SFM. [31]

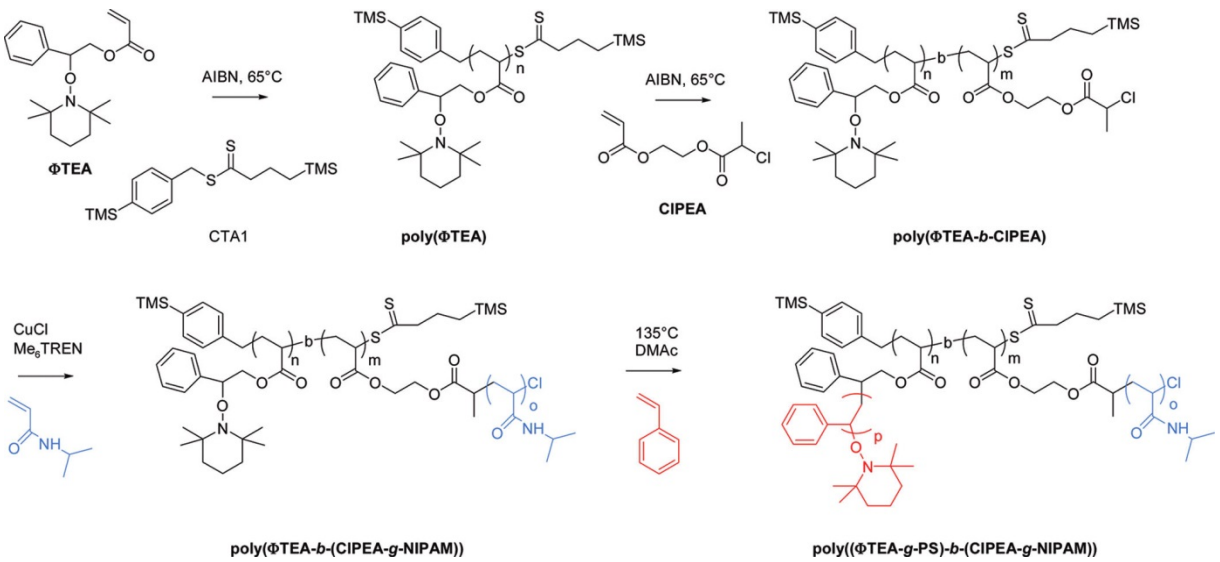

Figure 4-9. Synthesis of the amphiphilic dual brush copolymer poly((ΦTEA-*g*-PS)-*b*-(CIPEA-*g*-NIPAM)) by subsequent RAFT, ATRP, and NMP polymerizations.[31]

For comparison, two more brush block copolymers were synthesized through a similar strategy.[29, 30]

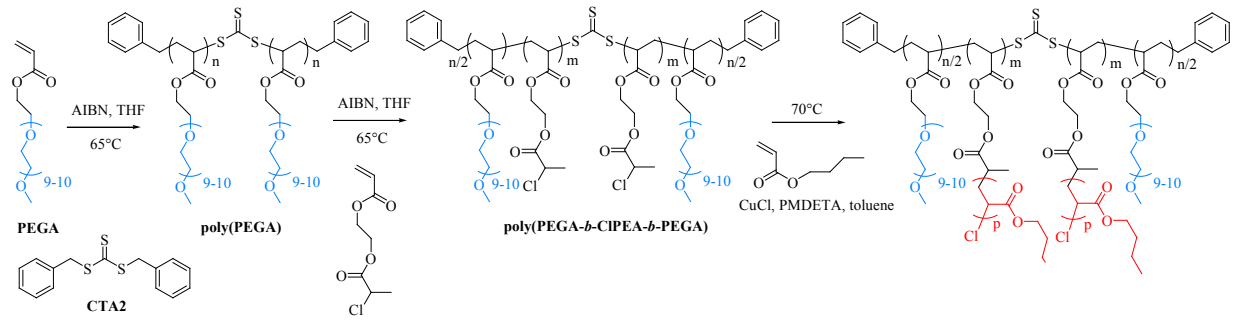

Figure 4-10. Synthesis of poly(PEGA-*b*-(CIPEA-*g*-BuA)-*b*-PEGA) dual brush block copolymer [30]

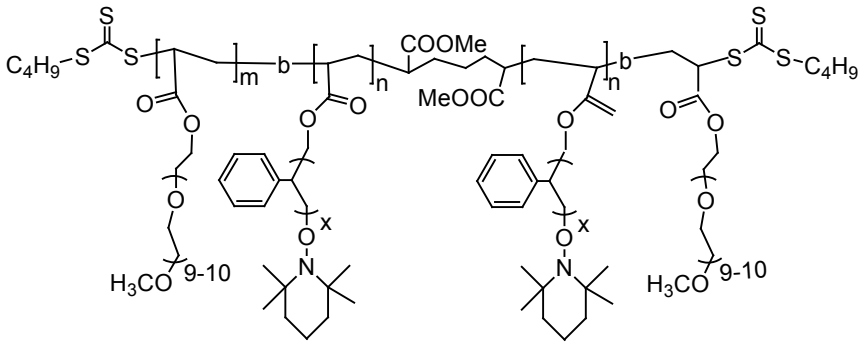

Figure 4-11. Chemical structure of poly(PEGA-*b*-(ΦTEA-*g*-PS)-*b*-PEGA) dual brush block copolymer [29]

4.2.2 Self-assembly of the dual brush block copolymer

The structure and the aggregation behavior of the amphiphilic dual brush block copolymer depend strongly on the solvent in which it is dissolved. In this work the polymers were dissolved in chloroform and water, respectively, and spin coated onto different surfaces to study their molecular structure as well as their supramolecular aggregates.

Brush polymer dissolved in chloroform

Poly((ΦTEA-g-$(PS)_{116}$)$_{96}$-b-(CIPEA-g-$(NIPAM)_{44}$)$_{359}$) was dissolved in chloroform and then deposited onto a mica surface. Fig. 4.12 displays the representative structures of the polymer on the surface. Nano-sized cylinder structures and their aggregates were observed (Fig. 4-12a). The small-sized cylindrical objects are attributed to single molecules. The distribution of the contour lengths of single molecules reveals a number-averaged length L_n = 33 nm (Fig. 4-12b). Zooming in onto a single molecule reveals a "tadpole-like" structure, with a relatively large "head" and a long "tail" (Fig. 4-12c). A cross section through the height profile along the molecular backbone reveals a height difference between the head (4.2 nm) and the tail (2.6 nm). Similar heights were observed in the profile of a dimer formed by two molecules positioned head-to-head (Fig. 4-12d). "Flower like" oligomers, also formed by a head-to-head manner, exhibited a higher head (6.1 nm) but a similar height of the tail compared with single molecules (Fig. 4-12e). The average full width of the tail is about 21 nm (Fig. 4-12d), taking into account a tip broadening effect[146] on the order of 4 nm, upon assuming a tip radius of 7 nm and an average height of the tail (spine and corona) around 1 nm.

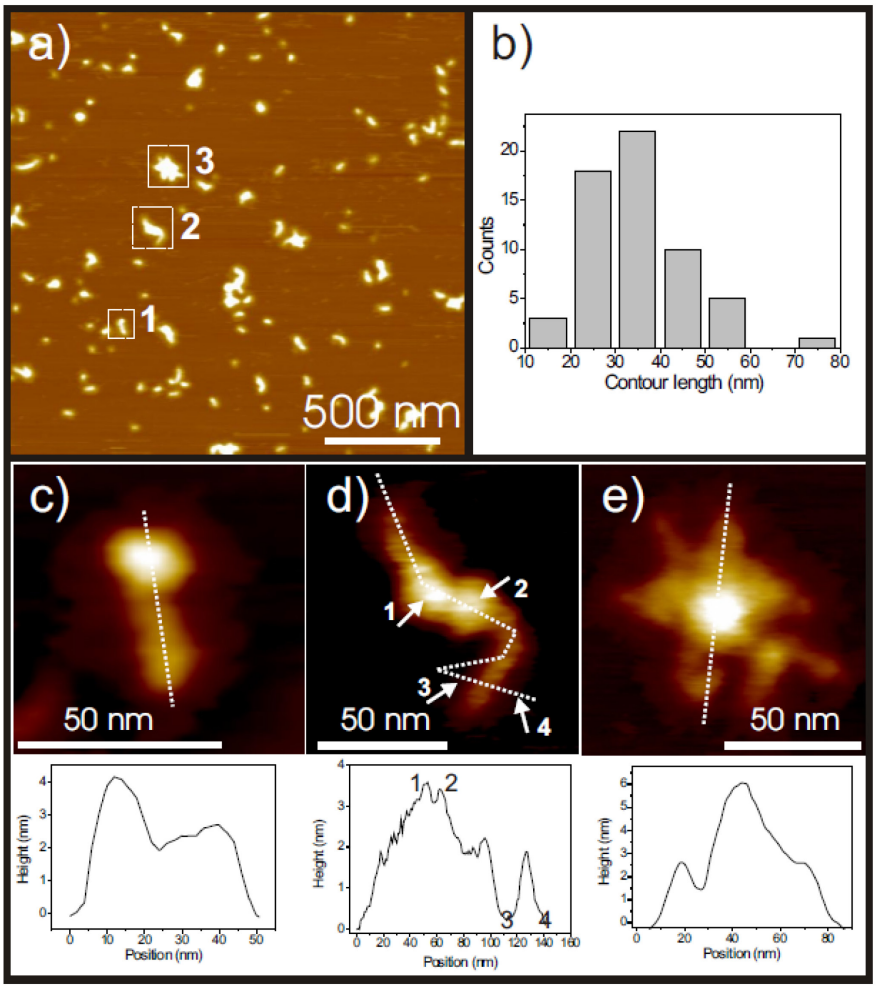

Figure 4-12. (a) SFM height image of poly(ΦTEA-g-$(PS)_{116})_{96}$-b-$(ClPEA-g-(NIPAM)_{44})_{359}$ deposited on mica by spin-coating from $CHCl_3$ solution. (b) Histogram of measured contour lengths of single molecules. Zoom-in on a): (c) single molecule 1, (d) dimer 2, and (e) oligomer 3, including their height profile cross sections. [31]

In previous work, the formation of a tadpole structure was observed for a brush polymer with a gradient of grafting density along the backbone, where the single molecules were incorporated in a condensed monolayer. The tadpole formation was attributed to the compression, upon which the end with the higher grafting density forms the "head".[147] Here we attribute the formation of isolated tadpole structures for one amphiphilic block copolymer molecule to the differences in the chemical structure of both blocks, side chain lengths, as well as the different wetting behaviors of both blocks on the surface.[148] During the drying phase, the hydrophilic NIPAM brush block favors contact with the polar mica surface, whereas the

hydrophobic PS brush block minimizes the contact. Thus, after solvent evaporation, the NIPAM brush block is directly adsorbed on the mica surface, while the collapsed PS brush block is located on top of the poly(NIPAM) block. The longer hydrophilic block (N = 359) with the shorter NIPAM side chains (N = 44) forms the "tail", while the shorter hydrophobic block (N = 96) with the longer PS side chains (N = 116) forms the spherical "head". This picture is supported by the height and width cross-section analysis. The fully extended NIPAM block has a width of 22 nm (44 × 2 × 0.25 nm), which is close to the experimental value of 21 nm. Our model agrees also with the work from Kumaki and Hashimoto, who showed that when a diblock copolymer PS-b-PMMA is deposited on a mica surface, the PS block collapses into a single PS coil on the top of PMMA chain.[149] The experimentally detected contour length ~ 33 nm, which corresponds 0.073 nm per repeating unit, is considerably shorter than the fully extended chain length (L_c = 455×0.25 nm = 113 nm for an all-trans conformation). Similar results (0.07 ~ 0.1 nm per repeating unit) were reported for a PMMA cylindrical brush polymer.[150] Thus, the main chain of the brush structure is not fully stretched, but at least locally coiled. The formation of "head" and "tail" conformation is also supported by looking into the length of the side chains. One can simply imagine that when the side chains are shorter than the polymer backbone, the polymer exhibits a cylindrical conformation, while in the opposite case, other conformations such as a "star like" conformation is preferred. In our particular case, the NIPAM side chains (N = 44) are shorter than the backbone (N = 359), thus they form the cylindrical "tail". On the other hand, the PS side chains (N = 116) are longer than the backbone (N = 96), thus they should favor a spherical "head". Finally, the formation of dimers and oligomers may be attributed to hydrophobic interactions between the PS brush blocks.[149]

Fig. 4-13 presents SFM images of the long amphiphilic dual brush poly((PEGA)$_{375}$-*b*-((CIPEA)$_{680}$-*g*-(BuA)$_{230}$)-*b*-(PEGA)$_{375}$) deposited on mica from chloroform solution. The polymer exhibits worm-like chains on the surface with a number average length of L_n= 107 nm (Fig. 4-13a and b). Considering the number average degree of polymerization of the main chain

of 1430, this value is less than 1/3 of the contour length of a fully extended chain L_c = 1430 × 0.25 nm = 357 nm. Figs. 4-13c and d reveal the structure of a single polymer brush at higher resolution. A thick spine with a height of 1.8 nm and a corona width of around 100 nm were detected (Fig. 4-13e). The middle BuA brush side chain has a theoretical fully extended length of 230 × 0.25 nm = 57 nm. This agreement suggests that the soft polyBuA side chains are highly extended, resulting in the well resolved corona in the SFM height and phase images. On the other hand, there is no indication of the stretched hydrophilic end blocks, which are each 94 nm long, nor the coiled end block, which should exhibit a diameter of 8 nm, assuming a PEO density of 1.1. g cm^{-3}. Moreover, the spine is surprisingly thick.

This puzzle is solved if one assumes a back-folding of the main chain, which reduces the contour length to less than half of the fully extended contour, and also explains that thickened spine. Similar back-folding has been observed for other brush polymers and charged dendronized polymers.[62, 151] The driving force may lay on the different affinities of the two different blocks to the surface. Alternatively, the stretched two-dimensional arrangement induces an orientation of the ester moieties at the polymer backbone, the resulting dipole moment being compensated by the ether moieties of the back-folded poly(PEGA) chains.

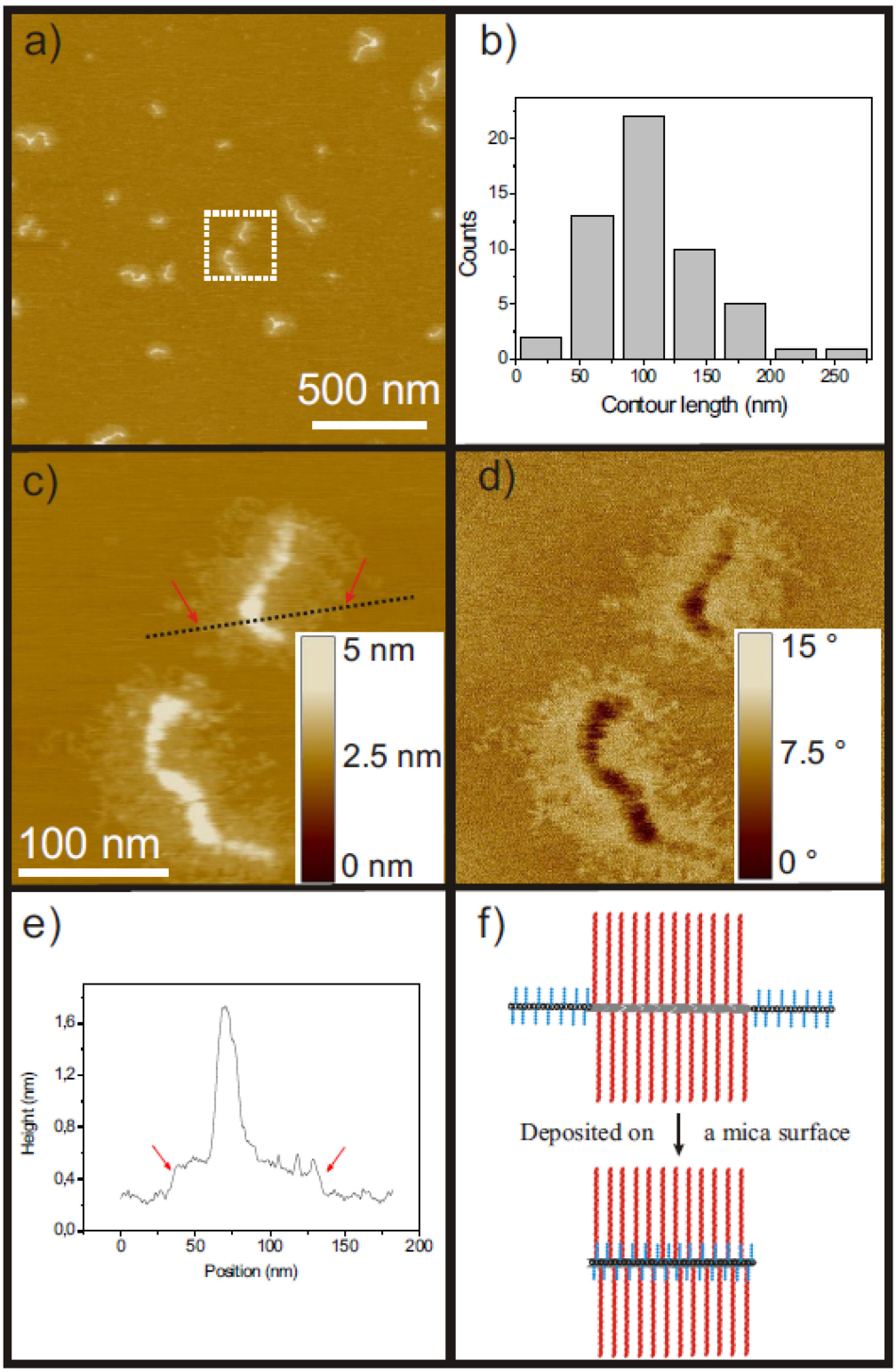

Figure 4-13. SFM imaging of poly((PEGA)$_{375}$-*b*-((CIPEA)$_{680}$-*g*-(BuA)$_{230}$)-*b*-(PEGA)$_{375}$) deposited on mica: a) height image; b) histogram of measured contour lengths; c) height image and d) phase image of Zoom-in area in a); e) height profile of dotted line in a), showing the height difference between the substrate, graft chains and the backbone; f) Back-folding model suggesting that the end blocks fold back underneath the middle block (top view).[30]

2.2.2 Brush polymer dissolved in water

In aqueous solution, the amphiphilic brush polymer forms aggregates due to the hydrophobic effect. The polymer aggregates were deposited on different surfaces, in particular mica, poly-L-ornithine pre-coated mica, and octadecylamine pre-coated HOPG, in order to investigate their shape and size distributions. In all cases, 2D clusters of slightly hexagonally distorted spherically shaped particles with similar sizes and size distributions were observed. However the size of the clusters varies largely, indicating different particle mobilities on these three surfaces.

Fig. 4-14 presents SFM images of poly((PEGA)$_{160}$-*b*-((ΦTEA)$_{108}$-*g*-(PS)$_{17}$)-*b*-(PEGA)$_{160}$) on a mica surface. 2D clusters with a size of a few microns were detected on the surface. The clusters were made compact by single particles up to 120 nm high, with the large particles in the center and the small ones at the edges. Zooming in, the cluster revealed that the particles had a slightly hexagonally distorted spherical shape. The average size of the particles is 62 nm (Fig. 4-14b).

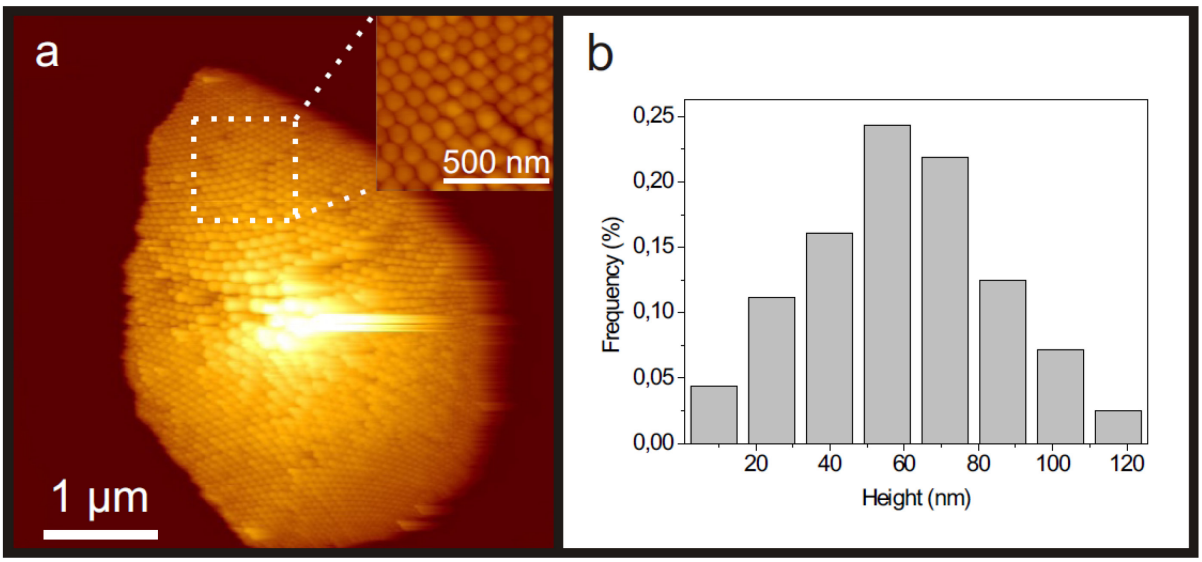

Figure 4-14. a) SFM height image of poly((PEGA)$_{160}$-*b*-((ΦTEA)$_{108}$-*g*-(PS)$_{17}$)-*b*-(PEGA)$_{160}$) on mica; b) height histogram of the particles in the cluster. [29]

The same sample was deposited onto poly-L-ornithine pre-coated mica, on which the particles had a small mobility. Compared with the cluster on mica, on poly-L-ornithine pre-coated mica smaller clusters were observed. Figure 4-15 displays a typical compact cluster of around 1 micron size, formed by single particles with an average size of 65 ± 20 nm on poly-L-ornithine pre-coated mica. A similar size self-sorting phenomenon like on the mica surface was observed: large particles being in the center and small ones at the edges.

Even smaller cluster were detected on alkylamine pre-coated HOPG surfaces. However a similar average size of the particles 73 ± 22 nm was observed (Fig. 4-16).

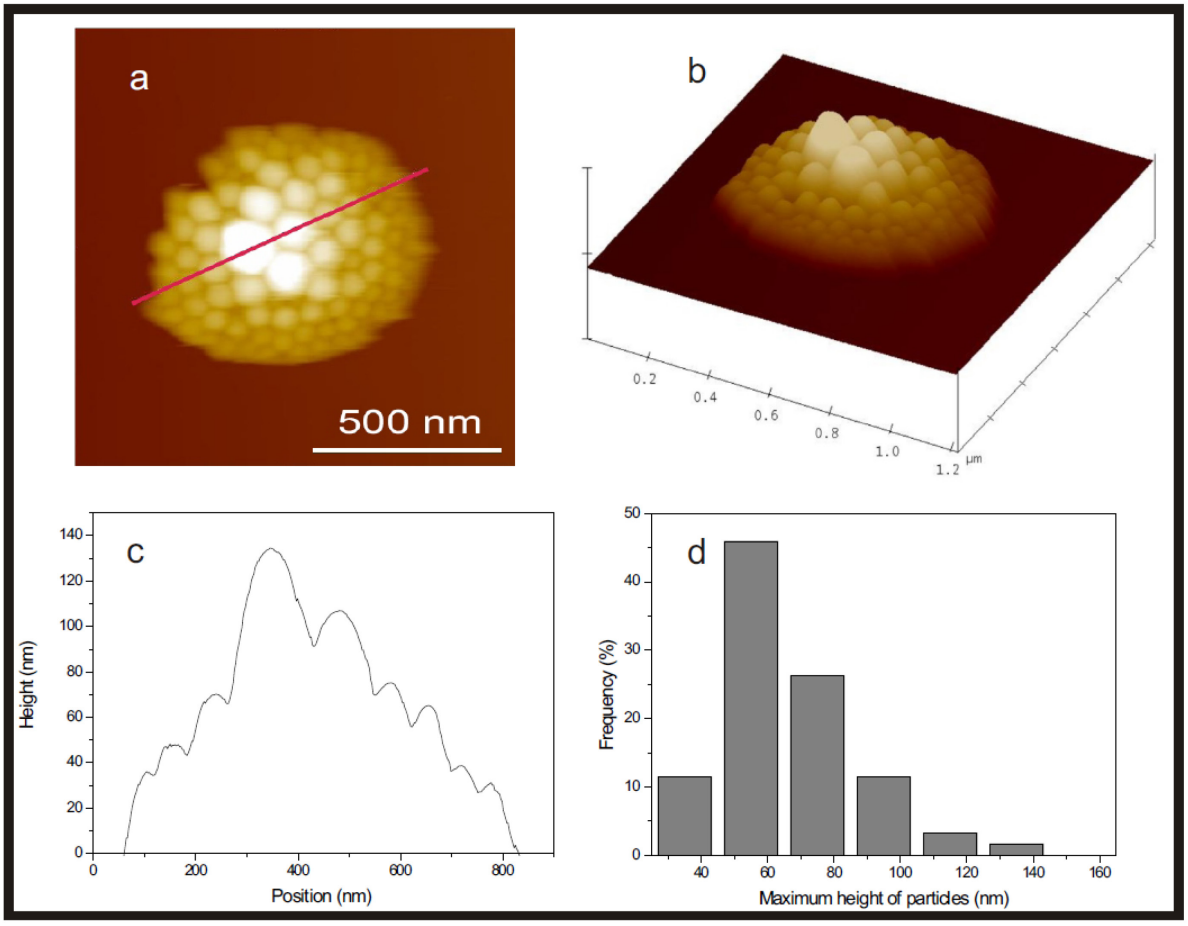

Figure 4-15. SFM height image of poly((PEGA)$_{160}$-*b*-((ΦTEA)$_{108}$-*g*-(PS)$_{17}$)-*b*-(PEGA)$_{160}$) on poly-L-ornithine pre-coated mica in a) top view, b) 3D representation, c) height profile along the line shown in a), d) height histogram of 61 particles with an average height amounts to 65 ± 20 nm.[29]

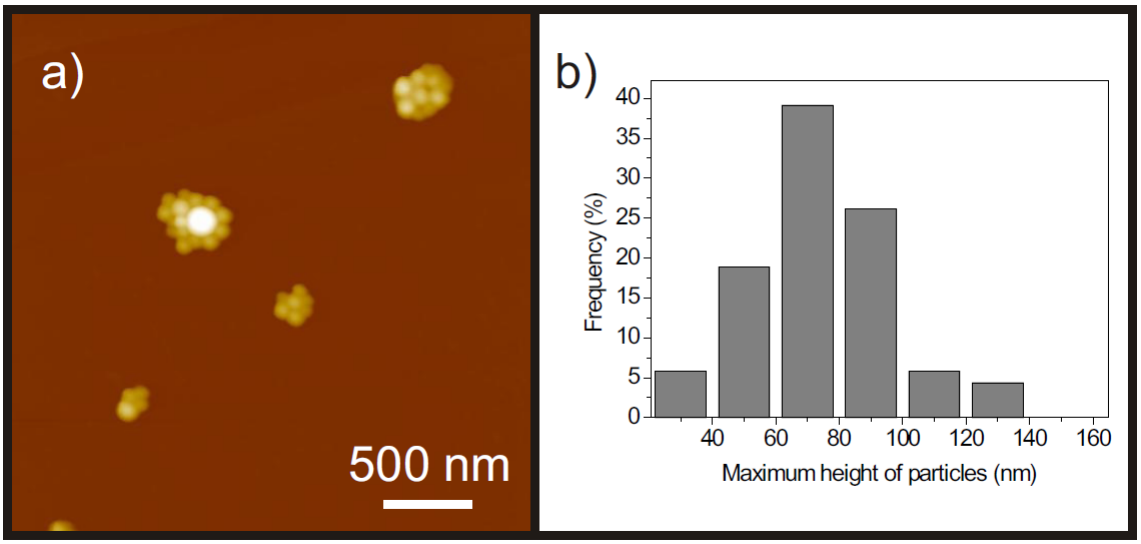

Figure 4-16. a) SFM height image of poly((PEGA)$_{160}$-*b*-((ΦTEA)$_{108}$-*g*-(PS)$_{17}$)-*b*-(PEGA)$_{160}$) on an alkylamine pre-coated HOPG surface; b) height histogram of the particles in the cluster.[29]

Table 4-2. Comparison of the particle and cluster size on different surfaces and in solution

Surfaces	Particle size	Cluster size	Surface Mobility
Mica	62 ± 15 nm	↓	↓
Pre-coated mica	65 ± 20 nm		
Pre-coated HOPG	73 ± 22 nm	Increase	Decrease
In solution (DLS)	65 nm	-	-

A comparison of the particle size and the cluster size on different surfaces is listed in Table 4-2. The similarity of the particle shape and of the size distributions on three different surfaces indicates that the particles are pre-formed in solution by aggregation of single amphiphilic brush copolymers, driving by the hydrophobic effect. Furthermore, the sizes are in good agreement with the ones obtained from dynamic light scattering in aqueous solution. The slightly hexagonal distortion of the particles indicates a soft shell. This picture corresponds to particles containing a hard polystyrene core with a high glass transition temperature, T_g, surrounded by a collapsed soft shell of poly(PEGA), in agreement with the DSC results. The

increasing cluster size in the order mica > pre-coated mica > pre-coated HOPG indicates that the mobility of the particles on mica is the highest under ambient conditions. This may be due to different wettability and also mobility of the dissolved adsorbents, which both increase from mica over pre-coated mica to pre-coated HOPG.

Particularly interesting is the ordering of the particles within a cluster according to their sizes. It has been reported that lyophilic colloidal particles can sort according to their sizes on surfaces of patterned wettability,[152] and polyelectrolyte-amphiphile complexes can self-sort on HOPG according to their lengths.[119] We attribute here the ordering to the drying process, during which the particles move toward the center of an evaporating droplet (Fig. 4-17).

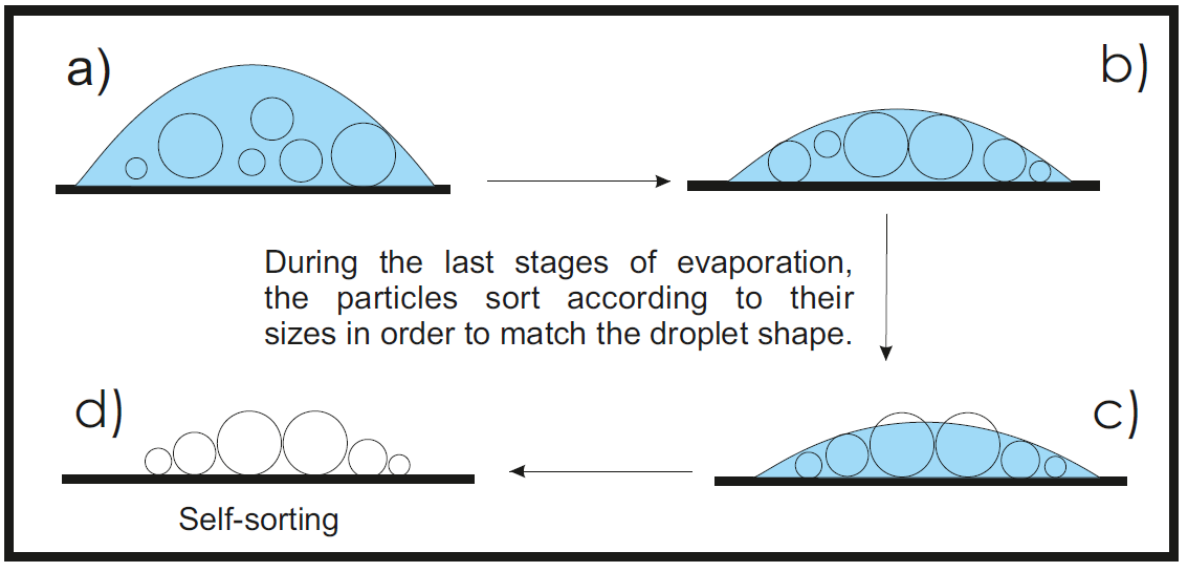

Figure 4-17. Schematic illustrating the self-sorting of amphiphilic polymer supramolecular aggregates according to their size during drying from an aqueous solution

4.2.3 Conclusion from amphiphilic dual polymer brush part

The conformation of an amphiphilic dual polymer brush on a surface depends on the adsorption dynamics as well as its conformation in solution, from which it is deposited onto the surface. The interaction between the polymer side chains and the surface plays an important role. Deposited from a selective solvent, the dual brush revealed worm-like chain conformations on the surface. Due to the different affinfinities of the side chains to the surface, parts of the

side chains collapsed while others fully extended on the surface, resulting in a “tadpole like” or a folding back structure. Deposited from an aqueous solution, supramolecular aggregates were detected on the surface. These aggregates formed clusters of different size and underwent a self-sorting process according to their size on the surface. The size of the clusters depends on the surface mobility.

4.3 Dendritic hyperbranched polyglycerol (hPG) as nanocarrier for drug delivery

In this section, I report studies on the characterization of amphiphilic dendritic hyperbranched polyglycerol (hPG) and its derivatives used as nanocarrier in drug delivery, focusing on the host-guest molecule interaction. It turns out that the transport properties of the nanocarrier relate directly with the chemical structure of the nanocarrier as well as its supramolecular aggregates.

4.3.1 Hyperbranched Polyglycerol

hPG and the derivatives were synthesized in Prof. Haag’s group in Free University Berlin carried out by Dr. Kurniasih through a ring-opening multi-branching polymerization reaction of glycidol under base conditions.[110, 153, 154] 1,1,1-tris (hydroxymethyl) propane (TMP) was used as the initiator (Fig. 2-25).

Fig. 4-18 presents the SFM height image of hPG with a weight average molecular weight of 10 000 g/mol on a mica surface. Single particles were observed. We attribute the single particles to single hPG molecules. The average size of the particles is about 5 nm, which fits with the results from a dynamic light scattering experiment. No aggregates were detected.

hPG is highly water soluble, with very good biocompatibility and low viscosity in solution due to no entanglement. It is a promising candidate for drug delivery. However due to the low hydrophobicity it shows no delivery properties for hydrophobic drugs. Therefore further modification of either the core or the shell is necessary.

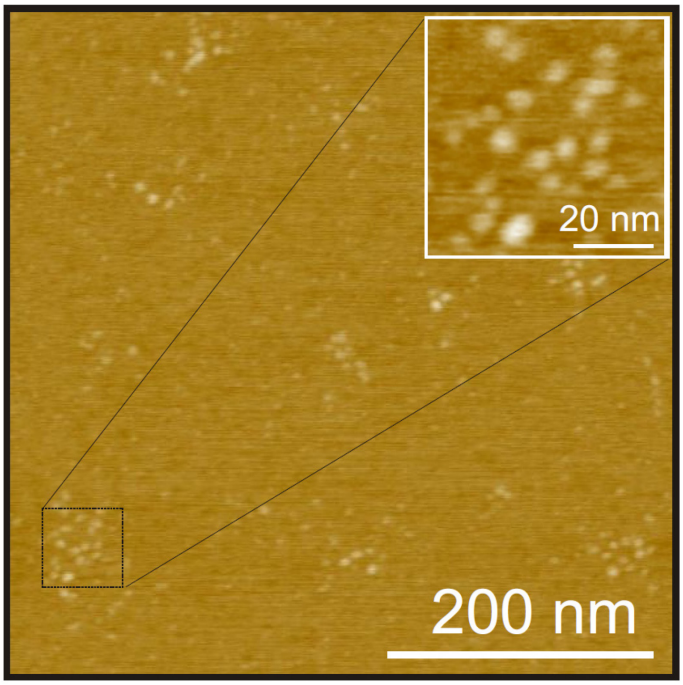

Figure 4-18. SFM height image of hPG with Mw = 10 000 g/ml deposited from aqueous solution (0.1 mg/ml) onto a mica substrate. Single particles with an average size of 5 nm were detected, which are attribute to single polymer molecules.

4.3.2 Core modified hyperbranched polyglycerol

In order to increase the hydrophobicity of the nanocarrier, hydrophobic chemical groups such as biphenyl and ester biphenyl were introduced into the core of the polymer by covalent coupling with the linear hydroxyl group in the core, which was achieved in a 3-steps strategy. The first step is to protect the terminal hydroxyl group by forming acetal groups with acetone dimethylacetal in the presence of *p*-toluenesulfonic acid (PTSA) as a catalyst. The linear hydroxyl groups were connected with the hydrophobic groups. In the last step, the polymer acetals were deprotected by treating a methanolic solution with an acidic ionic exchange resin (Fig. 4-19).

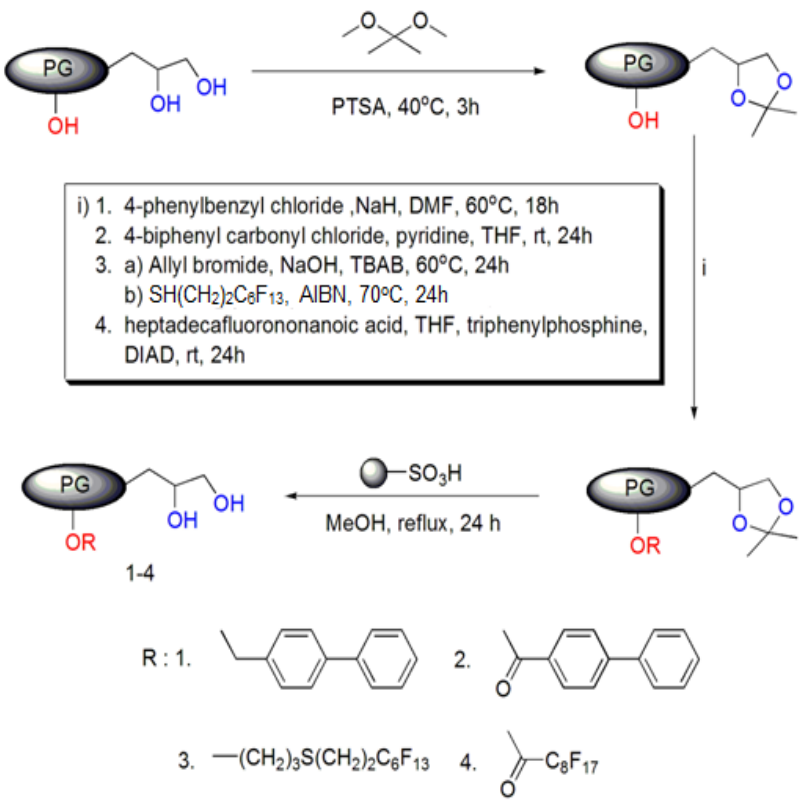

Figure 4-19. Synthesis of core-shell structures: i) The protection of the terminal –OH groups: PTSA, acetone dimethylacetal, 40°C, 3h; ii) The core functionalization of polyglycerol with three different groups (biphenyl ester, perfluorinated thiol and perfluorinated ester): a) pyridine, THF, 25°C, 18h; b_1) TBAB, 50% NaOH, 60°C, 24h; b_2) AIBN, 70°C, 24h; c) THF, triphenyl phosphine, DIAD, 2°C, 4h; iii) the deprotection of the terminal –OH groups: MeOH, reflux, 24h.[110]

The polymer was dissolved in water and various hydrophobic guest molecules such as nile red, pyrene, and nimodipine were added to test the transport properties of the system. The encapsulation of the guest molecules into the polymer was confirmed and quantitatively studied by spectroscopic methods.[110] Here I focus on the guest-host complexes and the interaction between them as well as the transport mechanism.

Fig. 4-20 presents the SFM results of Polymer 1 deposited on a mica surface. Above a concentration of 0.02 mg/mL, single particles and supramolecular aggregates with an average size of 20 nm were detected. The total volume of the aggregates decreases from high to low

concentration. When the normalized aggregate volume (volume/concentration) *vs* concentration is plotted, a transition is observed around 0.02 mg/mL, corresponding to about 1.2×10^{-6} mol/L. I attribute this to the critical aggregate concentration (CAC) of the polymer in water, which is close to the value of 2.0×10^{-6} measured by a pendant drop apparatus.[110]

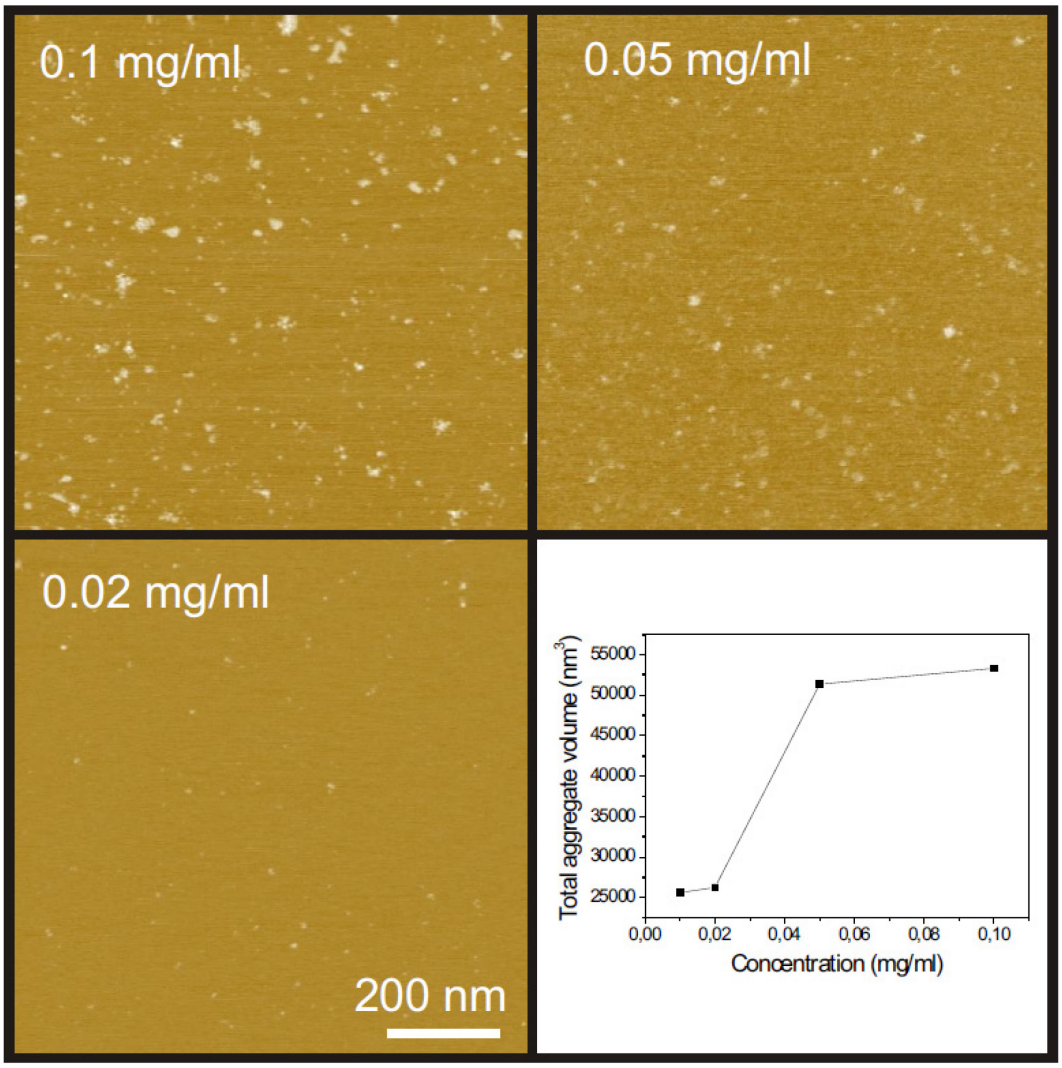

Figure 4-20. SFM height images of Polymer 1 deposited on a mica surface from different polymer solution concentrations a) 0.1 mg/mL, b) 0.05 mg/mL, c) 0.02 mg/mL, d) the normalized total aggregate volume *vs* solution concentration.

Fig. 4-21 presents the SFM results of the core modified hPG and nile red polymer complexes on a mica surface. Similar sizes of supramolecular aggregates of polymer 2 and 3 were detected (Fig. 3-4 a). No significant changes in size were observed when guest molecule

nile red was added. In the case of Polymer 4, much larger aggregates around 200 nm were observed, which seem to be flattened on the surface.

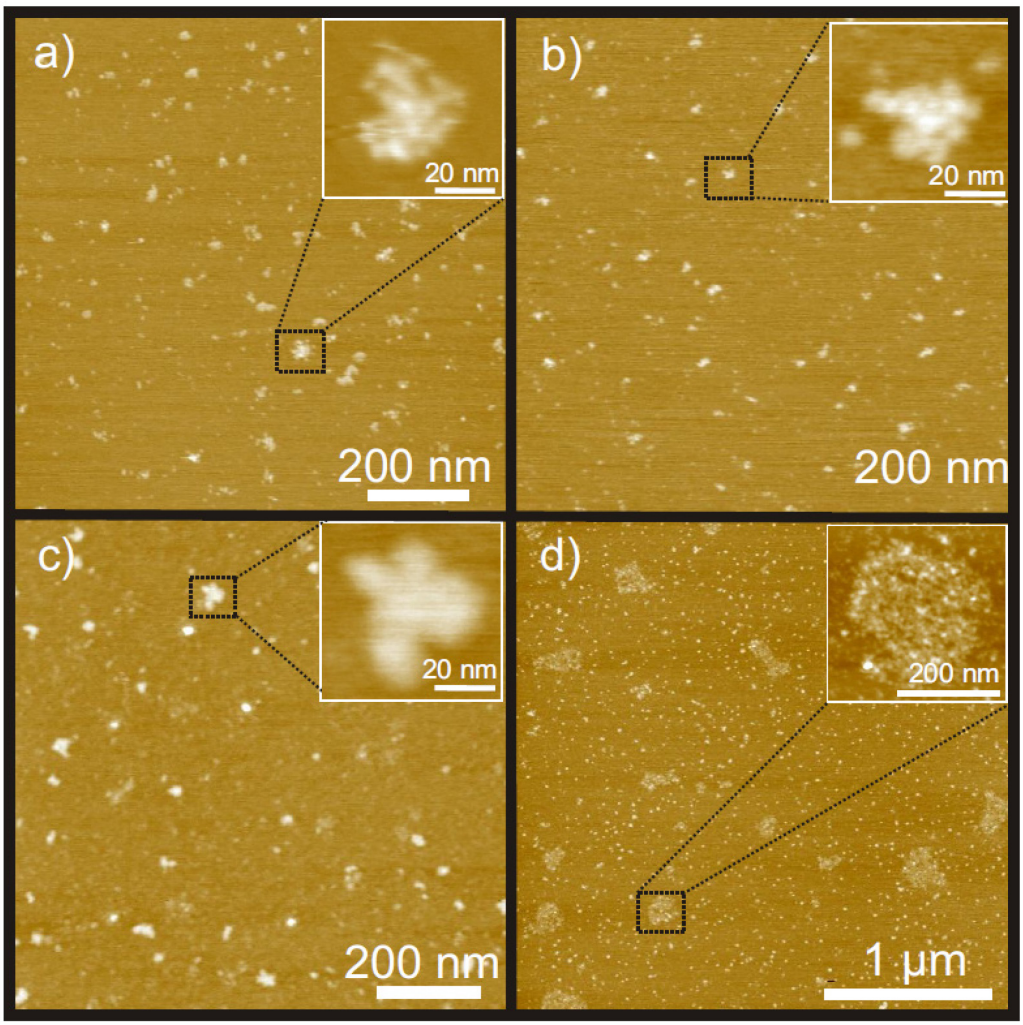

Figure 4-21. SFM height images with a height range of 5 nm of a) Polymer 2, b) Polymer 2 with nile red, c) polymer 3 with nile red, d) polymer 4 with nile red. The polymer concentration from which the samples were prepared was 0.1 mg/mL. [110]

The introduction of hydrophobic groups into the core of hPG increases the hydrophobicity of the system. The overlapping of the hydrophobic core of the polymer leads to the formation of supramolecular aggregates in aqueous solution due to the hydrophobic effect. The supramolecular aggregate behavior plays an important role in encapsulating the hydrophobic guest molecules. Guest molecules are encapsulated in the hydrophobic core of the

polymer through hydrophobic interaction as well as specific interactions such as π-π stacking between the aromatic rings of the polymer and guest molecules.[111]

4.3.3 Shell modified hyperbranched polyglycerol

PEG chains were covalently coupled to terminal hydroxyl groups by "click chemistry" to increase the hydrophilicity of the nanocarrier system. Fig. 4-22 shows the reactions pathways to modify the shell. The final product of hPG with PEG chains in the shell, Polymer 5, was obtained through 2 step reactions. For comparison, biphenyl groups were introduced as a spacer to connect the hPG and the PEG, Polymer 6, and inside the core as described before, Polymer 7.

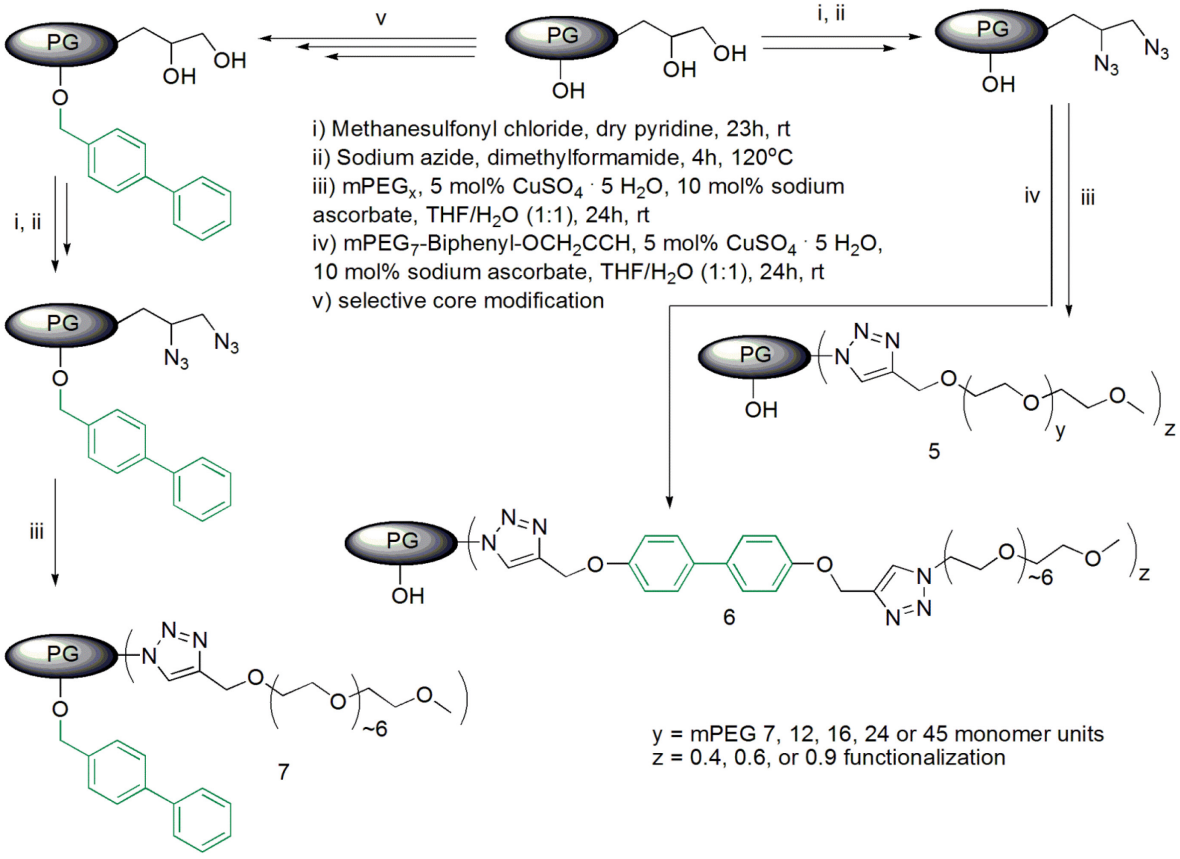

Figure 4-22. Chemical synthetic path way to achieve hPG with PEG shell (Polymer 5), hPG with biphenyl groups as a spacer (Polymer 6) and with biphenyl core and PEG shell (Polymer 7) [153]

Fig.4-23 displays Polymer 7 on mica, deposited from a chloroform solution of 0.1 mg/ml. Single round shape particles with an average size around 10 nm were detected on the surface. Particles with sizes up to 40 nm were observed (Fig. 4-23a). Zooming in on one of the particles reveals a double layer structure both in height and phase images: a center core and a surrounding shell (Fig. 4-23b and c). A height profile across the center of the particle indicated by the dotted line shows the height difference between the central core, the shell, and the substrate, respectively (Fig. 4-23d). Numbers and arrows in the height profile indicate the corresponding positions in the image.

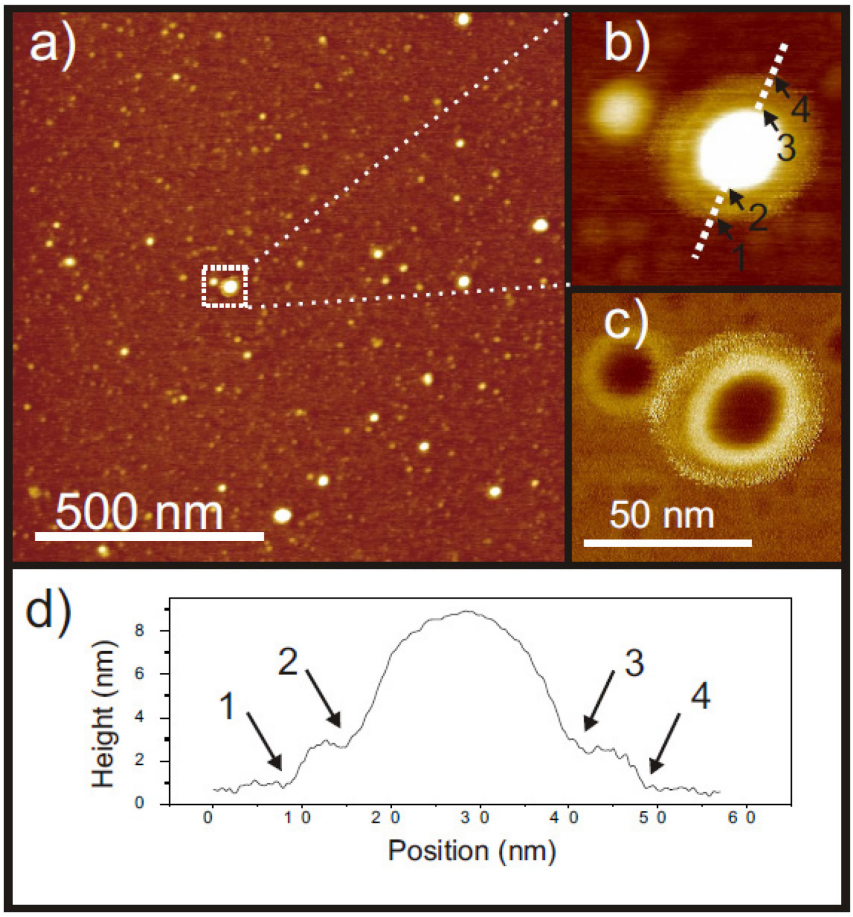

Figure 4-23. SFM images of Polymer 7 in chloroform (0.1 mg/ml): a) Height image, b) Zoom-in height, c) Phase image, d) Height profile indicated by the dotted line in 9b).

I attribute the single particles to single polymer molecules. The size difference between the single particles is attributed to the size distribution of the polymer. The different contrast in the center and the corona can be caused by different chemical components in the core and the shell, which confirms the core-shell structure of the molecule.

Fig. 4-24 presents SFM images of Polymer 7 with guest molecules deposited on a mica surface from aqueous solution (0.1 mg/ml). Single round shape small particles of around 10 nm in size as well as aggregates around 50 nm (Fig. 4-24a). Zoom in onto one of the aggregates revealed that the aggregate was formed by single small particles (Fig. 4-24b). The same polymer solution co-dissolved with nimodipine led to the formation of larger aggregates of about 200 nm on the surface (Fig. 4-24c). Again, a higher resolution height image reveals that the aggregates were formed by many small particles.

I attribute the small round shaped particles to single polymer molecules. The aggregates are formed by single molecules through hydrophobic core-core interactions as already discussed before.[110] The hydrophilic shell-shell interaction also plays a role in the formation of the aggregates, which is confirmed by the fact that there are no aggregates formed in a chloroform solution shown in Fig. 4-23. The presence of hydrophobic organic compounds such as nimodipine seems to enhance the interaction between the molecules, which results in the formation of larger aggregates. A further study on this point will be discussed in the following.

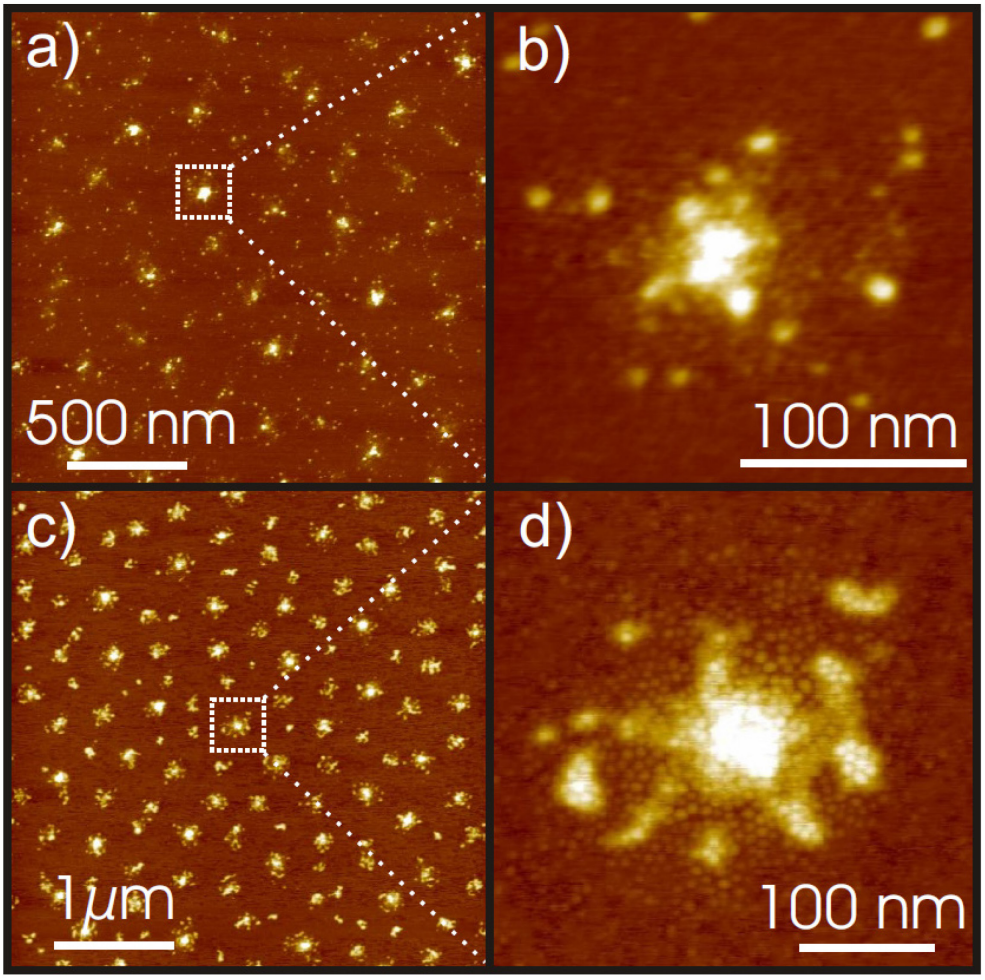

Figure 4-24. a) SFM images of Polymer 7 in water (0.1 mg/ml), b) Zooming in, c) Polymer 7 with Nimodipine, d) Zooming in.

4.3.4 Core shell modified hyperbranched polyglycerol

The core shell structure was achieved by first introducing hydrophobic groups in the core by a method described previously.[110] Thereafter PEG chains were attached to the shell through an esterification reaction (Fig. 4-25). PEG chains with 21 repeat units were used.

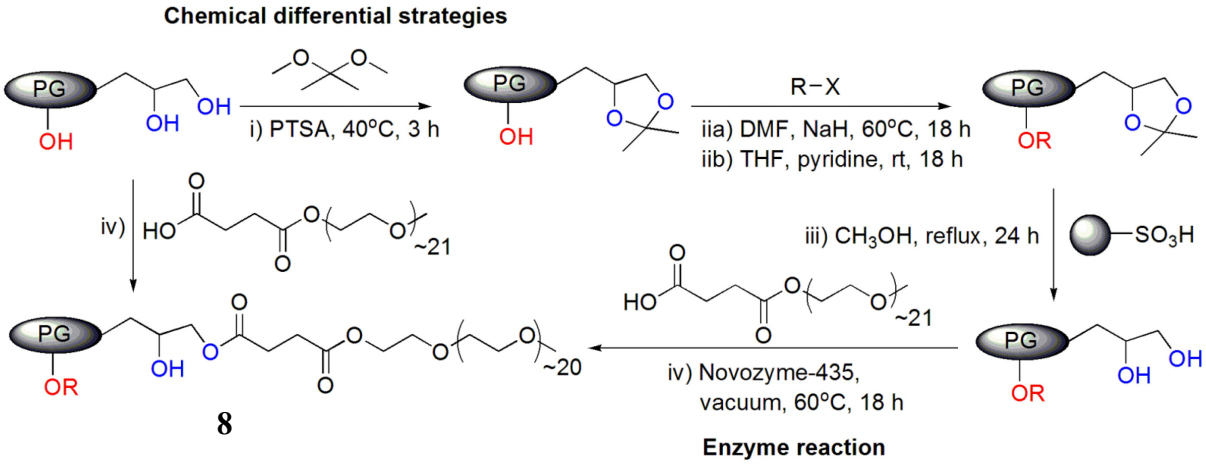

Figure 4-25. Chemical reaction path ways to achieve hPG with PEG shell and hydrophobic groups in the core [154]

The physical properties of the outcoming polymer product are listed in Table 4-3.

Table 4-3. Physical characteristics of the core-shell functionalized hPG derivatives

Polymer	-R	-R mol %	$mPEG_{22}$ mol %	M_n x 10^4	M_w/M_n	D_h nm (DLS)
8a	H	40	30	2.69	1.9	10*
8b	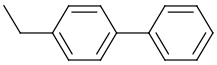	20	30	2.91	1.5	10.8
8c	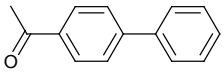	20	30	2.93	1.4	11.1

M_n number average molecular weight; M_w/M_n polydispersity; D_h mean hydrodynamic diameter. *The DLS experiment shows the aggregation as well as small particles of polymer with sizes up to 100 nm, single particles are around 10 nm.

Fig. 4-26 presents the SFM height images of core shell structured hPG (polymer 8) and the polymer guest molecule complexes deposited on a mica surface from aqueous solution. Single round shape particles with an average size of 10 nm were detected for pure polymers (Fig. 4-26a). No aggregates were observed. Similar size particles were obtained after pyrene was encapsulated into the polymer (Fig. 4-26b). However large aggregates with size around 200 nm were obtained for the polymer nile red complexes (Fig. 4-26c), which were decomposed into single particles around 10 nm upon dilution (Fig. 4-26d).

I attribute the single particles to single polymer molecules. A similar size (11 nm) was obtained from DLS experiments. Pyrene is located inside the core of the polymer, which led to an insignificant change in the size of the polymer-pyrene complex compared with pure polymer. This is confirmed by a similar size distribution from SFM and DLS results. On the other hand, nile red tends to locate in the outer shell of the polymer, connecting polymer molecules, which leads to the formation of large aggregates (100-200 nm). The nile red-polymer complexes were not stable and fell apart by dilution. Therefore the polymer transports guest molecules in both, a polymeric micelle and a unimolecule micelle mechanism. This model is confirmed by UV-VIS and fluorescence spectroscopy results.

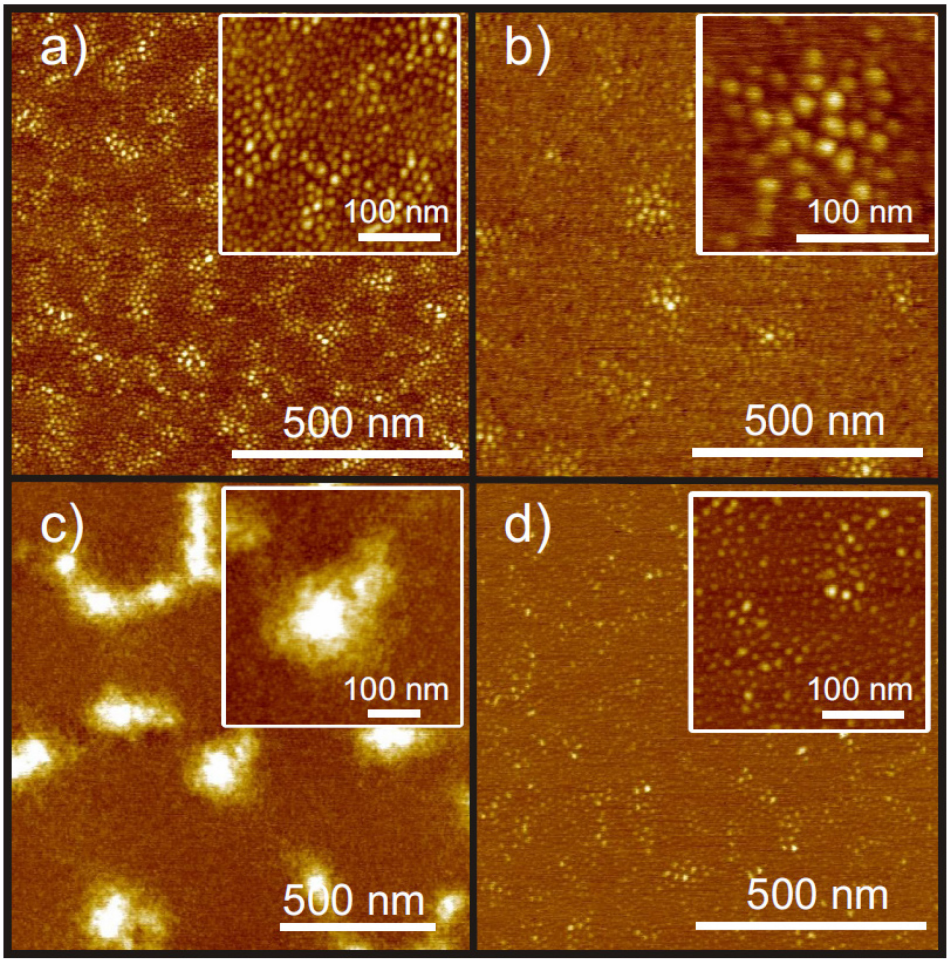

Figure 4-26. SFM height images of: a) 0.1 mg/mL hPG with PEG in the shell and biphenyl in the core, b) 0.1 mg/mL hPG-C loaded with pyrene, c) 0.1 mg/mL hPG-C loaded with nile red, and d) 0.02 mg/mL polymer loaded with nile red.

Fig. 4-27 shows the UV-VIS spectroscopy results of pyrene loaded Polymer **8c**. The wavelength of maximum adsorption (λ_{max}) stays constant on variation of the polymer concentration, while the absorbance enhances with increasing polymer concentration. A linear dependence of absorbance on polymer centration is found (Fig. 4-27b). Comparing the spectra data with those of pyrene in 60 wt% dioxane and using those as calibration, one can calculate the encapsulated pyrene concentration in the polymer. At a polymer concentration of 0.75 mg/ml, an average of 1.4 mole pyrene was encapsulated in one mole Polymer **8c** and 2 mole pyrene was encapsulated in one mole Polymer **8b**. The polarity index of pyrene (I_3/I_1, the ratio of the intensities of the third (384 nm) and first (372 nm) vibronic peaks in the emission

spectrum) can be used as an indicator of the hydrophobicity of the environment in which the pyrene is located.[155] The fluorescence spectroscopy study indicated that the I_3/I_1 ratios of pyrene in Polymer **8b** and Polymer **8c** were 1.02 and 0.97, respectively.[154] These values were significantly larger than those of ethylene glycol (0.63) and methanol (0.75), which have a similar composition as the PG shell. Similar results (1.08) were reported for hPG with a polyethylene core.[156] Therefore I conclude that pyrene was encapsulated in the hydrophobic core of hPG. The linear dependence of absorbance on the polymer centration suggests a "unimolecular micelle-type" transport mechanism.

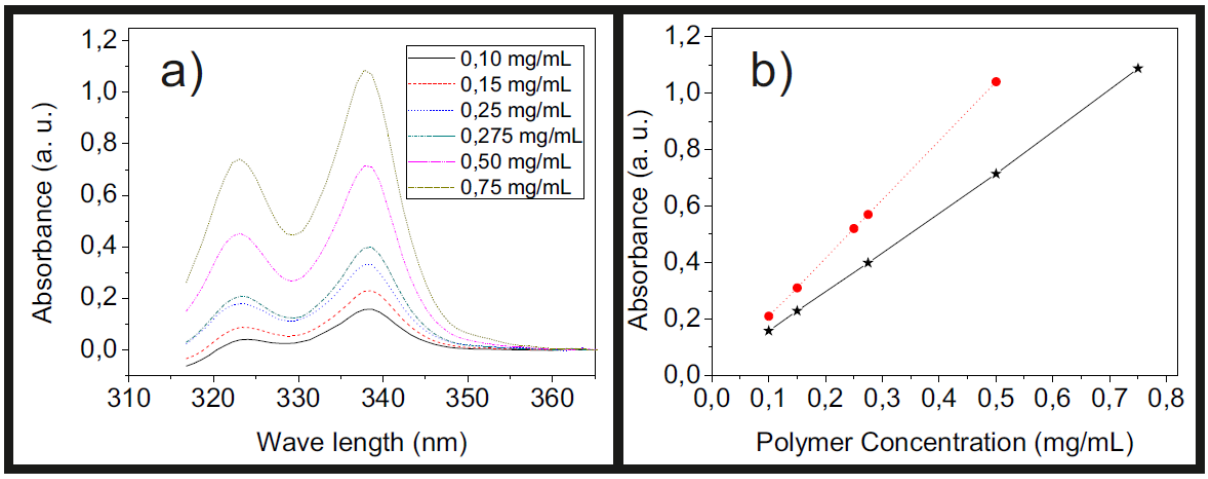

Figure 4-27. a) UV-VIS spectra of pyrene loaded Polymer **8c**, b) linear dependence of loaded pyrene on polymer concentration: Polymer **8b** (circle), Polymer **8c** (star). [154]

Fig. 4-28 presents typical UV-VIS spectra of nile red-loaded hPG-C in water. At low amounts of the dye (5 and 10 µL), a single broad peak around 570 nm was observed. In general, absorbance increases with an increasing amount of nile red added to the system within the experimental concentration range with vibrations between 30 µL and 50 µL (Fig. 4-28a). At amounts higher than 20 µL an additionally growing peak around 670 nm was observed, with an increasing amount of nile red. For example, from 20 µL to 30 µL, the extra peak remains almost the same; while from 30 µL to 40 µL, it doubles its height and stays constant to 60 µL

(Fig. 4-28a). A shoulder peak around 510 nm becomes obvious to the eye after 60 µL and dominates from 100 µL. Fig. 4-28b shows the corresponding fluorescence emission spectra of dye-loaded hPG-C polymers excited at 550 nm. Within the experimental concentration range, all emission curves exhibit single broad peaks with a peak maximum around 630 nm, which slightly shifts to longer wavelengths with a rising amount of nile red, e. g., from 626 nm at 5 µL to 636 nm at 200 µL (Fig. 2b). Similar to the absorbance in excitation spectra, the fluorescence intensity rises from 5 µL to 30 µL and oscillates between 30 µL and 50 µL. It reaches the maximum intensity at 60 µL and then drops, saturating after 100 µL.

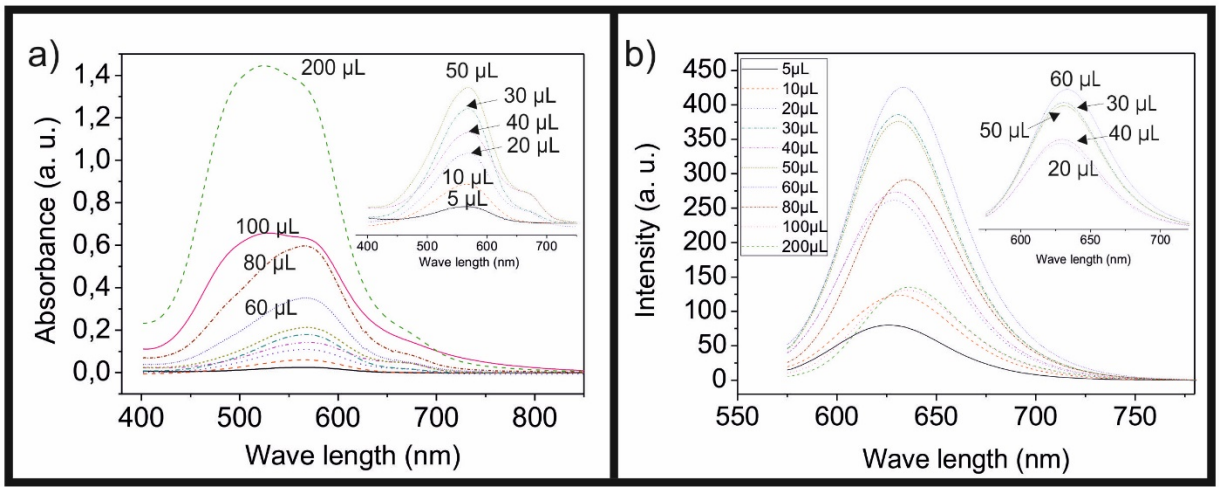

Figure 4-28. Spectroscopic studies of nile red loaded Polymer 8c: a) UV-VIS, b) fluorescence [154]

In order to separate the three peaks in the UV-VIS spectra, a 3-peak Gaussian fitting is used. All curves from 20 µL to 200 µL are fitted (Fig. 4-29a, b, c, and d). The three peaks are shown by blue dotted lines. Fig. 4-29e demonstrates the variation of emission intensity between 5 µL and 200 µL (squares) as well as the peak height ratio between Peak 2 to Peak 3 (triangles). I attribute Peak 2 to monomer absorbance and Peak 3 to J-aggregates' absorbance, which will be discussed in the following.

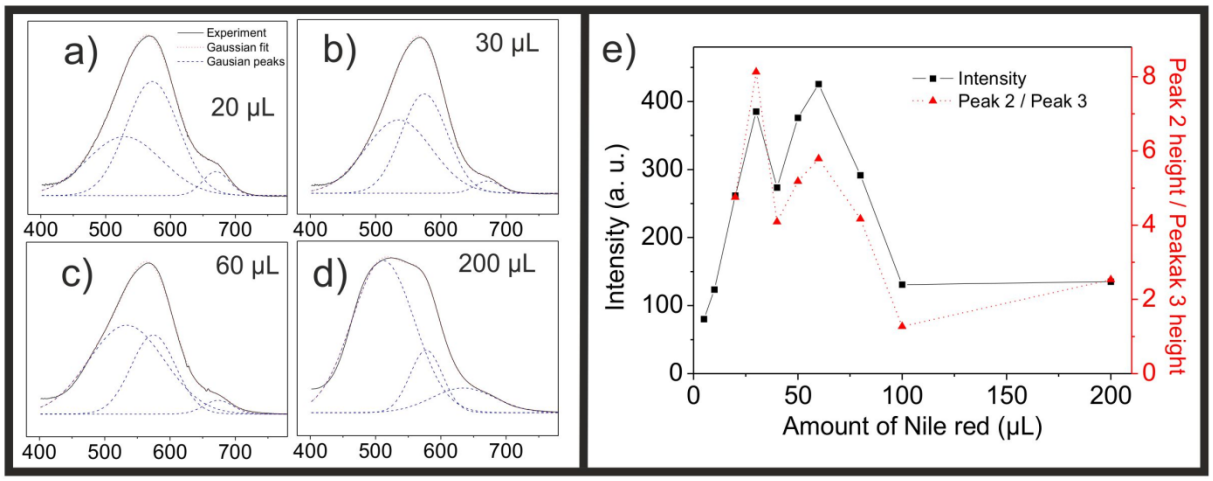

Figure 4-29. Gaussian fitting of the excitation curves at (a) 20µL, (b) 30µL, (c) 60µL, and (d) 200µL together with (e) variation of emission intensity (square) as well as the ratio of Peak 2 to Peak 3. [154]

Nile red has been extensively used as a probe molecule for solvent polarity and hydrophobicity. Due to its solvatochromic behaviour, the absorption and emission maxima strongly depend on the polarity of the environment.[157] From the spectroscopic results, absorption maxima between 558 nm to 566 nm as well as emission maxima between 626 nm to 636 nm were observed (Fig. 4-28). These values fit well with the absorption maxima of nile red in a mixture of 60 wt% of dioxane in water (λ_{max}=559 nm ε = 40.9), respectively, as well as in ethylene glycol (λ_{max}=557 nm). By looking carefully at the core-shell structure of the host molecule, one can infer that nile red preferably resides within the outer layer of the host molecule, where the local polarity is close to that of ethanol and ethylene glycol. The peak in the lower wavelength regions appears to be around 510 nm, which is attributed for H-aggregate and the peak around 670 nm, which is attributed for the J-aggregate of nile red.

The formation of dye aggregates is also supported by examining the changes of fluorescence on the nile red concentration. The excitation is carried out at 550 nm, which is mainly the monomer absorption region. Since the absorption band of the J-aggregate overlaps with the emission band of the monomer and the J-aggregate is the main fluorescence quench factor, the fluorescence intensity depends on the ratio of monomer to J-aggregate. A similar

dependence of fluorescence and monomer to J-aggregate ratio on the nile red concentration (Fig. 4-29e) soundly confirms the co-existence of nile red monomer and aggregate in the system. The formation of nile red aggregate is further supported by DLS and SFM size examination experiments (Fig. 4-26). In summary, I conclude that nile red resides in the outer shell of hPG, connecting hPG molecules to form aggregates. The aggregates break apart upon dilution. Therefore a "polymeric micelle type" transport mechanism is implied.

By comparing the UV-VIS spectra of co-encapsulated pyrene and nile red with only pyrene or nile red encapsulated in the polymer (Fig. 4-30), one may see the intensity and peak maxima of pyrene and nile red remained unchanged. This result implies that there is no strong interaction between two guest molecules, which confirms our hypothesis that pyrene stays in the core of the hPG while nile red is located in the outer shell.

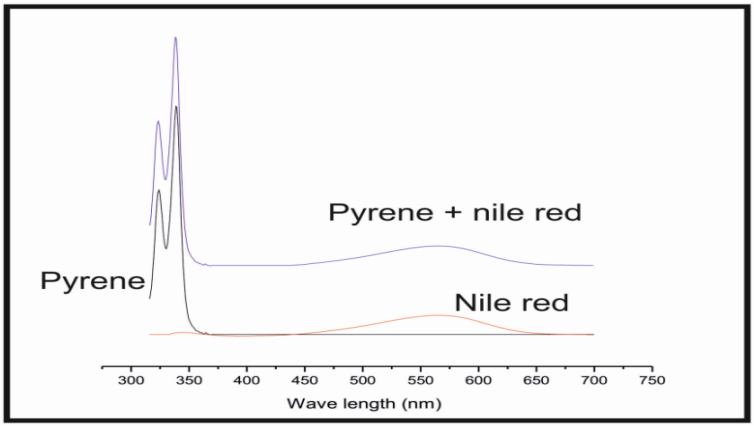

Figure 4-30. UV-VIS spectra of pyrene (balck), nile red (red), and c) nile red and pyrene co-loaded in Polymer **8c** [154]

The release study of the complexes revealed that the nile red was released under acid conditions and upon dilution, while pyrene was released in the presence of enzyme, which reacts selectively with the ester bond in the core.[154] In summary, the core-shell structured hPG solubilized and released pyrene and nile red by different mechanisms. Pyrene is encapsulated in the hydrophobic core of the polymer, which reveals the unimolecular micelle type carrier properties of the polymer. On the other hand, nile red was solubilized in the polymer

aggregates and the aggregates broke down into single molecules upon dilution, which indicates polymeric micelle-like transport properties (Fig. 4-31). The different encapsulation mechanisms and controlled release profiles make this polymer a promising candidate for simultaneous delivery of two hydrophobic drugs, which is a current need for combination therapy, e.g. in cancer treatment.

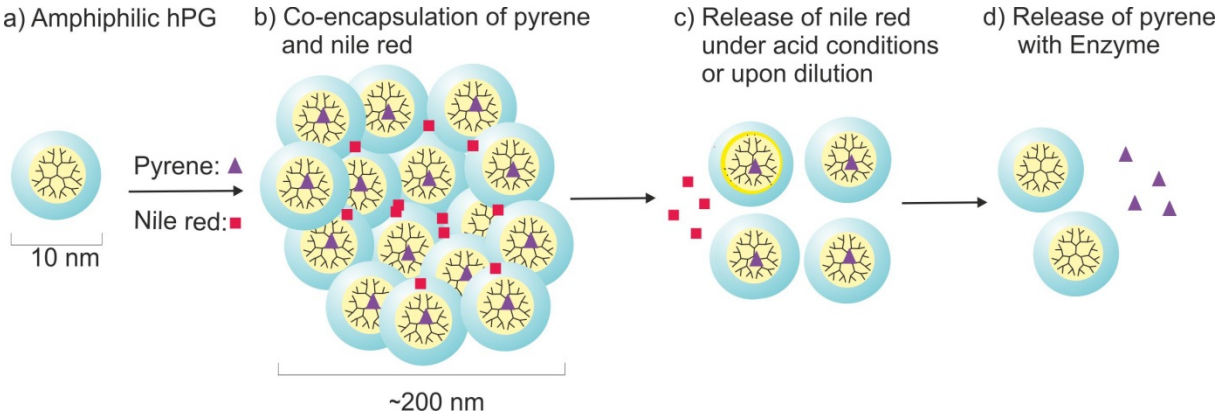

Figure 4-31. Transport mechanisms and release profiles of the core shell structured polymer

4.3.5 Conclusion from hPG part

The transport properties of hPG strongly relate with the polymer structure. The chemical structures of the core and the shell play an important role. Modification of the core increases the hydrophobicity of the system, which leads to supramolecular aggregates in aqueous solution. It provides a universal encapsulation of the hydrophobic drugs through the hydrophobic effect in an aqueous solution. It allows also specific interactions such as π-π stacking and dipole-dipole interaction between the host and the guest. Modification of the shell leads to better water solubility and solubility of polar guest molecules in an organic solvent. The both core and shell modified structure leads to a large hydrophobic gradient across the polymer molecule, which results in better selective transport capacities and better water solubility. Co-loading of two drugs and controlled release is possible, which makes it a promising candidate for simultaneous delivery of two hydrophobic drugs in cancer combination therapy.

5. Summary and Conclusions

In this work three polymer systems were explored, in order to describe structure-property-application relations on a single molecule level: DNA, amphiphilic cylindrical polymer brushes and amphiphilic core-shell structured hyperbranched polyglycerol (hPG). Studies of their conformational and mechanical properties in solution as well as on surfaces were carried out. Most important results and conclusions are outlined in the following.

5.1 DNA

I discovered a simple high throughput method to control single DNA conformations on an alkylamine modified graphene surface. Upon the variation of only one parameter, i.e. the surface coverage, the following conformations of plasmid double stranded DNA can be obtained: supercoiled, double strand splitting, stretched, over stretched backbone, relaxed circles and compact coils. The resulting DNA conformation is caused by an interplay of the intrinsic topological properties of plasmid DNA and the interaction between the substrate and the DNA-amphiphile complexes.

In particular, the intrinsic twist-stretch coupling of DNA was directly confirmed on the surface. Plasmid DNA overwinds and splits locally to keep the base pairs stacking when stretched on the surface. The splitting of the double helix into two single strands is attributed to the release of torsional stress, which is built up during DNA stretching. The observation of only one splitted part in each molecule and the splitting length, being proportional to the total length of the DNA chain, suggests that the torsion-splitting effect is a long range effect which correlates the whole molecule.

For extreme elongation and finally chain rupture, a relatively large intrinsic activation rate constant of $(2.2 \pm 0.1) \times 10^{-7}$ s^{-1} is obtained and an activation barrier with an upper limit of 45 k_BT under the given environmental conditions is estimated. Furthermore, the conformational changes of DNA were traced in real time and a structural transition was observed during

stretching. Using the internal force calibration given by the assumed transition from B-form to S-form DNA under force I have shown that ds-DNA has a mean breaking time of 5 minutes under a static load of 380 pN, which increases to 15 minutes at about half of the force load.

5.2 Cylindrical polymer brushes

Deposited from a chloroform solution, the dual brushes exhibit worm-like chain conformations on the surface. Due to different affinities of the side chains to the surface, parts of the side chains collapsed while others fully extended on the surface, resulting in a "tadpole like" or a folding back structure. Deposited from an aqueous solution, supramolecular aggregates were detected on the surface. These aggregates formed clusters of different size and underwent a self-sorting process according to their size on the surface. The size of the clusters depends on the surface mobility.

5.3 Core-shell structured hPG

The amphiphilic core-shell structured nanocarrier exhibited innovative bi-functional transport capacities for hydrophobic guest molecules. It encapsulates and transports in both a "unimolecular micelle" and a polymeric micelle type mechanism. These transport properties originate from the core-shell structure of hPG, which creates a large hydrophobic gradient across the polymer molecule, leading to improved selective transport capacities and better water solubility. The capacity of co-loading of two drugs and controlled release makes it a promising candidate for simultaneous delivery of two hydrophobic drugs in cancer combination therapy.

6. Reference

1. Cluzel, P., et al., *DNA: An extensible molecule.* Science, 1996. **271**(5250): p. 792-794.
2. Smith, S.B., Y.J. Cui, and C. Bustamante, *Overstretching B-DNA: The elastic response of individual double-stranded and single-stranded DNA molecules.* Science, 1996. **271**(5250): p. 795-799.
3. Leger, J.F., et al., *Structural transitions of a twisted and stretched DNA molecule.* Physical Review Letters, 1999. **83**(5): p. 1066-1069.
4. Bustamante, C., et al., *Single-molecule studies of DNA mechanics.* Current Opinion in Structural Biology, 2000. **10**(3): p. 279-285.
5. Gore, J., et al., *DNA overwinds when stretched.* Nature, 2006. **442**(7104): p. 836-839.
6. Ghorbani, M. and F. Mohammad-Rafiee, *Twist-stretch correlation of DNA.* Physical Review e, 2008. **78**(6).
7. Adamcik, J., et al., *Quantifying supercoiling-induced denaturation bubbles in DNA.* Soft Matter, 2012. **8**(33): p. 8651-8658.
8. Sarkar, A., et al., *Structural transitions in DNA driven by external force and torque.* Physical Review E, 2001. **63**(5): p. 10.
9. Bustamante, C., Z. Bryant, and S.B. Smith, *Ten years of tension: single-molecule DNA mechanics.* Nature, 2003. **421**(6921): p. 423-427.
10. Adam, R.E. and B.H. Zimm, *SHEAR DEGRADATION OF DNA.* Nucleic Acids Research, 1977. **4**(5): p. 1513-1537.
11. Bensimon, D., et al., *Stretching Dna with A Receding Meniscus - Experiments and Models.* Physical Review Letters, 1995. **74**(23): p. 4754-4757.
12. Clausen-Schaumann, H., et al., *Mechanical stability of single DNA molecules.* Biophysical Journal, 2000. **78**(4): p. 1997-2007.
13. Friedsam, C., et al., *Dynamic single-molecule force spectroscopy: bond rupture analysis with variable spacer length.* Journal of Physics-Condensed Matter, 2003. **15**(18): p. S1709-S1723.
14. Grandbois, M., et al., *How strong is a covalent bond?* Science, 1999. **283**(5408): p. 1727-1730.
15. Beyer, M.K., *The mechanical strength of a covalent bond calculated by density functional theory.* Journal of Chemical Physics, 2000. **112**(17): p. 7307-7312.
16. Evans, E. and K. Ritchie, *Dynamic strength of molecular adhesion bonds.* Biophysical Journal, 1997. **72**(4): p. 1541-1555.
17. Braun, E., et al., *DNA-templated assembly and electrode attachment of a conducting silver wire.* Nature, 1998. **391**(6669): p. 775-778.
18. Loweth, C.J., et al., *DNA-based assembly of gold nanocrystals.* Angewandte Chemie-International Edition, 1999. **38**(12): p. 1808-1812.
19. Monson, C.F. and A.T. Woolley, *DNA-templated construction of copper nanowires.* Nano Letters, 2003. **3**(3): p. 359-363.
20. Winfree, E., et al., *Design and self-assembly of two-dimensional DNA crystals.* Nature, 1998. **394**(6693): p. 539-544.
21. Mao, C.D., et al., *Logical computation using algorithmic self-assembly of DNA triple-crossover molecules.* Nature, 2000. **407**(6803): p. 493-496.
22. Yurke, B., et al., *A DNA-fuelled molecular machine made of DNA.* Nature, 2000. **406**(6796): p. 605-608.
23. Yan, H., et al., *A robust DNA mechanical device controlled by hybridization topology.* Nature, 2002. **415**(6867): p. 62-65.
24. Simmel, F.C. and W.U. Dittmer, *DNA nanodevices.* Small, 2005. **1**(3): p. 284-299.
25. Xu, M.S., et al., *Conformation and local environment dependent conductance of DNA molecules.* Small, 2005. **1**(12): p. 1168-1172.
26. Xu, M.S., et al., *Conductance of single thiolated poly(GC)-poly(GC) DNA molecules.* Applied Physics Letters, 2005. **87**(8).

27. Xu, M.S., D. Fujita, and N. Hanagata, *Perspectives and Challenges of Emerging Single-Molecule DNA Sequencing Technologies.* Small, 2009. **5**(23): p. 2638-2649.
28. Severin, M., et al., *Manipulation and overstretching of genes on solid substrates.* Nano Letters, 2004. **4**(4): p. 577-579.
29. Zehm, D., et al., *Amphiphilic Dual Brush Block Copolymers as ΓÇ£Giant SurfactantsΓÇØ and Their Aqueous Self-Assembly.* Langmuir, 2009. **26**(5): p. 3145-3155.
30. Zehm, D., et al., *Synthesis and self-assembly of amphiphilic semi-brush and dual brush block copolymers in solution and on surfaces.* Polymer Chemistry, 2011. **2**(1): p. 137-147.
31. Zehm, D., et al., *Straightforward Access to Amphiphilic Dual Bottle Brushes by Combining RAFT, ATRP, and NMP Polymerization in One Sequence.* Macromolecules, 2011. **44**(24): p. 9635-9641.
32. Sunder, A., et al., *Controlled synthesis of hyperbranched polyglycerols by ring-opening multibranching polymerization.* Macromolecules, 1999. **32**(13): p. 4240-4246.
33. Odijk, T., *ON THE STATISTICS AND DYNAMICS OF CONFINED OR ENTANGLED STIFF POLYMERS.* Macromolecules, 1983. **16**(8): p. 1340-1344.
34. Watson, J.D. and F.H.C. Crick, *MOLECULAR STRUCTURE OF NUCLEIC ACIDS - A STRUCTURE FOR DEOXYRIBOSE NUCLEIC ACID.* Nature, 1953. **171**(4356): p. 737-738.
35. DeHaseth, P.L. and J.D. Helmann, *Open complex formation by Escherichia coli RNA polymerase: the mechanism of polymerase-induced strand separation of double helical DNA.* Molecular Microbiology, 1995. **16**(5): p. 817-824.
36. Fuller, R.S., B.E. Funnell, and A. Kornberg, *The Dnaa Protein Complex with the Escherichia-Coli Chromosomal Replication Origin (Oric) and Other Dna Sites.* Cell, 1984. **38**(3): p. 889-900.
37. Erzberger, J.P., M.L. Mott, and J.M. Berger, *Structural basis for ATP-dependent DnaA assembly and replication-origin remodeling.* Nature Structural & Molecular Biology, 2006. **13**(8): p. 676-683.
38. Mott, M.L. and J.M. Berger, *DNA replication initiation: mechanisms and regulation in bacteria.* Nature Reviews Microbiology, 2007. **5**(5): p. 343-354.
39. Travers, A. and G. Muskhelishvili, *DNA supercoiling - A global transcriptional regulator for enterobacterial growth?* Nature Reviews Microbiology, 2005. **3**(2): p. 157-169.
40. Radloff, R., W. Bauer, and J. Vinograd, *A DYE-BUOYANT-DENSITY METHOD FOR DETECTION AND ISOLATION OF CLOSED CIRCULAR DUPLEX DNA - CLOSED CIRCULAR DNA IN HELA CELLS.* Proceedings of the National Academy of Sciences of the United States of America, 1967. **57**(5): p. 1514-&.
41. Depew, R.E. and J.C. Wang, *CONFORMATIONAL FLUCTUATIONS OF DNA HELIX.* Proceedings of the National Academy of Sciences of the United States of America, 1975. **72**(11): p. 4275-4279.
42. Horowitz, D.S. and J.C. Wang, *TORSIONAL RIGIDITY OF DNA AND LENGTH DEPENDENCE OF THE FREE-ENERGY OF DNA SUPERCOILING.* Journal of Molecular Biology, 1984. **173**(1): p. 75-91.
43. Vologodskii, A.V. and N.R. Cozzarelli, *Conformational and Thermodynamic Properties of Supercoiled Dna.* Annual Review of Biophysics and Biomolecular Structure, 1994. **23**: p. 609-643.
44. Rief, M., H. Clausen-Schaumann, and H.E. Gaub, *Sequence-dependent mechanics of single DNA molecules.* Nature Structural Biology, 1999. **6**(4): p. 346-349.
45. Wang, M.D., et al., *Stretching DNA with optical tweezers.* Biophysical Journal, 1997. **72**(3): p. 1335-1346.
46. Marko, J.F., *DNA under high tension: Overstretching, undertwisting, and relaxation dynamics.* Physical Review E, 1998. **57**(2): p. 2134-2149.
47. Bustamante, C., et al., *ENTROPIC ELASTICITY OF LAMBDA-PHAGE DNA.* Science, 1994. **265**(5178): p. 1599-1600.
48. Lebrun, A. and R. Lavery, *Modelling extreme stretching of DNA.* Nucleic Acids Research, 1996. **24**(12): p. 2260-2267.
49. Severin, N., et al., *Blowing DNA bubbles.* Nano Letters, 2006. **6**(11): p. 2561-2566.
50. Lee, G.U., L.A. Chrisey, and R.J. Colton, *DIRECT MEASUREMENT OF THE FORCES BETWEEN COMPLEMENTARY STRANDS OF DNA.* Science, 1994. **266**(5186): p. 771-773.

51. Schmidt, S.W., M.K. Beyer, and H. Clausen-Schaumann, *Dynamic strength of the silicon-carbon bond observed over three decades of force-loading rates.* Journal of the American Chemical Society, 2008. **130**(11): p. 3664-3668.
52. Smith, D.E., et al., *The bacteriophage phi 29 portal motor can package DNA against a large internal force.* Nature, 2001. **413**(6857): p. 748-752.
53. Strick, T.R., et al., *The elasticity of a single supercoiled DNA molecule.* Science, 1996. **271**(5257): p. 1835-1837.
54. Strick, T.R., D. Bensimon, and V. Croquette, *Micro-mechanical measurement of the torsional modulus of DNA.* Genetica, 1999. **106**(1-2): p. 57-62.
55. Strick, T.R., et al., *Behavior of supercoiled DNA.* Biophysical Journal, 1998. **74**(4): p. 2016-2028.
56. Marko, J.F., *Stretching must twist DNA.* Europhysics Letters, 1997. **38**(3): p. 183-188.
57. Kamien, R.D., et al., *Direct determination of DNA twist-stretch coupling.* Europhysics Letters, 1997. **38**(3): p. 237-242.
58. Djalali, R., S.Y. Li, and M. Schmidt, *Amphipolar core-shell cylindrical brushes as templates for the formation of gold clusters and nanowires.* Macromolecules, 2002. **35**(11): p. 4282-4288.
59. Zhang, M.F., M. Drechsler, and A.H.E. Muller, *Template-controlled synthesis of wire-like cadmium sulfide nanoparticle assemblies within core-shell cylindrical polymer brushes.* Chemistry of Materials, 2004. **16**(3): p. 537-543.
60. Neugebauer, D., et al., *Densely-grafted and double-grafted PEO brushes via ATRP. A route to soft elastomers.* Macromolecules, 2003. **36**(18): p. 6746-6755.
61. Lee, H.I., et al., *pH-induced conformational changes of loosely grafted molecular brushes containing poly(acrylic acid) side chains.* Polymer, 2008. **49**(25): p. 5490-5496.
62. Sheiko, S.S., B.S. Sumerlin, and K. Matyjaszewski, *Cylindrical molecular brushes: Synthesis, characterization, and properties.* Progress in Polymer Science, 2008. **33**(7): p. 759-785.
63. Beers, K.L., et al., *The synthesis of densely grafted copolymers by atom transfer radical polymerization.* Macromolecules, 1998. **31**(26): p. 9413-9415.
64. Gao, H.F. and K. Matyjaszewski, *Synthesis of molecular brushes by "grafting onto" method: Combination of ATRP and click reactions.* Journal of the American Chemical Society, 2007. **129**(20): p. 6633-6639.
65. Deffieux, A. and M. Schappacher, *Synthesis and characterization of star and comb polystyrenes using isometric poly(chloroethyl vinyl ether) oligomers as reactive backbone.* Macromolecules, 1999. **32**(6): p. 1797-1802.
66. Tsukahara, Y., et al., *STUDY ON THE RADICAL POLYMERIZATION BEHAVIOR OF MACROMONOMERS.* Macromolecules, 1989. **22**(4): p. 1546-1552.
67. Wintermantel, M., et al., *Molecular bottlebrushes.* Macromolecules, 1996. **29**(3): p. 978-983.
68. Pantazis, D., I. Chalari, and N. Hadjichristidis, *Anionic polymerization of styrenic macromonomers.* Macromolecules, 2003. **36**(11): p. 3783-3785.
69. Heroguez, V., et al., *Synthesis of alpha-norbornenylpoly(ethylene oxide) macromonomers and their ring-opening metathesis polymerization.* Macromolecules, 1996. **29**(13): p. 4459-4464.
70. Cheng, C., E. Khoshdel, and K.L. Wooley, *ATRP from a norbornenyl-functionalized initiator: Balancing of complementary reactivity for the preparation of alpha-norbornenyl macromonomers/omega-haloalkyl macroinitiators.* Macromolecules, 2005. **38**(23): p. 9455-9465.
71. Liu, Y.F., V. Abetz, and A.H.E. Muller, *Janus cylinders.* Macromolecules, 2003. **36**(21): p. 7894-7898.
72. Neugebauer, D., et al., *Densely heterografted brush macromolecules with crystallizable grafts. Synthesis and bulk properties.* Macromolecules, 2006. **39**(2): p. 584-593.
73. Fredrickson, G.H., *SURFACTANT-INDUCED LYOTROPIC BEHAVIOR OF FLEXIBLE POLYMER-SOLUTIONS.* Macromolecules, 1993. **26**(11): p. 2825-2831.
74. Gunari, N., et al., *Surfactant-induced helix formation of cylindrical brush polymers with poly(L-lysine) side chains.* Macromolecular Rapid Communications, 2008. **29**(10): p. 821-825.

75. Li, C.M., et al., *New perspectives for the design of molecular actuators: Thermally induced collapse of single macromolecules from cylindrical brushes to spheres.* Angewandte Chemie-International Edition, 2004. **43**(9): p. 1101-1104.
76. Potemkin, II, *Persistence length of comblike polymers strongly adsorbed on a flat surface.* Macromolecules, 2006. **39**(21): p. 7178-7180.
77. Sheiko, S.S., et al., *Adsorption-induced scission of carbon-carbon bonds.* Nature, 2006. **440**(7081): p. 191-194.
78. Borner, H.G., et al., *Synthesis of molecular brushes with block copolymer side chains using atom transfer radical polymerization.* Macromolecules, 2001. **34**(13): p. 4375-4383.
79. Ishizu, K. and H. Yamada, *Architecture of prototype copolymer brushes by grafting-from ATRP approach from functionalized alternating comb-shaped copolymers.* Macromolecules, 2007. **40**(9): p. 3056-3061.
80. Amidon, G.L., et al., *A THEORETICAL BASIS FOR A BIOPHARMACEUTIC DRUG CLASSIFICATION - THE CORRELATION OF IN-VITRO DRUG PRODUCT DISSOLUTION AND IN-VIVO BIOAVAILABILITY.* Pharmaceutical Research, 1995. **12**(3): p. 413-420.
81. Li, P., L.W. Zhao, and S.H. Yalkowsky, *Combined effect of cosolvent and cyclodextrin on solubilization of nonpolar drugs.* Journal of Pharmaceutical Sciences, 1999. **88**(11): p. 1107-1111.
82. Kawakami, K., K. Miyoshi, and Y. Ida, *Solubilization behavior of poorly soluble drugs with combined use of gelucire 44/14 and cosolvent.* Journal of Pharmaceutical Sciences, 2004. **93**(6): p. 1471-1479.
83. Sanghvi, R., D. Evans, and S.H. Yalkowsky, *Stacking complexation by nicotinamide: A useful way of enhancing drug solubility.* International Journal of Pharmaceutics, 2007. **336**(1): p. 35-41.
84. Hancock, B.C. and M. Parks, *What is the true solubility advantage for amorphous pharmaceuticals?* Pharmaceutical Research, 2000. **17**(4): p. 397-404.
85. Matsumura, Y. and H. Maeda, *A NEW CONCEPT FOR MACROMOLECULAR THERAPEUTICS IN CANCER-CHEMOTHERAPY - MECHANISM OF TUMORITROPIC ACCUMULATION OF PROTEINS AND THE ANTITUMOR AGENT SMANCS.* Cancer Research, 1986. **46**(12): p. 6387-6392.
86. Maeda, H., et al., *Tumor vascular permeability and the EPR effect in macromolecular therapeutics: a review.* Journal of Controlled Release, 2000. **65**(1-2): p. 271-284.
87. Kataoka, K., A. Harada, and Y. Nagasaki, *Block copolymer micelles for drug delivery: design, characterization and biological significance.* Advanced Drug Delivery Reviews, 2001. **47**(1): p. 113-131.
88. Jones, M.C., M. Ranger, and J.C. Leroux, *pH-sensitive unimolecular polymeric micelles: Synthesis of a novel drug carrier.* Bioconjugate Chemistry, 2003. **14**(4): p. 774-781.
89. Kabanov, A.V., et al., *A NEW CLASS OF DRUG CARRIERS - MICELLES OF POLY(OXYETHYLENE)-POLY(OXYPROPYLENE) BLOCK COPOLYMERS AS MICROCONTAINERS FOR DRUG TARGETING FROM BLOOD IN BRAIN.* Journal of Controlled Release, 1992. **22**(2): p. 141-157.
90. Mortensen, K., *PEO-related block copolymer surfactants.* Colloids and Surfaces a-Physicochemical and Engineering Aspects, 2001. **183**: p. 277-292.
91. Newkome, G.R., et al., *CHEMISTRY OF MICELLES .13. UNIMOLECULAR MICELLES.* Angewandte Chemie-International Edition in English, 1991. **30**(9): p. 1178-1180.
92. Svenson, S. and D.A. Tomalia, *Commentary - Dendrimers in biomedical applications - reflections on the field.* Advanced Drug Delivery Reviews, 2005. **57**(15): p. 2106-2129.
93. Wolinsky, J.B. and M.W. Grinstaff, *Therapeutic and diagnostic applications of dendrimers for cancer treatment.* Advanced Drug Delivery Reviews, 2008. **60**(9): p. 1037-1055.
94. Haag, R. and F. Kratz, *Polymer therapeutics: Concepts and applications.* Angewandte Chemie-International Edition, 2006. **45**(8): p. 1198-1215.
95. Kobayashi, H. and M.W. Brechbiel, *Nano-sized MRI contrast agents with dendrimer cores.* Advanced Drug Delivery Reviews, 2005. **57**(15): p. 2271-2286.
96. Watanabe, K., et al., *In vivo siRNA delivery with dendritic poly(L-lysine) for the treatment of hypercholesterolemia.* Molecular Biosystems, 2009. **5**(11): p. 1306-1310.

97. Tomalia, D.A., et al., *A NEW CLASS OF POLYMERS - STARBURST-DENDRITIC MACROMOLECULES.* Polymer Journal, 1985. **17**(1): p. 117-132.
98. Hawker, C.J. and J.M.J. Frechet, *PREPARATION OF POLYMERS WITH CONTROLLED MOLECULAR ARCHITECTURE - A NEW CONVERGENT APPROACH TO DENDRITIC MACROMOLECULES.* Journal of the American Chemical Society, 1990. **112**(21): p. 7638-7647.
99. Frechet, J.M.J., et al., *Dendrimers and hyperbranched polymers: Two families of three-dimensional macromolecules with similar but clearly distinct properties.* Journal of Macromolecular Science-Pure and Applied Chemistry, 1996. **A33**(10): p. 1399-1425.
100. Yellepeddi, V.K., A. Kumar, and S. Palakurthi, *Biotinylated Poly(amido)amine (PAMAM) Dendrimers as Carriers for Drug Delivery to Ovarian Cancer Cells In Vitro.* Anticancer Research, 2009. **29**(8): p. 2933-2943.
101. Debrabandervandenberg, E.M.M. and E.W. Meijer, *POLY(PROPYLENE IMINE) DENDRIMERS - LARGE-SCALE SYNTHESIS BY HETEREOGENEOUSLY CATALYZED HYDROGENATIONS.* Angewandte Chemie-International Edition in English, 1993. **32**(9): p. 1308-1311.
102. Spetzler, J.C. and J.P. Tam, *UNPROTECTED PEPTIDES AS BUILDING-BLOCKS FOR BRANCHED PEPTIDES AND PEPTIDE DENDRIMERS.* International Journal of Peptide and Protein Research, 1995. **45**(1): p. 78-85.
103. Wooley, K.L., J.M.J. Frechet, and C.J. Hawker, *INFLUENCE OF SHAPE ON THE REACTIVITY AND PROPERTIES OF DENDRITIC, HYPERBRANCHED AND LINEAR AROMATIC POLYESTERS.* Polymer, 1994. **35**(21): p. 4489-4495.
104. Wu, P., et al., *Efficiency and fidelity in a click-chemistry route to triazole dendrimers by the copper(I)-catalyzed ligation of azides and alkynes.* Angewandte Chemie-International Edition, 2004. **43**(30): p. 3928-3932.
105. McGrath, D.V., *Dendrimer disassembly as a new paradigm for the application of dendritic structures.* Molecular Pharmaceutics, 2005. **2**(4): p. 253-263.
106. Kim, Y.H. and O.W. Webster, *WATER-SOLUBLE HYPERBRANCHED POLYPHENYLENE - A UNIMOLECULAR MICELLE.* Journal of the American Chemical Society, 1990. **112**(11): p. 4592-4593.
107. Haag, R., *Supramolecular drug-delivery systems based on polymeric core-shell architectures.* Angewandte Chemie-International Edition, 2004. **43**(3): p. 278-282.
108. Sunder, A., et al., *Hyperbranched polyether polyols: A modular approach to complex polymer architectures.* Advanced Materials, 2000. **12**(3): p. 235-+.
109. Stiriba, S.E., H. Frey, and R. Haag, *Dendritic polymers in biomedical applications: From potential to clinical use in diagnostics and therapy.* Angewandte Chemie-International Edition, 2002. **41**(8): p. 1329-1334.
110. Kurniasih, I.N., et al., *Supramolecular Aggregates of Water Soluble Dendritic Polyglycerol Architectures for the Solubilization of Hydrophobic Compounds.* Macromolecular Rapid Communications, 2010. **31**(17): p. 1516-1520.
111. Turk, H., et al., *Water-soluble dendritic core-shell-type architectures based on polyglycerol for solubilization of hydrophobic drugs.* Chemistry-a European Journal, 2007. **13**(15): p. 4187-4196.
112. Cheng, Y.Y. and T.W. Xu, *Dendrimers as potential drug carriers. Part I. Solubilization of non-steroidal anti-inflammatory drugs in the presence of polyamidoamine dendrimers.* European Journal of Medicinal Chemistry, 2005. **40**(11): p. 1188-1192.
113. Cheng, Y.Y. and T.W. Xu, *The effect of dendrimers on the pharmacodynamic and pharmacokinetic behaviors of non-covalently or covalently attached drugs.* European Journal of Medicinal Chemistry, 2008. **43**(11): p. 2291-2297.
114. Hu, J.J., et al., *Host-Guest Chemistry and Physicochemical Properties of the Dendrimer-Mycophenolic Acid Complex.* Journal of Physical Chemistry B, 2009. **113**(1): p. 64-74.
115. Rabe, J.P. and S. Buchholz, *Commensurability and Mobility in 2-Dimensional Molecular-Patterns on Graphite.* Science, 1991. **253**(5018): p. 424-427.
116. Severin, N., J.P. Rabe, and D.G. Kurth, *Fully extended polyelectrolyte-amphiphile complexes adsorbed on graphite.* Journal of the American Chemical Society, 2004. **126**(12): p. 3696-3697.

117. Adamcik, J., et al., *Temperature-Controlled Assembly of High Ordered/Disordered Dodecylamine Layers on HOPG: Consequences for DNA Patterning.* Langmuir, 2009. **25**(5): p. 3159-3162.
118. Emslie, A.G., F.T. Bonner, and L.G. Peck, *Flow of A Viscous Liquid on A Rotating Disk.* Journal of Applied Physics, 1958. **29**(5): p. 858-862.
119. Severin, N., et al., *Self-sorting of polyelectrolyte-amphiphile complexes on a graphite surface.* Macromolecules, 2007. **40**(14): p. 5182-5186.
120. Cyr, D.M., et al., *Functional group identification in scanning tunneling microscopy of molecular adsorbates.* Journal of Physical Chemistry, 1996. **100**(32): p. 13747-13759.
121. Coman, D. and I.M. Russu, *Base pair opening in three DNA-unwinding elements.* Journal of Biological Chemistry, 2005. **280**(21): p. 20216-20221.
122. Lionnet, T., et al., *Wringing out DNA.* Physical Review Letters, 2006. **96**(17).
123. Randall, G.L., L. Zechiedrich, and B.M. Pettitt, *In the absence of writhe, DNA relieves torsional stress with localized, sequence-dependent structural failure to preserve B-form.* Nucleic Acids Research, 2009. **37**(16): p. 5568-5577.
124. EssevazRoulet, B., U. Bockelmann, and F. Heslot, *Mechanical separation of the complementary strands of DNA.* Proceedings of the National Academy of Sciences of the United States of America, 1997. **94**(22): p. 11935-11940.
125. Yakovchuk, P., E. Protozanova, and M.D. Frank-Kamenetskii, *Base-stacking and base-pairing contributions into thermal stability of the DNA double helix.* Nucleic Acids Research, 2006. **34**(2): p. 564-574.
126. Evans, E.A. and D.A. Calderwood, *Forces and bond dynamics in cell adhesion.* Science, 2007. **316**(5828): p. 1148-1153.
127. Diezemann, G. and A. Janshoff, *Force-clamp spectroscopy of reversible bond breakage.* Journal of Chemical Physics, 2009. **130**(4).
128. Garcia-Manyes, S., et al., *Direct observation of an ensemble of stable collapsed states in the mechanical folding of ubiquitin.* Proceedings of the National Academy of Sciences of the United States of America, 2009. **106**(26): p. 10534-10539.
129. Ciechanover, A., *Proteolysis: from the lysosome to ubiquitin and the proteasome.* Nature Reviews Molecular Cell Biology, 2005. **6**(1): p. 79-86.
130. Liang, H., et al., *Statistics of Time-Dependent Rupture of Single ds-DNA.* Journal of Physical Chemistry B, 2013. **117**(29): p. 8875-8879.
131. Bell, G.I., *Models for Specific Adhesion of Cells to Cells.* Science, 1978. **200**(4342): p. 618-627.
132. Hummer, G. and A. Szabo, *Kinetics from nonequilibrium single-molecule pulling experiments.* Biophysical Journal, 2003. **85**(1): p. 5-15.
133. Dudko, O.K., G. Hummer, and A. Szabo, *Intrinsic rates and activation free energies from single-molecule pulling experiments.* Physical Review Letters, 2006. **96**(10).
134. Baumann, C.G., et al., *Ionic effects on the elasticity of single DNA molecules.* Proceedings of the National Academy of Sciences of the United States of America, 1997. **94**(12): p. 6185-6190.
135. Williams, M.C., et al., *Effect of on on the overstretching transition of double-stranded DNA: Evidence of force-induced DNA melting.* Biophysical Journal, 2001. **80**(2): p. 874-881.
136. Rivetti, C., M. Guthold, and C. Bustamante, *Scanning Force Microscopy of DNA Deposited onto Mica: EquilibrationversusKinetic Trapping Studied by Statistical Polymer Chain Analysis.* Journal of Molecular Biology, 1996. **264**(5): p. 919-932.
137. Schwaderer, P., et al., *Single-molecule measurement of the strength of a siloxane bond.* Langmuir, 2008. **24**(4): p. 1343-1349.
138. Bensimon, A., et al., *Alignment and Sensitive Detection of Dna by A Moving Interface.* Science, 1994. **265**(5181): p. 2096-2098.
139. Beyer, M.K. and H. Clausen-Schaumann, *Mechanochemistry: The mechanical activation of covalent bonds.* Chemical Reviews, 2005. **105**(8): p. 2921-2948.
140. Konopka, M., et al., *Mechanochemistry and thermochemistry are different: Stress-induced strengthening of chemical bonds.* Physical Review Letters, 2008. **100**(11).

141. Wiita, A.P., et al., *Probing the chemistry of thioredoxin catalysis with force.* Nature, 2007. **450**: p. 124-+.
142. Takeda, N., et al., *Kinetic and theoretical studies on the mechanism of alkaline hydrolysis of DNA.* Journal of Organic Chemistry, 2000. **65**(14): p. 4391-4396.
143. Boudaiffa, B., et al., *Resonant formation of DNA strand breaks by low-energy (3 to 20 eV) electrons.* Science, 2000. **287**(5458): p. 1658-1660.
144. Zheng, Y., et al., *Chemical basis of DNA sugar-phosphate cleavage by low-energy electrons.* Journal of the American Chemical Society, 2005. **127**(47): p. 16592-16598.
145. Schroeder, G.K., et al., *The time required for water attack at the phosphorus atom of simple phosphodiesters and of DNA.* Proceedings of the National Academy of Sciences of the United States of America, 2006. **103**(11): p. 4052-4055.
146. Vesenka, J., R. Miller, and E. Henderson, *3-DIMENSIONAL PROBE RECONSTRUCTION FOR ATOMIC-FORCE MICROSCOPY.* Review of Scientific Instruments, 1994. **65**(7): p. 2249-2251.
147. Lord, S.J., et al., *Tadpole conformation of gradient polymer brushes.* Macromolecules, 2004. **37**(11): p. 4235-4240.
148. Zhang, A.F., et al., *A covalent-chemistry approach to giant macromolecules and their wetting behavior on solid substrates.* Angewandte Chemie-International Edition, 2004. **43**(39): p. 5185-5188.
149. Kumaki, J. and T. Hashimoto, *Conformational change in an isolated single synthetic polymer chain on a mica surface observed by atomic force microscopy.* Journal of the American Chemical Society, 2003. **125**(16): p. 4907-4917.
150. Gerle, M., et al., *Main Chain Conformation and Anomalous Elution Behavior of Cylindrical Brushes As Revealed by GPC/MALLS, Light Scattering, and SFMΓÇí.* Macromolecules, 1999. **32**(8): p. 2629-2637.
151. Zhuang, W., et al., *Self-folding of charged single dendronized polymers.* Advanced Materials, 2008. **20**(17): p. 3204-+.
152. Fan, F.Q. and K.J. Stebe, *Assembly of colloidal particles by evaporation on surfaces with patterned hydrophobicity.* Langmuir, 2004. **20**(8): p. 3062-3067.
153. Kurniasih, I.N., et al., *Synthesis and transport properties of new dendritic core-shell architectures based on hyperbranched polyglycerol with biphenyl-PEG shells.* New Journal of Chemistry, 2012. **36**(2): p. 371-379.
154. Kurniasih, I.N., et al., *A bifunctional nanocarrier based on amphiphilic hyperbranched polyglycerol derivatives.* Journal of Materials Chemistry B, 2013. **1**(29): p. 3569-3577.
155. Kalyanasundaram, K. and J.K. Thomas, *ENVIRONMENTAL EFFECTS ON VIBRONIC BAND INTENSITIES IN PYRENE MONOMER FLUORESCENCE AND THEIR APPLICATION IN STUDIES OF MICELLAR SYSTEMS.* Journal of the American Chemical Society, 1977. **99**(7): p. 2039-2044.
156. Popeney, C.S., et al., *Tandem Coordination, Ring-Opening, Hyperbranched Polymerization for the Synthesis of Water-Soluble Core-Shell Unimolecular Transporters.* Acs Macro Letters, 2012. **1**(5): p. 564-567.
157. Greenspan, P. and S.D. Fowler, *SPECTROFLUOROMETRIC STUDIES OF THE LIPID PROBE, NILE RED.* Journal of Lipid Research, 1985. **26**(7): p. 781-789.

7. Bibliography

7.1 Abbreviations

AFM: Atomic Force Microscopy

ATRP: Atom Transfer Radical Polymerization

bp: base pairs

CMC: Critical Micelle Concentration

DNA: deoxyribonucleic acid

EFM: Electrostatics Force Microscopy

FJC: freely joint chain

HOPG: Highly Oriented Pyrolytic Graphite

hPG: hyperbranched polyglycerol

NMP: Nitroxide-mediated Polymerization

RAFT: Reversible Addition Fragmentation Chain Transfer

rps: rounds per second

PAMAM: poly-amido-amines

poly(BuA): poly(n-butyl acrylate)

poly(CIPEA): poly(2-chloropropionyloxyethyl acrylate (CIPEA))

poly(NIPAM): poly(N-isopropylacryamide)

poly(PEGA): poly(ethylene glycol monomethyl ether acrylate)

poly(ΦTEA): poly(2-phenyl-2-(2,2,6,6-tetramethyl-piperidine-1-oxyl)ethyl acrylate)

PPI: poly-propylene-imines

PS: polystyrene

SEC: Size Exclusion Chromatography

SFM: Scanning Force Microscopy

SNOM: Scanning Near Field Optical Microscopy

SPM: Scanning Probe Microscopy

STM: Scanning Tunneling Microscopy

WLC: worm like chain

7.2 Publications

1. Nile Red Dye in Aqueous Surfactant and Micellar Solution,

   Indah Nurita Kurniasih, Hua Liang, Parveen Mohr, Gaurang Khot, Jürgen P. Rabe, Andreas Mohr; submitted

2. Statistics of time-dependent rupture of single ds-DNA

   Hua Liang, Nikolai Severin, Simon Fugmann, Igor Sokolov, Jürgen P. Rabe

   Journal of Physical Chemistry B **117** (2013), 8875-8879

3. A bifunctional nanocarrier based on amphiphilic hyperbranched polyglycerol derivatives

   Kurniasih, IN; Liang, H; Kumar, S; Mohr A; Sharma, SK; Rabe, JP; and Haag, R;

   Journal of Materials Chemistry B **1** (2013), 3569-3577

4. Synthesis and transport properties of new dendritic core–shell architectures based on hyperbranched polyglycerol with biphenyl-PEG shells

   Kurniasih, IN; Liang, H; Möschwitzer, VD; Quadir, MA; Radowski, M; Rabe, JP; and Haag, R

   New Journal of Chemistry **36** (2012), 371-379

5. Straightforward access to amphiphilic dual bottle-brushes by combining RAFT, ATRP and NMP polymerization in one sequence

   Zehm, D; Laschewsky, A; Liang, H; and Rabe, JP

   Macromolecules (2011), 9635-9641

6. Synthesis and self-assembly of amphiphilic semi-brush and dual brush block copolymers in solution and on surfaces

   Zehm, D; Laschewsky, A; Heunemann, P; Gradzielski, M; Prévost, S; Liang, H; Rabe, JP; and Lutz, J

   Polymer Chemistry **2** (2011), 137-147

7. Amphiphilic dual brush block copolymers as "giant surfactants" and their aqueous self-

assembly

Zehm, D; Laschewsky, A; Gradzielski, M; Prévost, S; Liang, H; Rabe, JP; Schweins, R; and Gummel, J

Langmuir **26** (2010), 3145-3155

8. Supramolecular aggregates of water soluble dendritic polyglycerol architectures for the solubilization of hydrophobic compounds

Kurniasih, IN; Liang, H; Rabe, JP; and Haag, R;

Macromolecular Rapid Communications **31** (2010), 1516-1520

Acknowledgement

It was a very good time during my stay in the PMM group. I would like to give my sincere thanks to the following people:

Prof. Dr. Jürgen P. Rabe, for his guiding through my scientific studies and his financial support; Dr. Nikolai Severin, for his kindness and patience to answering all kinds of questions during last a few years; all other members of PMM group, for their fruitful discussions or technical support.

I would like to thank the collaboration partners: Prof. Rainer Haag, Dr. Indah Nurita Kurniasih, for their synthesis of hPG; Prof. Andre Laschewsky, Dr. Daniel Zehm, for their synthesis of cylindrical brush polymers.

I would like to thank SFB 448 and SFB 765 for the funding.

I would like to thank Indah, for her love, patience and continuous support.

Erklärung

Hiermit erkläre ich, die vorliegende Arbeit selbständig und ohne unerlaubte Hilfe angefertigt zu haben und nur die angegebene Literaturen und Hilfsmittel verwendet zu haben. Ich habe mich anderwärts nicht um einen Doktorgrad beworben und besitze einen entsprechenden Doktorgrad nicht. Ich erkläre die Kenntnisnahme der dem Verfahren zugrunde liegenden Promotionsordnung der Mathematisch-Naturwissenschaftlichen Fakultät der Humboldt-Universität zu Berlin.

Liang Hua

Berlin, 27. Nov. 2014